



Study of photoluminescence properties of nanoscale systems under high electric field

Linda Venturi

► To cite this version:

Linda Venturi. Study of photoluminescence properties of nanoscale systems under high electric field. Materials Science [cond-mat.mtrl-sci]. Normandie Université, 2019. English. NNT : 2019NORMR118 . tel-02506142

HAL Id: tel-02506142

<https://theses.hal.science/tel-02506142>

Submitted on 12 Mar 2020

HAL is a multi-disciplinary open access archive for the deposit and dissemination of scientific research documents, whether they are published or not. The documents may come from teaching and research institutions in France or abroad, or from public or private research centers.

L'archive ouverte pluridisciplinaire **HAL**, est destinée au dépôt et à la diffusion de documents scientifiques de niveau recherche, publiés ou non, émanant des établissements d'enseignement et de recherche français ou étrangers, des laboratoires publics ou privés.



Normandie Université

THÈSE

Pour obtenir le diplôme de doctorat

Spécialité Physique

Préparée au sein de

« Groupe de Physique de Matériaux, UMR 6634, CNRS, Normandie Université »

Study of photoluminescence properties of nanoscale systems under high electric field

**Présentée et soutenue par
Linda VENTURI**

**Thèse soutenue publiquement le 18 décembre 2019
devant le jury composé de**

M. François JULIEN	Directeur de recherche, CNRS, Univ. Paris-Sud	Rapporteur
M. Julien CLAUDON	Chercheur CEA, Grenoble	Rapporteur
M. Paolo MAIOLI	Chercheur CNRS, Lyon	Examineur
M. Fabrice GOURBILLEAU	Directeur de recherche, Cimap-Ensicaen, Caen	Examineur
M. Lorenzo RIGUTTI	Maître de conférences, GPM, Normandie Université	Codirecteur de thèse
M.me Angela VELLA	Professeur, GPM, Normandie Université	Directeur de thèse

Thèse dirigée par Angela VELLA et Lorenzo RIGUTTI, GPM, Normandie Université



Abstract

In this thesis, the Laser-assisted Atom Probe Tomography is coupled *in-situ* with a photoluminescence (PL) bench, where the pulsed laser radiation is used to trigger the ion evaporation from the specimens and, simultaneously, to activate the emission from optically active centers present into the material.

For this work, two different materials were selected: diamond nano-needles with embedded optically active defects (color centers) and a ZnO/(Mg,Zn)O multi-quantum-well (MQW) heterostructure, which contains quantum emitters of different thicknesses.

Thanks to this original photoluminescence setup, the influence of the electric field on the fine structure of some color centers, embedded into the diamond nanoneedles, was observed. The first study focused on the neutral nitrogen-vacancy center (NV^0), which is one among the most studied color centers in literature. The evolution of the NV^0 optical signature, as a function of the applied bias, allowed to evaluate the mechanical stress ($> 1 \text{ GPa}$) and the electric-field acting on diamond tips. These results demonstrate an original new method to perform contactless piezo-spectroscopy of nanoscale systems under uniaxial tensile stress, generated by the electric field. This method was applied also on another color center, which nature is still not clear in literature, emitting at 2.65 eV , and more sensitive than the NV^0 color centers to the stress/strain field. New results on its opto-mechanical properties were obtained, but its identity still needs to be understood. Since the evaporation field of diamond is really high, the diamond nanoneedles were not analyzed using La-APT. Therefore the coupled in-situ technique was applied in order to study the ZnO/(Mg,Zn)O MQW heterostructure, accessing to the structure, composition and optical signature of the probed specimen in only one experiment. The photoluminescence spectra acquired by the specimen during its on-

going evaporation represents a unique source of information for the understanding of the mechanism of light-matter interaction and the physics of photoemission under high electric field. The correlation of the structural and optical information, related to this MQW heterostructure, demonstrates that the coupled in-situ technique can overlap the diffraction limit of the PL laser and that, as done for the diamond nanoneedles, is possible to estimate the induced-tensile-stress.

The results achieved by the in-situ coupling of the La-APT technique with the PL spectroscopy show that such instrument is an innovative and powerful technique to perform research at the nanometric scale.

For this reason, this work can open new perspectives for a deeply understanding of the physics related to the studied systems in parallel with the continuous enhancement of the experimental setup.

Contents

Introduction	1
1 Experimental Methods	5
1.1 Microphotoluminescence	5
1.1.1 Principles of photoluminescence	5
1.1.2 Experimental study of photoluminescence signals	9
1.1.3 μPL experimental setup	11
1.2 Laser-assisted Atom Probe Tomography	12
1.2.1 Atom Probe Tomography	13
1.2.2 Physics of field evaporation	15
1.2.3 Laser-induced field evaporation	18
1.2.4 Time-of-flight mass spectroscopy	19
1.2.5 Three-dimensional reconstruction of APT data	20
1.2.5.1 Delay line detector (DLD)	25
1.2.6 Field of view and detection efficiency	27
1.2.7 Compositional measurements and related issues in APT	30
1.2.7.1 Mass spectra indexation	30
1.2.7.2 Preferential evaporation	31
1.2.7.3 Production of neutral molecules	31
1.2.7.4 Multiple detection events	31
1.2.7.5 Dissociation phenomena	32
1.2.8 Charge State Ratio metrics	34

1.3	La-APT/ μPL coupled “ <i>in-situ</i> ”	34
1.3.1	Experimental setup	35
1.4	FIB/SEM specimens preparation	37
2	Overview about diamond	45
2.1	Physical properties of diamond	45
2.2	Crystal Structure	47
2.2.1	Direct Lattice	47
2.3	Band Structure	48
2.4	Natural and Synthetic Diamond	49
2.4.1	Mechanical properties	50
2.4.2	Defects in Diamond	52
2.4.3	Thermal and electrical properties	54
2.5	Description of the synthetic diamond needles	55
2.5.1	Synthesis procedure	55
2.5.2	Diamond defects: focus on nitrogen vacancy centers	58
3	Photoluminescence-piezo-spectroscopy on diamond nanoneedles	67
3.1	Mechanism of induced stress on a diamond tip	68
3.2	The NV^0 defect as a stress-field sensor	70
3.2.1	Experimental results obtained on the NV^0 stress-sensor: dependency on the bias	73
3.2.2	Experimental results obtained on the NV^0 stress-sensor: dependency on the position	79
3.2.3	Experimental results obtained on the NV^0 stress-sensor: investigation of the radiative lifetime	83
3.3	The color-center at $2.65eV$	87
3.3.1	Piezo-spectroscopic study of the center at $2.65eV$: dependence on the V_{DC} bias	90
3.3.2	Piezo-spectroscopic study of the center at $2.65eV$: dependence on the position	93

3.3.3	Polarization spectroscopic study of the center at 2.65 eV under V_{DC} bias	95
3.4	Multi-photon excitation of the NV ⁰ defect into the IR range	96
3.4.1	Experimental results	98
3.4.1.1	Dependency of the NV ⁰ amplitude on the illumination position	100
3.4.1.2	Piezo-spectroscopic study of the NV ⁰ center as a function of the V_{DC} applied bias	101
3.4.1.3	Dependency of the NV ⁰ signal as a function of the applied power	103
4	Structural and optical properties of ZnO/MgZnO heterostructures	109
4.1	Introduction	109
4.1.1	ZnO/MgZnO heterostructures	111
4.1.1.1	Band alignment in ZnO/MgZnO heterostructures	117
4.1.2	Carriers distribution inside the ZnO quantum wells	120
4.1.2.1	Excitons	124
4.1.3	Carrier localization and radiative recombination in ZnO/MgZnO heterstructures	126
4.1.4	Stress and Strain tensors of hexagonal systems	129
4.1.5	Strain effect on band structure of ZnO	132
5	Coupled “<i>in-situ</i>” μPL/La-APT measurements of the ZnO/MgZnO MQWs system	135
5.1	The ZnO/MgZnO sample	135
5.1.1	Morphological and structural characteristics of the APT specimens	137
5.2	The <i>in-situ</i> μ PL/La-APT analysis	141
5.2.1	Protocol for the correlative analyses	142
5.2.2	Data acquired by the La-APT system	145
5.2.2.1	Mass spectrum	145
5.2.2.2	3D reconstruction	148

5.2.2.3	<i>Mg</i> -concentration profile	150
5.2.3	μPL analysis	153
5.2.3.1	Spectra before the evaporation of the sample	153
5.2.3.2	Spectra during the evaporation of the sample	154
5.3	Interpretation of the correlated results	157
5.3.1	Evaluation of the stress using the bandgap deformation potential associated to the <i>ZnO</i> substrate	159
Conclusions		163
Bibliography		167
Appendix		A
Acknowledgements		I

List of Figures

1.1	Principles of a PL experiment.	6
1.2	Different electron-hole pairs radiative recombination mechanisms which lead to PL emission	8
1.3	Layout of the PL optical setup	12
1.4	Working principle of APT, in: voltage pulse and laser pulse mode . . .	13
1.5	Schematic rapresentation of the 2D point projection reconstruction method	22
1.6	Detection dynamic in a conventional DLD system	25
1.7	Scheme of the electronic system used to measure the impact position of the ions on the MCP in a conventional MCP/DLD.	26
1.8	Analog-to-digital conversion in a DLD system	27
1.9	Schematic rapresentation of the ions loss mechanisms.	29
1.10	Rapresentation of the dissociation of a molecular ion into two daughter ions	33
1.11	Core of the project: the combination between La-APT and the μ PL systems	35
1.12	Schematic of the experimental setup: the coupled La-APT/ μ PL “ <i>in-situ</i> ”.	36
1.13	Non-radiative and radiative recombination process in annular milled field emission tips	38
1.14	Schematic of diamond specimen preparation by SEM-FIB	40
2.1	sp^3 orbitals	46
2.2	Charge density of sp^3 hybrid orbitals	46
2.3	Unit cell of the diamond structure	47

2.4	Band structure of diamond	48
2.5	Schematic of the formation for the bunch of the needle-like-micro-diamonds	57
2.6	Concentrations of nitrogen and silicon related centers in diamond nanotips	58
2.7	The NV center into the diamond lattice	59
2.8	Schematics of the NV optical transitions.	61
3.1	The PL signal of the diamond Tip 2	69
3.2	Spectra and transition scheme related to the NV^0 center, with and without bias	70
3.3	Field Ion Microscopy image of the apex of a diamond needle	73
3.4	Optical study of the NV^0 ZPL as a function of the applied bias	75
3.5	Rapresentation of the a and b ZPL related to the NV^0 center as a function of the voltage applied	77
3.6	Stress model of nanoscale needles under high electric field	78
3.7	Polar graph related to the NV^0 center	79
3.8	Spatially resolved study of the stress propagation along the needle axis	81
3.9	TRPL analysis related to the NV^0 center	84
3.10	Decay time curves of the NV^0 center	86
3.11	PL signal of the diamond Tip 2	88
3.12	SEM images of the Tip 2 and Tip 3 diamond nanoneedles	91
3.13	μ -PL signal of the Tip 3, acquired at different values of the V_{DC} bias .	92
3.14	Evolution of ‘a’ and ‘b’ lines related the the 2.65 eV and the NV^0 centers	94
3.15	Comparison of NV^0 ZPL and 2.65 eV center polar graphs	95
3.16	Schematic of the multi-photon transition.	97
3.17	SEM image and PL spectra of Tip 4	99
3.18	μ -PL signal acquired with the IR-laser impinging at different positions with respect to the apex of the diamond Tip 4	101
3.19	μ -PL spectra acquired at different values of the V_{DC} bias on Tip 4 . . .	102
3.20	Photo-emission amplitude of the laser SHG and NV^0 signal as a function of the exciting power	104

3.21	Photo-emission amplitude of the NV^0 signal as a function of the exciting power	105
4.1	Rocksalt, zinc blend and wurtzite structures	111
4.2	Representation of the wurtzite unit cell, with the two lattice parameters, a and c , and the u cell-internal parameter indicated	112
4.3	Band structure of ZnO in wurtzite structure	114
4.4	Bandgaps as a function of the lattice constant for various elements of the II-VI groups	116
4.5	Dependence of the a-lattice and c-lattice parameters	117
4.6	Position of band edges (band alignment) in (a) type-I and (b) type-II heterostructure.	119
4.7	Confined electron and hole energies and wave functions within a rectangular quantum well	121
4.8	Effect of an internal electric field acting on confined electron and hole energies and wave functions	123
4.9	Temperature-dependent luminescence spectra of ZnO thin film	125
4.10	Interband transitions at different temperatures, in presence of alloy compositional fluctuations	127
4.11	PL spectra of a $Zn_{0.85}Mg_{0.15}O - ZnO - Zn_{0.85}Mg_{0.15}O$ sample	128
5.1	Schematic of the hierarchic structure of the $ZnO/MgZnO$ MQW heterostructure.	136
5.2	SEM images of the $ZnO/MgZnO$ MQW heterostructures	138
5.3	STEM-HAADF image of a $ZnO/MgZnO$ atom probe specimen	139
5.4	PL signal of $ZnO/MgZnO$ MQW heterostructure, without bias	143
5.5	Mass spectrum related to the tip A2	145
5.6	Distribution of multiple-ion events	147
5.7	Hitmaps of the Zn atomic fractions and the Zn^{2+}/Zn^+ CSR	149
5.8	3D volume reconstruction of the tip A2 with both the Mg^{2+} and Zn^{1+or2+} ions	150
5.9	Mg II-site fraction profile measured along the m -axis direction	151

5.10	<i>Mg</i> II-site fraction profiles measured along the <i>a-axis</i> direction	152
5.11	<i>Mg</i> II-site fraction profiles measured along the <i>m-axis</i> direction	152
5.12	PL spectra of the “ <i>in-situ</i> ” μPL -APT analysis	154
5.13	Series of spectra, detected during the μPL -APT analysis of the tip A2	155
5.14	Representation of the differential spectra in a 2D color-map	156
5.15	Results of the coupled μPL and APT analysis of the ZnO/MgZnO heterostructure	158
5.16	Effect of the field-induced stress on the <i>PL</i> emission of the <i>ZnO</i> substrate	162
17	The mass spectrum related to the tip A3. The elaboration of the APT-data was realized by Pradip Dalapati.	D
18	Distribution of multiple-ion events associated to the mass spectrum presented in fig 17. 87% of the total events is associated to single events, while the remaining 13% is associated to multi-ions detection.	E
19	Hitmaps of: (a) the <i>Zn</i> atomic fractions visualized through detector statistics and (b) the Zn^{2+}/Zn^{+} charge state ratio (CSR).	E
20	(a) 3D volume reconstruction of the tip A3 with both the Mg^{2+} and Zn^{1+or2+} ions, on the left side, and 3D virtual reconstruction just with the Mg^{2+} and Zn^{1+} ions, on the right side. (b) 2D-distribution of the <i>Mg</i> II-site fraction, calculated over a volume of $(30 \times 30 \times 40) nm^3$	F
21	(a) Series of spectra, detected during the μPL -APT analysis of the tip A3, where the spectral components progressively disappear due to the evaporation of the tip. (b) Differential spectra of the tip A3 represented in a 2D color-map: the <i>red-shift</i> of the signals related to the QWs and barriers are highlighted by the two yellow lines.	H

List of Tables

2.1	Mechanical properties of single-crystal diamond and CVD diamond . . .	50
2.2	Non-linear mechanical properties of diamond	51
2.3	Thermal and electrical properties of different types of diamond	54
3.1	Geometrical parameters of the diamond needles: Tip 1 and Tip 2 . . .	73
3.2	Geometrical parameters of the diamond needles: Tip 2 and Tip 3 . . .	90
3.3	Geometrical parameters of the diamond Tip 4.	101
4.1	Structural and optical characteristics of ZnO , MgO and $Mg_xZn_{1-x}O$.	118
4.2	Second-order elastic coefficients of bulk ZnO	133
4.3	Deformation potentials of ZnO	134
5.1	Geometrical parameters of the $ZnO/MgZnO$ MQW heterostructures . .	138
5.2	Table structure of the collected data during the coupled <i>in-situ</i> μPL - APT experiment	144
5.3	Parameters given by the APT 3D-reconstruction	148
5.4	The Mg II-site fraction evaluated as the profiles in figure 5.10.	153
5.5	The QWs size, evaluated by the Mg II-site fraction profiles in figure 5.11.	153
6	Tip A3 parameters given by the APT 3D-reconstruction: <i>projection</i> <i>point</i> , $F \cdot k_f$ <i>factor</i> , <i>curvature factor</i> , <i>detection efficiency</i>	D
7	The Mg II-site fraction.	G
8	QWs size of the tip A3	G

Introduction

Laser-assisted Atom Probe Tomography (La-APT) technique is a unique tool which allows for the 3D analysis of materials with nearly atomic resolution and chemical sensitivity close to one atomic part per million. The working principle of APT is the triggered field evaporation of atoms, which corresponds to applying an electric field so strong to overcome the binding force between the atoms on the surface of the specimen of interest. A sufficiently high positive electric field ($\approx 10\text{V}/nm$) generates the emission of atoms from the surface of the probed materials. This strong electric field is generated by applying a high voltage to the samples, which needs to have a needle shape, with an apex radius $< 100\text{ nm}$. The field-evaporation of the ions, triggered by laser pulses is used with success in order to probe semiconductors or high resistivity nanomaterials [1]. The application of the electric field induces a large stress propagating inside the sample, which is a reason for frequent sample fracture in APT analyses. In order to control the evaporation of the ions and the stress applied on the probed needle-shaped specimens, a good evaluation of the applied electric field is needed. This technique has the limit to probe the structural and compositional properties of the analyzed materials, while physical (*e.g.* optical, mechanical...) properties related to materials analyzed have to be assessed by complementary means. By these instrumentation constraints came out the idea, reported in *L. Mancini's thesis*, to develop a *correlative multi-microscopy approach*, which relies on La-APT and on Scanning Transmission Electron Microscopy (STEM) to get the structural/compositional/morphological properties and on the micro-photoluminescence (μPL) spectroscopy for the assessment of the optical properties, of the same nanoscale specimen. The μPL setup gives access to the optical properties of the probed material, but it also has two main restrictions to take into

account:

1. the probed materials need to have optically active centers;
2. the limit of the spatial resolution of this technique is given by the laser-spot size that impings on the specimens.

In this thesis, we focused on the correlation of structural and optical properties of specimens of selected materials systems, probed by a coupled “*in-situ*” La-APT/ μ PL instrument. The coupling of the La-APT technique with a μ PL bench allows to use the same laser pulses for triggering the evaporation of ions from the surface of a needle-shaped specimen and simultaneously to generate a photoluminescence signal which can be collected during the APT analysis. This approach has the advantage to collect, at the same time, on a single specimen, information related to its:

- structure;
- composition;
- optical properties.

In this instrument, the evolution of the PL signal during the APT analysis is a source of unprecedented information, which enable to correlate the optical properties of a nanoscale object and its structural properties, yielding important information that can be exploited for the understanding of the mechanisms of light-matter interaction and for better understanding the physics of photoemission, under high electric fields.

An example of application of the “*in-situ*” technique is reported in E. di Russo’s thesis [1] for the analysis of the non-uniform composition in the barriers of the $ZnO/Mg_xZn_{1-x}O$ Multiple Quantum Wells (MQWs) heterostructure. The results obtained by the coupled La-APT/ μ PL system were compared with STEM analysis.

As it will be better explained in the **Chapter 1**, the coupling of the La-APT with the μ PL system within the same instrument imposes the following constraints to the specimens:

- be needle-shaped tips with a nanometric-size apex radius;

- preserve a strong optical signal.

For this last reason, the materials selected for this thesis contain optically active defects or light emitters, based on quantum confinement (quantum emitters) and they are:

- PECVD-diamond nanoneedle-shaped tips with color centers, among which the NV^0 center, about which is reported in **Chapters 2**;
- ZnO/MgZnO MQWs heterostructures, about which is reported in **Chapters 4**.

The NV^0 color centers are among the most studied color centers in literature. These centers are of particular interest for their application in quantum information, exploiting their optical property to act as single-photon-emitters, but they can find also interesting application as field-stress sensors, as demonstrated by the work of Bluvstein *et al.* [2], while in the work of Davies *et al.* [3], the relationship between the displacement of the electronic levels of these color centers and the uniaxial stress acting on them, along a specific diamond crystalline direction, is given. The coupled “*in-situ*” La-APT/ μ PL system was used to study the influence of the electric field on the fine structure of some color centers, embedded into the diamond needles. Thanks to the coupled “*in-situ*” approach, it was possible to observe as function of the applied electric field how it changed the optical emission of these centers. Combining this observations with the previous work of Davies *et al.* [3], then, an original method to perform contactless piezo-spectroscopy of nanoscale systems under uniaxial tensile stress generated by the electric field was developed. This new method was exploited also to study another color center, which nature is still not clear in literature [4, 5, 6], emitting at 2.65eV, and more sensitive than the NV^0 color centers to the stress/strain field. The results about these studies are explained in **Chapter 3**.

The ZnO/MgZnO MQWs studied are constituted by quantum wells of thickness in the range between $\approx [1.5; 3]$ nm which are separated to each other by barriers of average thickness ≈ 45 nm. By probing these samples with the coupled “*in-situ*” La-APT/ μ PL system it was possible to follow in real-time and to reconstruct, at the end of the analysis, the evolution of the optical signal of the heterostructure during its evaporation and so, to observe how the optical signal of the specimen changes between

a quantum well and the next one, with a spatial resolution below the threshold of the μ PL diffraction limit. The results of these analysis are reported in the **Chapter 5**.

Chapter 1

Experimental Methods

1.1 Microphotoluminescence

Micro-photoluminescence (μPL) is the technique which was used in this work for characterizing the optical properties of the studied systems. In this section, the physics of photoluminescence is briefly discussed within the framework of band theory along with the fundamental aspects of μPL and time-resolved PL (TRPL) experiments. Typical constituents of $\mu PL/TRPL$ experimental setups are described and the specifications of the photoluminescence optical setup developed for this work are reported.

1.1.1 Principles of photoluminescence

Photoluminescence (PL) is the physical phenomenon for which, following the absorption of light in the UV/visible range, a system emits photons again in the UV, visible and IR range of wavelengths. This induced emission can be exploited for studying the optical properties of semiconductors, as the incident photons generate free electrons and holes (section 4.1.3 of Chapter 4) within the crystal, which can eventually recombine at energies which reflect the band structure and properties of the system. In a typical photoluminescence experiment, an excitation laser in continuous or pulsed mode is focused on the analyzed sample with controlled wavelength and incident power. The resulting emitted PL signal is collected within different possible geometries and sent

on the diffraction grid of a spectrometer equipped with a charge-coupled device (CCD) camera, which allows for analyzing its intensity as a function of the wavelength (obtaining a time-integrated, energetically resolved spectrum). Such experimental procedure is referred to as PL spectroscopy and its principles are schematized in figure 1.1. When

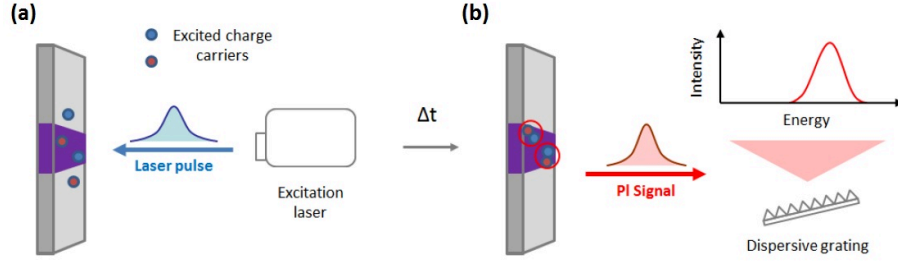


Figure 1.1: Illustration of PL analysis: (a) a laser pulse is sent on a heterostructured specimen, generating electron-hole pairs. After Δt , characteristic time of the radiative recombination process within the system, (b) a PL signal is emitted and energetically dispersed on a diffraction grating. The collected dispersed signal allows for obtaining a spectrum for time-integrated signal as a function of the energy.

the incident laser interacts with matter, it triggers different processes characterized by different probabilities. These processes can be distinguished by the nature of the scattering process, elastic or inelastic, by the number of emitted photons, single or multiple emission, and by the nature of the emission, coherent or incoherent. The PL emission stems from the incoherent, spontaneous inter-band recombination of electrons and holes, allowing obtaining experimental access to different physical quantities, depending on the nature of the system studied. For simple bulk semiconductor systems, PL spectroscopy has been traditionally used for addressing experimentally different properties of semiconductors, such as band gaps, defects, exciton fine structure and donor-acceptor pairs among others. The carriers excited by photons, whose energy is higher than the system bandgap, relax reaching the lowest energies of the conduction and valence bands before recombining radiatively. It is worth noting that emission is obtained most efficiently in direct band gap semiconductors, namely semiconductors for which the minima of the conduction and valence bands are found along the same directions in reciprocal spaces (usually the Γ valley). In systems with indirect band gaps, the electron-hole

pairs recombination happens in a phonon-mediated process, where the lattice phonons compensate the momentum difference independently of their energy, causing a broadening of the PL spectrum along with a strong decrease of the probability of a radiative process. Moreover, even for direct band gap semiconductors, the PL emission can be characterized by a lower energy with respect to the band gap, as defects and impurities can lead to the formation of intra-gap levels from which electrons and holes can recombine at lower energies (*e.g.* section 2.5.2 in Chapter 2) and charge carriers can form bond states (*e.g.* subsection 4.1.2 in Chapter 4), before recombining at the energy of the bandgap minus the binding energy. PL spectroscopy gives access to the energies at which electrons and holes recombine within wide bandgap materials. For instance, in this work we focused on two kind of samples:

- diamond nanoneedles with optically active defects, known as color centers (reported in Chapters 2 and 3);
- ZnO/MgZnO MQWs heterostructures (reported in Chapters 4 and 5).

In figure 1.2 are represented different recombination mechanisms previously described, namely electron-hole pair recombination for (a) the electronic emission of a direct bandgap material, (b) the case of excitonic emission, (c) charge carriers populating an intra-gap level and (d) the case in which the process happens within an heterostructure. Purple arrows indicate the laser excitation, red arrows the PL emission and black dashed arrows the thermalization processes associated with the emission of phonons. The black full line in (b) indicates the intra-gap level associated to a defect state. In (d), the two purple dashed arrows represent two possible excitation mechanisms, namely the case of carriers excited in the matrix and the one of direct excitation of electrons and holes within the heterostructure. The study of the PL emission dependencies on polarization, impinging laser power and temperature can give information on the polarized nature of radiative recombination centers, on the nature of recombining bond states and on the localization of charge carriers, respectively. Let alone the interest of controlling the temperature of the analyzed systems for studying how the optical properties depend on it, the control over this experimental parameter within a PL acquisition is important, as low temperatures reduce the probability of having electrons and holes recombining

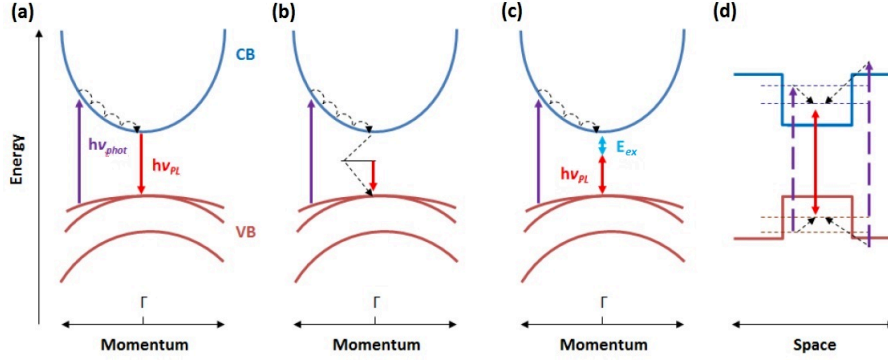


Figure 1.2: Excitation of electron-hole pairs and consequent radiative recombination for a bulk semiconductor in the case of (a) direct recombination of electron and hole at their groundstate energies, (b) in presence of defects which lead to the formation of an intra-gap energy level and (c) after the formation of a bond state with binding energy E_{ex} . The image (d) shows the recombination within a heterostructure of electrons and holes generated either in the matrix or in the heterostructure.

far from the position in which they have been generated and within defects-induced nonradiative recombination centers, thus allowing for stronger PL signals. The way in which the laser excitation is focused onto the sample is also important: the optical path can be designed in such a way that the laser is focused on the sample in a spot whose dimensions are of the order of $1\ \mu m$ (or less, the lowest dimensions being defined by the diffraction limit as $d = \frac{\lambda}{2NA}$, where λ is the light wavelength and NA is the system numerical aperture). This, along with the possibility of moving the sample with respect to the laser path, allows for exciting the analyzed sample in specific positions and to spatially resolve the optical properties of the system, the spatial resolution being determined by the laser spot size ($d_{spot} \approx 1-1.5\ \mu m$). PL acquisitions performed in this last configuration are commonly referred to as micro-photoluminescence (μPL). The μPL system gives the optical signature of the analyzed material, but it loses information related to the morphological properties of the probed materials on length scale below the laser spot size. In section 1.3, the μPL system is coupled “*in-situ*” with the technique introduced in section 1.2. This original setup allows to correlate the optical and morphological properties of the probed samples on the length-scale of $< 100\ nm$.

1.1.2 Experimental study of photoluminescence signals

Experimental PL setups are conceived for ensuring, along with the possibility of exciting the sample and of collecting a good emitted signal, the control over the physical parameters which come into play in the PL process.

Excitation:

Excitation is provided by a laser operating either in continuous-wave or in pulsed mode. The first category of lasers provide a continuous excitation of the material with a constant light output power in time (different noise sources can cause involuntary deviations from the average) and with the instantaneous power equal to the time-averaged one. The second category of lasers emit light pulses of fixed duration and at regular frequencies (repetition rate). Two main operation modes exist, namely Q-switching [7, 8], allowing for a pulse temporal full width at half maximum (FWHM) of 50-100 *ps*, and Mode-locking [9, 10], whose pulses duration can go down below 100 *fs*. Typical repetition rates can go from 50 *GHz* down to few *Hz* and the instantaneous power is anti-proportional to the pulse duration and repetition rate. Tunable lasers and non-linear optical processes (second and third harmonic generation (S/THG)) can be used in order to have access to different excitation energies. The impinging power on the sample can be monitored using a power-meter and tuned using the combined effects of a polarizer and a half-waveplate (polarization rotator). Filters are commonly used for ensuring a monochromatic excitation. In this work, a pulsed laser in mode-locking mode was used to performed the experiments through the instrument described in section 1.3.

Laser focusing and signal collection:

Once the PL signal is emitted, it has to be sent to the detection system. Integrating spheres can be used for some applications (*e.g.* measurement of the quantum yield [11]), even if they are not applicable for μPL spectroscopy and for low temperature ($T \approx 25K$) measurements. In the present case a hemispherical mirror put behind the specimen is used in order to reflect and focus the excitation laser on the sample, allowing the collection of the emitted signal on the same optical path. Using beam-splitters and filters

the PL signal can then be separated from the laser wavelengths for being detected.

Temperature control:

The temperature of the analyzed sample can be controlled by enclosing it in a cryostat. Different technologies exist, such as cold-finger and bath-type cryostats. In the present work, the sample was kept inside an ultra high vacuum chamber (APT chamber), at tunable T, within the range: [25; 300] K, on a piezo-mechanical positioning stage, which is connected to the cold finger cryostat. The cooling of the sample is thus obtained by conduction. The interaction between liquid Nitrogen and the stage is ensured by the circulation of the former within a circuit which can either close (closed-loop cryostat) or open (open-loop cryostat). While in the first configuration the liquid Helium never leaves the cooling circuit, in open-loop cryostats a constant supply of Helium coming from an external dewar is needed. The high pressure of He vapor inside the dewar forces the liquid He phase to circulate within the refrigerated enclosure and then leave the cryostat in the gaseous phase. The temperature within the cryostat is measured by means of a calibrated thermocouple or thermal diode sensor. Temperature controllers equipped with an heater for fixing the temperature at a specific value are commonly used.

PL signal detection:

The collected PL signal is eventually sent to a spectrometer for the spectrum analysis. Even if alternatives detection methods exists, such as Fabry-Perot [12] or Michelson interferometric [13, 14] techniques coupled with single channel detectors (*e.g.* avalanche diodes), modern spectrometers normally relies on a diffraction grating which allows for the dispersion of the detected signal, which is then detected by a CCD cooled with liquid Nitrogen or with a Peltier element. Different grating periods ensure different resolutions and signal bandwidth, as longer periods allows for a larger bandwidth at the cost of a decrease in resolution and vice versa. For instance, the dispersed signal can be sent to a streak camera instead of to the CCD. For obtaining the time-resolved spectra, a supplementary pulsed light source (photo-diode) synchronized with the excitation pulses (same repetition rate) has to be added to the experimental setup for triggering

the time-dependent deflection of photo-generated electrons.

1.1.3 μPL experimental setup

In figure 1.3 is reported the simplified layout of the μPL setup which has been used in this work for characterizing the optical properties of color centers in diamond and low dimensional semiconductors. The experimental setup consists of tunable Ti:Sapphire oscillator operating in mode-locking mode, which emitting pulses with a repetition rate of 80 MHz and within a wavelength range going from 680 to 1080 nm (red lines). Higher energies are obtained by means of nonlinear crystals for SHG and THG. Typically, μPL acquisitions were performed fixing the laser output at 780 nm and selecting the third harmonic for exciting the sample (260 nm). A pulse picker is employed before the SHG/THG system for selecting only one peak out of 20 and thus reducing the repetition rate to 4 MHz . This lower pulse frequency allows operating the streak camera and brings the repetition rate closer to those commonly used in atom probe tomography (this was originally important for confirming the feasibility of the “*in-situ*” APT/ μPL analysis, as at lower repetition rates correspond lower time-integrated PL signal intensities). The beam leaving the SHG/THG system (blue lines) can be filtered by an opportune high-pass filter in order to block the undesired wavelengths (*e.g.* if the third harmonic is selected, a filter blocking the first and the second harmonic is used) and sent through an achromatic beam splitter to an adonlyable reflective objective for UV-visible light, with 36X magnification, 0.5 numerical aperture and working distance of 8.6 mm . The excitation laser is thus focused on the sample through a hemispherical mirror positionated at $\approx 2.3\text{ cm}$ from the specimen position. The radius of the laser spot is close to the diffraction limit. Samples are inserted in copper cylindric stages of a high stability, which compose the multi-axis positioning stages. A temperature controller allows fixing the temperature of the sample within the range $25\text{-}500\text{ K}$. The position of the laser spot with respect to the sample is controlled thanks to an imaging system consisting of a CCD camera and a light source (photo-diode) which allows visualizing the two, and a multi-axis positioning stages which allows for moving the specimen, inside the ultra-vacuum (U.V.) chamber, through a piezoelectric mechanism. The emitted

PL signal (yellow lines) is collected by the spectrometer after having been filtered for removing the excitation laser components. A polarizer can also be placed before the spectrometer entrance for studying the polarization of the emitted signal. The 320 mm focal length spectrometer is equipped with 300, 600 and 1200 nm⁻¹ gratings and a liquid Nitrogen cooled CCD detector, allowing for a spectral resolution of 0.06 nm. For the acquisition of time-resolved PL spectra, the dispersed signal is sent to a streak camera with spectral response of 200-850 nm and temporal resolution lower than 1 ps.

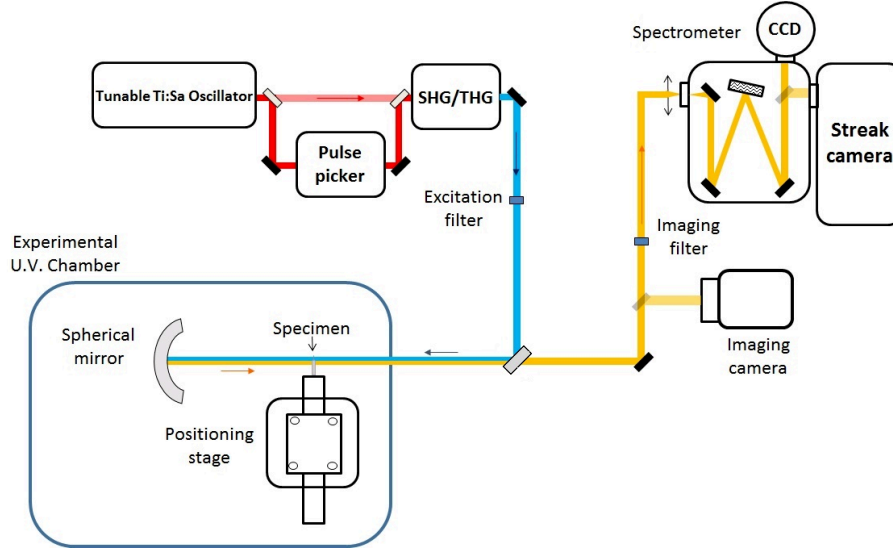


Figure 1.3: Simplified layout of the photoluminescence optical setup used for $\mu(TR)PL$ analyses. The red, blue and yellow beams represent respectively the excitation laser at the original wavelength of the Ti:Sa oscillator, after having passed through the SHG/THG system and the emitted PL signal.

1.2 Laser-assisted Atom Probe Tomography

In this section the experimental technique employed for the structural and morphological characterization of the analyzed *ZnO/MgZnO* specimens is introduced. First, an introductory background is dedicated to the working principle of the Atom Probe Tomography (APT) and then the reasons of the development of Laser-Atom Probe To-

mography (La-APT) for the study of nonconductive materials (such as semiconductors, oxides... [15]) will be explained. The consequences of the laser-specimen interaction on the APT performances will be discussed in the subsection 1.2.3.

1.2.1 Atom Probe Tomography

APT is a destructive microscopy technique which allows for the 3D analysis of materials with near-atomic resolution and maximal chemical sensitivity close to one atomic part per million. In figure 1.4, the working principle of the atom probe technique is schematically represented.

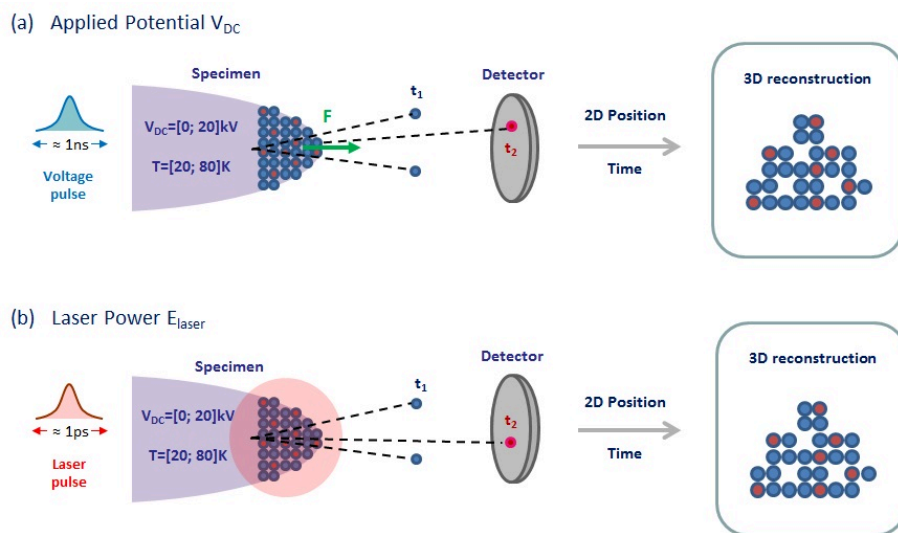


Figure 1.4: Schematic of the working principle of atom probe tomography. Single atoms (red and blue dots) are field evaporated from a field emission tip under the effect of (a) voltage or (b) laser pulses and flight to the detector under the effect of the applied DC field. Atoms of different species reach the detector with different times of flight. The 2D spatial information of the position of the impacts and the recorded times of flight are used for obtaining a 3D reconstruction of the sample. The 3D reconstructed APT sample takes into account the non unitary of the detector efficiency (see section 1.2.6).

The working principle of APT is the triggered field evaporation (section 1.2.2) of atoms, which corresponds to applying an electric field so strong to overcome the electrostatic field existing between the atoms on the surface of the specimen of interest. A

sufficient positive electric field ($\sim 10 \text{ V/nm}$) generates the emission of atoms from the material surface. To create this strong electric field, the positively polarized samples need to have a needle shape, with an apex radius $< 100 \text{ nm}$. The atoms evaporated from a needle-shaped specimen are finally detected on a position- and time-of-flight-sensitive detector. The position on the 2D detector along with the knowledge of the evaporation order allow reconstructing the 3D position of detected atoms within the reconstructed volume, while their chemical nature can be deduced by time-of-flight spectroscopy (section 1.2.4) of the ions accelerated by the constant electric field. The field evaporation of the ions can be triggered in two ways: by voltage pulses or by laser pulses. In the voltage pulse mode, the evaporation probability of the most protruding ions is greatly increased by the superposition of potential pulses with a temporal width of the order of few ns to the constant potential applied to the sample. The additional field lowers the energy barrier confining the surface atoms so that for the short duration of the pulse the evaporation rate is higher. In laser pulse mode, the ion evaporation is triggered by the interaction with the specimen of a pulsed laser, with sub- ps pulses duration, whose main effect is to locally increase the specimen surface temperature in a phonon mediated absorption process and thus temporarily increasing the thermal energy of surface ions, increasing their probability of tunneling through the confining energy barrier or passing over it [16, 17]. It is worth noting that the voltage pulse mode allows for the analysis of metallic systems only, as in non-conductive systems the pulses are strongly distorted (lowered maximal amplitude and longer duration) so that they are no longer able to properly trigger the field evaporation. The introduction of the laser pulse operating mode, and of the so-called laser assisted atom probe tomography (La-APT), opened to the possibility of analyzing high resistivity materials such as semiconductors [18], oxides [19] and polymers [20]. In the following, the main aspects and features of APT are discussed in more details: the physics governing the field evaporation of atoms is described within the context of APT experiments. Different APT operating modes, along with the way in which the chemical and structural information is extracted by APT data are also discussed. Different involved resolutions and detection capabilities are considered. Finally, the methods and numerical tools used for exploiting the structural information within the correlative approach are reported.

1.2.2 Physics of field evaporation

The *field evaporation* of ions from the surface of materials, under the effects of strong electric fields, is the physical phenomenon underlying the triggered evaporation and consequent detection of charged particles (atoms and molecules), during APT analyses. The relationship between the applied potential and surface field is given by the equation (1.1):

$$F = \frac{V}{k_f \cdot R} \quad (1.1)$$

where R is the surface curvature radius and k_f is the field factor, a semiconstant which accounts for both the geometry of the emitter and its electrostatic environment. The particular geometry of field emission tips ($R \sim 50 \text{ nm}$) allows for the creation of surface fields strong enough for deforming the most external atomic layers to a point in which atoms can leave the surface as ions. From the point of view of one of the protruding atoms, this can be seen as a barrier-crossing process, which can thus be empirically described by the following Arrhenius-like crossing rate:

$$K = \nu_0 \cdot \exp\left(-\frac{Q(F)}{k_B \cdot T}\right) \quad (1.2)$$

where ν_0 is the vibration frequency of the evaporating atom and $Q(F)$ defines the field depending energy barrier. A relative simple 1D classical description of the energy barrier was proposed by Muller [21] as the difference between the surface atom binding energy Λ and the maximum potential energy of an ion close to the surface U_{MAX} . The ion potential energy as a function of the distance from the surface can be written as:

$$U(z) = \left(\sum I_n - n \cdot \phi\right) - \frac{n^2 \cdot e^2}{16 \cdot \pi \cdot \epsilon_0 \cdot z} - n \cdot e \cdot F \cdot z \quad (1.3)$$

where $\left(\sum I_n - n \cdot \phi\right)$ is the energy necessary for ionizing the atom (I_n and ϕ being respectively the n -th ionization energy and the electronegativity of the surface). The second term describes the attractive potential induced by the ion electrostatic image and the third term is the repulsive electrostatic force caused by the positive applied

field. The maximum potential energy of the ion can be written as:

$$U_{MAX} = \left(\frac{n^3 \cdot e^3 \cdot F}{4 \cdot \pi \cdot \varepsilon_0} \right)^{1/2} \quad (1.4)$$

so that the energy barrier $Q_n(F)$ is:

$$Q_n(F) = \left(\Lambda + \sum I_n - n \cdot \phi \right) - \left(\frac{n^3 \cdot e^3 \cdot F}{4 \cdot \pi \cdot \varepsilon_0} \right)^{1/2} \quad (1.5)$$

where Λ is the bonding energy of the surface atom. From the equation (1.5), the *evaporation field* F_{evap} , corresponding to $Q_n = 0$ can be defined as:

$$F_{evap} = \frac{4 \cdot \pi \cdot \varepsilon_0}{n^3 \cdot e^3} \cdot \left(\Lambda + \sum I_n - n \cdot \phi \right)^2 \quad (1.6)$$

for $F \approx F_{evap}$, the equation (1.6) can be rewritten as:

$$Q_{evap,n}(F) = \frac{Q_{0,n}}{2} \cdot \left(1 - \frac{F}{F_{evap}} \right) \quad (1.7)$$

where $Q_{0,n} = Q_n(0) = \left(\Lambda + \sum I_n - n \cdot \phi \right)^2$. While being able to reproduce experimental results in some particular cases, this model is not able to fully grasp the complexity of field evaporation processes, its main drawbacks being the lack of a realistic modeling of the potential seen by the evaporating atom close to the surface and the fact that the distribution of the local surface electric field is not taken into account. More realistic models describe the way in which under the effects of the field the surface is deformed, leading to a continuous variation of the charge carried by the atoms undergoing the field evaporation process. More precisely, surface (protruding) atoms can be described as partial ions subjected to a field-induced Maxwell stress, defined as:

$$f_M = \frac{\varepsilon_0 \cdot F^2}{2} \quad (1.8)$$

caused by the intrinsic inter-repulsion of surface charges, so that the potential barrier which has to be crossed by the ions can be seen as due to contributions from a classical atomic energy barrier (universal binding energy curve [22, 23]) or an analytically estimated atom/surface pair potential (Morse potential [24]), and the electrostatic potential of the field-dependent ion partial charge $q(F)$. A complete description of the phenomenon should also take into account the 3D atomic configuration characterizing the surroundings of the evaporating atoms (modifying the local potential), along with the effects of temperature and surface diffusion, contributions which can be studied by different approaches such as molecular dynamics simulations [25, 26]. During an APT experiment, atoms are evaporated from a surface whose characteristics are determined by the crystallography of the system and by the sample preparation process. The most protruding atoms are those subjected to the highest surface field and consequently those with the highest probability of being field evaporated. This behavior can be described by rewriting the evaporation rate considering equations (1.2) and (1.7) as the following relationship:

$$K = N' \cdot \nu_0 \cdot \exp\left(-\frac{C \cdot (1 - F/F_{evap})}{k_B \cdot T}\right) \quad (1.9)$$

where $C = Q_0/2$ and N' defines the number of atoms which feel a surface field which is high enough for triggering their field evaporation. The given relationship is valid until F is equal to 20% of F_{evap} , while for less intense electric fields, this relationship is not valid. The rate defined in equation (1.9) is not directly observed in experiments, as the reduced field of view of the instrument and the non-unity detection efficiency influence the detection rate. The equation 1.9 was expressed in terms of F_{evap} , the extrapolated voltage value for which atoms can be evaporated at a good rate at $T = 0 \text{ K}$. For a given surface field, when the temperature of the system is increased, the evaporation rate also increases, as the atoms can cross the energy barrier by thermal activation. It can thus be convenient defining the quantity F_T which corresponds to the threshold surface field for $T \neq 0$ and for a fixed rate K_T [27] as:

$$\frac{F_T}{F_{evap}} = 1 - T \cdot \left[\frac{k_B}{C} \cdot \left(\frac{N' \cdot \nu_0}{K_T} \right) \right] \quad (1.10)$$

where the slope of the linear dependence on T depends on the atom binding energy through C (variations from linearity can be experimentally observed [28] because the binding potential form from which the equation (1.10) is derived relies on a certain number of approximation). In the next section, the laser-assisted field evaporation mechanism is addressed.

1.2.3 Laser-induced field evaporation

The laser/matter interaction which is at the core of La-APT is a complex phenomenon which involves different physical processes depending on the nature of the analyzed material, on the geometry of the specimen and on the constant DC field applied to it. As previously introduced, the main merit of La-APT is allowing analyzing material systems for which the voltage pulse triggering of ions field evaporation is not possible. Nevertheless, the laser pulse operation mode can be extremely useful for applications in the study of metallic materials, as it can ensure better performances with respect to electrical APT in terms of mass resolution and field of view at condition that the illumination conditions are properly tuned [29]. From the point of view of La-APT, the main difference between metallic and non metallic materials is the way in which they interact with light: in metals, photons excite electrons to higher levels within the half-filled conduction band. These eventually thermalize to lower states interacting with other electrons or phonons, increasing the temperature of the system. In semiconductor systems the electron-light interaction is more complex, as it reflects their complex electronic structure. The analyzed specimen is more or less transparent to the incident laser (the light penetration depth is also affected) depending on the photon energy and bandgap. Also for semiconductors the absorption of light leads to the increasing of the system temperature, as generated charge carrier pairs recombine through phonon-mediated processes. Additional complexity stems from the particular geometry of APT specimens, this being related to the capacity of the system to locally absorb light. Nonuniform absorption maps can be obtained solving the Maxwell's equations for the 3D field emission tips volume, showing that depending on the material and on the laser direction and properties, photons can be absorbed in preferential posi-

tions on the surface (metals and semiconductors) and within the bulk with complex distributions of absorption spots (only semiconductors). The applied surface field also influences the absorption properties of the sample, as it affects the band structure at the sample/vacuum interfaces. The physical effects which enter in play in the different mentioned cases along with the effects of different fields and laser properties will not be discussed here in more detail. For more detailed information refer to [30, 29, 31, 32].

1.2.4 Time-of-flight mass spectroscopy

Within an APT analysis, after having left the surface, a field evaporated ion is subjected to the strong electric field induced by the potential difference V_{DC} existing between the specimen surface and the detector. The kinetic energy of the evaporating ion can be considered to be null only after the crossing of the energetic barrier. Under the effects of the acceleration induced by the electric field, the ion acquires a kinetic energy which equals the electrostatic potential corresponding to V_{DC} :

$$\frac{1}{2} \cdot m \cdot v^2 = n \cdot e \cdot V_{DC} \quad (1.11)$$

and thus starting to flight towards the detector at speed:

$$v = \left(2 \cdot \frac{n \cdot e \cdot V_{DC}}{m} \right)^{1/2} \quad (1.12)$$

Typical applied potentials range between: $V_{DC} = [1; 20] \text{ kV}$, the ion acquires the total kinetic energy given by (1.11), within a distance from the surface which is negligible with respect to typical flight lengths (specimen-detector distance) $L = 0.1 - 0.5 \text{ m}$, so that the ion can be considered as flying with unchanged velocity along all the flight path. The time-of-flight (TOF) of the ion, corresponding to the time needed for traveling from the surface to the detector can then be easily derived as:

$$t = L \cdot \left(\frac{m}{2 \cdot n \cdot e \cdot V_{DC}} \right)^{1/2} \quad (1.13)$$

During an APT acquisition, the elapsed time t_m measured between the generation of the laser pulse and the detection of each event is registered (typically within the $[1; 5]\mu s$ range), so that for each ion the mass over charge ratio M is established:

$$M = \frac{m}{n} = 2 \cdot e \cdot V_{DC} \cdot \left(\frac{t_m}{L} \right)^2 \quad (1.14)$$

allowing associating at each detected ion its chemical species. The histogram of all measured M values define what is referred to as mass spectrum. Mass spectra are characterized by peaks which can be ascribed to ions with corresponding mass over charge ratio, evaporated during a triggering pulse (peaks indexing). Ions evaporated in-between pulses constitute the background noise of the spectrum. The mass resolution of the technique is directly related to the broadening of the peaks which is affected by several different contributions, both instrumental and related to the physics of field evaporation. Mass spectra are optimized by means of statistical corrections which take into account different contributions, such as the different flight paths on different positions of the detector and the varying voltage applied to the tip. Further discussion of the calibration of the instrument, the different sources of incertitude for the determination of M and the corrections used for optimizing the mass spectra is beyond the aims of this thesis. For more detailed information on these topics refer to [33]. Depending on the analyzed material, mass spectra of different complexity from the point of view of their interpretation can be obtained. Ideally, there should not be overlapping between peaks associated to different ion or molecular species. If they do overlap, the relative contributions to single peaks still might be estimated by their deconvolution on the basis of the isotopic abundancies of different chemical species.

1.2.5 Three-dimensional reconstruction of APT data

The APT ability to analyze the 3D structure of materials relies on the capacity of transforming the 2D information of the impact positions on the detector of the field evaporated ions and the temporal information consisting in the ordering of their arrival in the 3D information consisting of the original position of the detected ions within the

reconstructed specimen volume. In other words, the 3-dimensional reconstruction procedure of APT data reduces to passing from the data triplet associated to each detected event $(X; Y; n)$, where X and Y are the position coordinates on the detector of the n -th detected ion, to the set of values $(x; y; z)$, corresponding to the coordinates within the Cartesian reference system of the reconstructed space. The simplest transformation procedure [34] is based on the definition of a magnification parameter η which describes the magnification of the specimen surface image on the detector, for which:

$$x = X/\eta \quad (1.15)$$

$$y = Y/\eta \quad (1.16)$$

Within the approximation of small fields of view, the following simplified expression for the magnification M can be used:

$$\eta = \frac{L}{\xi \cdot r} \quad (1.17)$$

where L is the estimated distance between the specimen surface and the detector, r is the surface radius of the sample and $1 < \xi < 2$ is a projection parameter which is commonly referred to as image compression factor and which takes into account the detection of the ions trajectory (initially perpendicular with respect to the surface) close to the surface induced by the surface field. Consequently, x and y follow from the detector impact coordinates as:

$$x = \frac{X}{L} \cdot \xi \cdot r \quad (1.18)$$

$$y = \frac{Y}{L} \cdot \xi \cdot r \quad (1.19)$$

This simple 2D reconstruction method (point projection reconstruction) for the lateral coordinates of the evaporated ions is schematically represented in figure 1.5 (a). The z coordinate of the i -th ion in reconstructed space is determined considering a variation in its position along the z -axis with respect to the i -th event of:

$$dz_i = \frac{v_i^{at}}{\eta \cdot s} = \frac{v_i^{at} \cdot M^2}{\eta \cdot S} = \frac{v_i^{at} \cdot L^2}{\eta \cdot S \cdot \xi^2 \cdot r^2} \quad (1.20)$$

where v_i^{at} is the atomic volume of the i -th atom within its specific phase, s is the cross

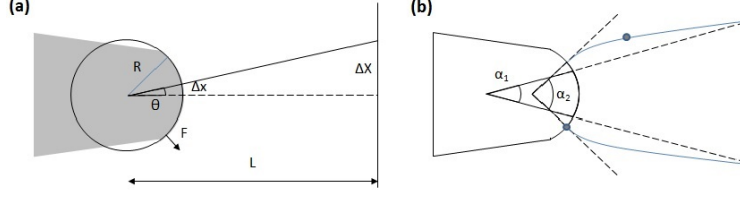


Figure 1.5: Schematic representation of (a) the 2D point projection reconstruction method. In (b), the deflection of ion trajectories due to the applied field are represented, along with the angles α_1 and α_2 which defines the field of view of the technique.

sectional area of the specimen corresponding to the detector area S and η is the detection efficiency of the corresponding ionic species (note that in reconstruction algorithms often an average or phase-related detection efficiency is considered instead). The set of equations (1.18), (1.19) and (1.20) should in principle allow for obtaining the full 3D reconstruction of the atomic positions, given the knowledge of the sample related parameters v_i^{at} and r along with the instrument and experimental conditions related parameters L ; S ; ξ and η . Nevertheless, for obtaining more realistic reconstruction better transfer functions relating detector to reconstructed space coordinates are needed. In APT data treatment, transfer functions relying on a certain number of assumptions above the geometrical shape of the sample and the electrostatic field distribution are used, allowing to overcome the limitations imposed by the small field of view approximation [15]. In order for a transfer function to be able to properly reconstruct more than a few atomic layers, it has necessarily to take into account the fact that during the field evaporation the radius of the specimen increases (this holds also for the simple procedure described here). The evolution of r is commonly estimating from the voltage applied to the tip considering:

$$F = \beta \cdot V_{DC} \quad (1.21)$$

where F is the surface field and β is the field-to-voltage conversion factor, along with eq. (1.1). The parameter k_f , which appears in eq. (1.1), can be estimated if r for a specific applied voltage is independently determined experimentally (*e.g.* by Scanning Electron Microscopy ‘SEM’ or Transmission Electron Microscopy ‘TEM’). This

reconstruction method (commonly referred to as E_β algorithm) leads to reconstruction artifacts when systems containing phases with different evaporation fields are considered. In this case, the evolution of r is usually better accounted for by assuming a specific geometry of the specimen and use geometrical models for determining the relationship between r and dz_i . Algorithms commonly used consider a hemispherical surface mounted over a cone described by a shank-angle and an initial radius (cone angle reconstruction method [35, 36]), or over more complex structures whose geometry is assessed by electron microscopy techniques (tip-profile method). When considering semiconductor heterostructures, information on the structure of the system issued by other microscopy techniques is extremely useful as it allows tuning the reconstruction parameters in order to obtain the best possible reconstruction (*e.g.* case of planar layers in multi-layered heterostructures [37]). A general quantification of the spatial resolution of the technique is not easily obtained as the resolution of the detection systems contributes only marginally to the real capabilities of APT to resolve the position of atoms within the reconstructed space. In fact, the nature of the field evaporation processes and the reconstruction methods are the limiting factors to the spatial resolution. Modern delay line detectors have a spatial resolution (defined as the capacity of distinguishing between two spatially close events on the detector) of the order of [50; 100] μm [38]. Considering typical magnifications of atom probes, this results in a spatial resolution on the plane perpendicular to the reconstruction axis lower than 5 Å. On the other hand, the effective resolution on the xy plane is considerably lower due to the contribution of three main effects:

1. The initial transverse velocity of field evaporating atoms can be different from zero [39], due to thermal agitation at which adatoms are subjected to;
2. When an atom leaves the surface within the evaporation process, its trajectory is influenced by the local atomic configuration of the surface and the corresponding local distribution of field [40];
3. Before being effectively evaporated, atoms can diffuse along the surface (normally high laser energies are needed [41]) or simply interact with neighbor atoms (while

still not being evaporated), slightly modifying their position and thus the flight trajectory (rolling-up motion [42]).

Due to these effects, experimentally observed lateral resolutions are of the order of $1nm$. The ideal spatial resolution along the z -direction is given by equation (1.20) (the inter-distance between successive reconstructed atomic planes) and thus depends on the average atomic volume of the atoms in the crystal and on the detection efficiency. It follows that for typical values of v^{at} and η the ideal in-depth resolution is less than one pm . The real spatial resolution is again considerably lower. The limiting factor in this case is the probabilistic nature of the field evaporation phenomena, or more precisely the fact that an uncertainty in the order of evaporation of atoms exists: an atom subjected to the highest local surface field is not necessarily field evaporated before other atoms subjected to lower field. Considering the number of surface atoms N within a typical tip and the relative rate with which the highest surface field atom is evaporated after n other atoms [43]:

$$\frac{K(n)}{K} = \exp\left(\frac{2 \cdot C \cdot n}{k_B \cdot T \cdot N}\right) \quad (1.22)$$

this uncertainty can be of the order of hundreds of atoms, leading to nearatomic in-depth resolution. It should be noted that what has been said about the APT spatial resolution actually holds for systems constituted by a single phase. The semiconductors considered in this thesis are constituted by regions characterized by different compositions and consequently different evaporation fields. During evaporation, regions with different evaporation fields evaporate with different rates, so that the spatial resolution along all direction is affected: local modifications of the specimen surface induced by the preferential evaporation of specific phases [44, 45, 46] can modify the surface field distribution and consequently the trajectories of evaporating ions, deteriorating the in-plane resolution (*e.g.* see the local magnification artefact [43, 47] affecting the reconstruction). This issue will be discussed more in detail for the analyzed heterostructure $ZnO/MgZnO$ in section 5.2.2 of Chapter 5. while the in-depth resolution is affected by the uncertainty in the evaporation order which follows different evaporation fields.

1.2.5.1 Delay line detector (DLD)

In a conventional DLD systems, as the one used in this work, the electron clouds generated by Multi Channel Plates (MCPs) are received on the two delay lines X and Y, producing each one two analog signals travelling in opposite directions (fig. 1.6).

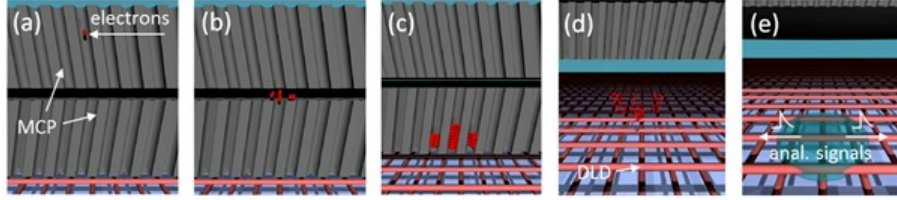


Figure 1.6: Detection dynamic in a conventional DLD system: (a, b, c) an ion impact at the top of the first MCP generates electrons, which are multiplied with a cascade mechanism inside the two MCPs. (d) The generated electronic cloud is extracted at the bottom of the second MCP and absorbed by the DLD. (e) Two analog signals are propagated along each delay line.

As the length of the two delay lines are fixed, the propagation times of the analog signal in each delay line are well known. These strictly depend on the position of electron cloud. In this way, four timing information provide the impact position (x, y) of a detected ion. This position can be back-projected to the tip surface using specially dedicated reconstruction algorithms, allowing to determine the ion position (x', y') on the tip volume. The spatial resolution obtained by a conventional detector is closed to $80 \mu m$ on the MCP surface, which approximately corresponds to less than 1\AA on the tip surface. The evaporation order of atoms allows access to the third dimension z' . Detailed information about the reconstruction algorithms are provided in ref. [15]. In order to determine the TOF, so the chemical nature of detected ions, a fifth time difference must be measured. A detailed scheme of the electronic system used to convert the analog signal in timing information in a conventional MCP/DLD is reported in fig. 1.7.

An analog signal produced by the MCP/DLD is amplified and then transformed in a digital signal by a discriminator. A logic value “1” is generated by this device when the input signal is higher than a fixed threshold value. Lastly, the digital signal

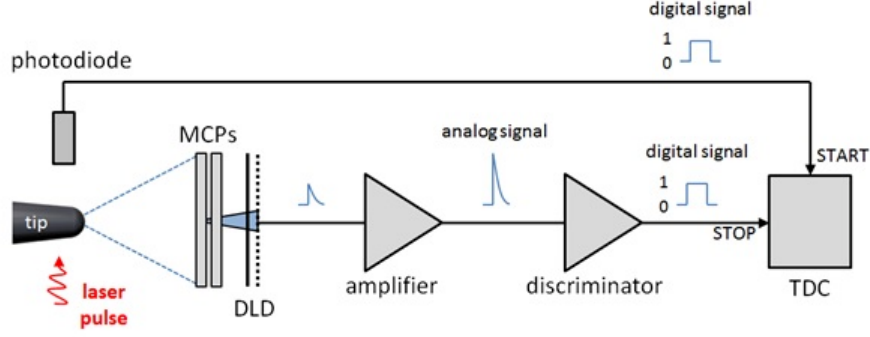


Figure 1.7: Scheme of the electronic system used to measure the impact position of the ions on the MCP in a conventional MCP/DLD.

is sent to a Time-to-Digital Converter (TDC) which calculates the time difference between two digital signals. The first one is provided by a photodiode and starts the timing measurement in correspondence of the arrival of a laser pulse on the tip. The second signal is the one generated by the discriminator, which stops the timing measurement. The TOF interval of an ion corresponds to the time difference between the signal provided by the photodiode (reps. the departure time from the tip) and the signal generated by the MCPs. Clearly, all the timing delays due to the electronic system and the signal propagation on the DLD are taken into account to calculate the TOF. Conventional DLD detectors can provide information for multiple ion impacts. Serial multiple ion impacts corresponding to the arrival of two or more ions which can be detected if their TOF difference is larger than $\sim 4 \text{ ns}$. This value corresponds to the Time Resolving Power (TRP) of the DLD detector. Differently, simultaneous impacts correspond to the arrival of two or more ions with almost the same TOF. If the impact distances on the MCP are lower than the Spatial Resolving Power (SRP), which is $\sim 4 \text{ mm}$ in a DLD detector (corresponding to $\sim 4 \div 0.4 \text{ nm}$ on the tip surface), the signals generated by each ion on the delay lines appear overlapped. Therefore, a single signal, resulting from the superimposing of several signals generated by each ion impact, is amplified. In this case, only one digital signal is generated by the discriminator and sent to the TDC (fig. 1.8(a)). This means that only one impact is detected and the event is recorded as a single ion impact. Nowadays, the detection of multiple

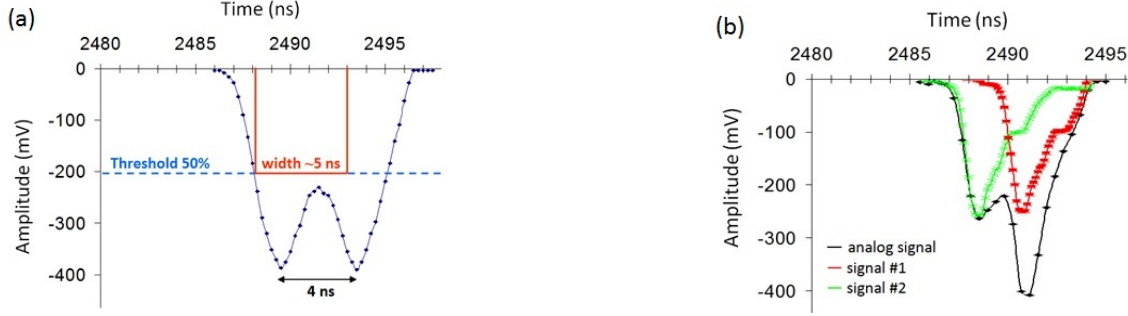


Figure 1.8: (a) Example of the analog-to-digital conversion carried out by the discriminator. A signal consisting of two overlapped peaks separated 4 ns is associated to the detection of simultaneous impacts of two different ions. With a threshold equal to the 50% of the peak value (blue dashed line), only one 5 ns width digital signal is generated (in red). (b) Example of an analog signal (black line) collected on the delay line and processed by an aDLD. The deconvolution of the analog signal reveals two different signals (red and green lines) associated to the simultaneous impact of two ions.

ion events has been improved through the design of an advanced Delay Line Detector (aDLD) [48, 19], which allows decreasing both the Time Resolving Power (TRP) and the Spatial Resolving Power (SRP) to 1.5 ns and 1.5 mm (corresponding to $\sim 1 \div 0.1\text{ nm}$ on the tip surface), respectively, showed in fig. 1.8(b). As a consequence, the detection of multiple ion events is strongly improved.

Therefore, the performance of the experimental system used in this work can be further improved substituting the DLD with an aDLD.

1.2.6 Field of view and detection efficiency

Not all the atoms which are field evaporated from the tip specimen during an APT acquisition participate to the mass spectrometry analysis and/or to the tomographic reconstruction process. Among those which are not evaporated during a voltage/laser pulse and successfully detected, some are accelerated by the surface field towards the detection system but their trajectory ends outside the acceptance angle of the detector. The maximum size of the object that can be observed is defined by the field of view of the instruments. The field of view is defined as a function of three different values,

corresponding to: x , y (lateral directions) and z (depth direction). The length of the specimen which can be probed by the technique depends on:

- a. the geometry of the sample (shank angle), determining the depth of analysis reached before obtaining the maximal tip radius for which a surface field evaporation is attainable;
- b. the maximum DC potential applicable to the sample;
- c. the evaporation field of the system (which again is related to the maximum radius at which atoms can be field evaporated).

The lateral field of view depends on the characteristic of the instruments such as the flight length and the surface of the detection system, but is also influenced by experimental conditions, namely by the applied potential which modifies the ions trajectories [15]. It is commonly defined for an instrument by means of the 2 angles represented in figure 1.5 (b), namely the acceptance angle of the detector with respect to the sample α_1 , and the angle which subtend the section of the surface imaged on the detector with respect to the center of the hemispherical tip head α_2 . Note that the second angle is bigger as the trajectories of the ions leaving the surface are bent in the direction of the detector in the first steps of flight. The total probed volume by a single APT analysis corresponds to the imaged part of field emission tips with apex radius smaller than 200 nm and for depths lower than $1\text{ }\mu\text{m}$. This implies that the features to be analyzed have to be characterized by typical size-scales comparable to the probed volume. When analyzing APT data, the atoms which are evaporated outside the field of view of the detector present no particular problems, as they are simply excluded from the TOF spectra and the reconstructed volume. Much more care is needed when taking into account those ions which are evaporated within the field of view but are not detected, for different ion loss mechanisms (*e.g.* because evaporated in-between the triggering pulses and end up the background noise of the mass spectra). The ensemble of the ions loss mechanisms are schematically represented in figure 1.9. The relative amount of ions belonging to the first category is quantified by the multi-channel plate detection efficiency η_{MCP} , which defines the fraction of atoms which hit the detector, but that are stopped

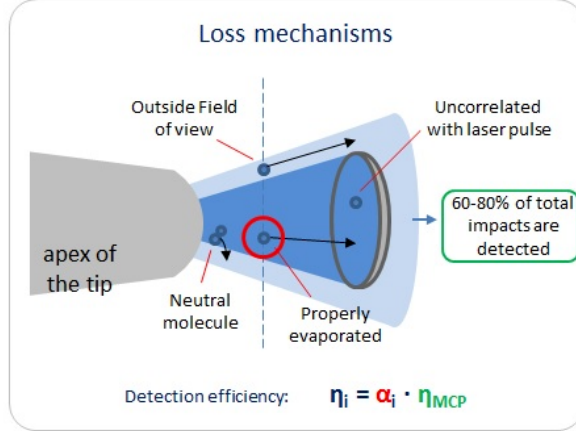


Figure 1.9: Schematic representation of the ions loss mechanisms. Only 60-80 % of the ions evaporated within the field of view are actually detected.

by the edges of the micro-channels and which does not lead to the generation of a detectable electric signal. This geometrical constraint fixes the ideal APT detection efficiency at $\eta_{MCP} \approx [60; 80]\%$. The actual detection efficiency, entering equation (1.20), is lower, the difference being mainly ascribable to the ions which are not evaporated simultaneously with the arrival of the voltage/laser pulse and for which the identification of the chemical nature is not possible (not indexed in the mass spectrum). The total detection efficiency η thus should account for both effects. Other mechanisms leading to the loss of atoms have been proposed for explaining experimental results obtained on semiconductor systems, such as the field evaporation of neutral molecules [49, 50] (which are thus not accelerated towards the detector, see section 1.2.7) or their formation as the product of dissociation processes [51] (which are either not detected or detected with random TOFs). It should be noted that the probability for an atom of being evaporated in-between pulses or as a part of a neutral molecule depends on its chemical nature. It follows that a better description of the detection process is given by a specific detection efficiency, as in the equation (1.23):

$$\eta_i = a_i \cdot \eta_{MCP} \quad (1.23)$$

where a_i defines the fraction of atoms of species i which are field-evaporated as ions during the voltage/laser pulse. The effects of different detection efficiencies on the measurements of composition performed by APT, along with a more detailed discussion of loss mechanisms and quantification of η can be found in the next subsection 1.2.7.

1.2.7 Compositional measurements and related issues in APT

While the composition of a given specimen can be determined by counting the events in the mass/charge histogram, various artifacts and aberrations may affect APT analysis. They originate from various sources (detection issues, presence of interfaces, clusters, layers with different evaporation field F_{ev} in the material, reconstruction algorithms). All these artifacts have important consequence on both compositional measurements and 3D reconstructions.

1.2.7.1 Mass spectra indexation

In order to determine the measured composition it is necessary to identify each peak in the mass spectrum. In presence of molecular ions this can be quite complex, but a correct and unambiguous interpretation of the mass spectrum is very often possible. However, two particular cases lead to an incorrect interpretation of the mass spectrum:

1. if we call an element A and m its atomic mass, then it is impossible to distinguish the detection of the A^{n+} from the A_2^{2n+} , since the mass to charge ratio is the same one; n is an integer index.
2. if we consider two species with the same *mass/charge* ratio, it is not possible to associate specifically to each peak the exact nature, but only the probability to be associated to one of the species: *e.g.* $\%_{(A)}$, for the first one, and *e.g.* $\%_{(B)}$, for the second one.

In summary, in the case (1) to know the chemical specie, of the detected atoms, is possible, but not their exact number. In the case (2) to know the exact number of ions to associate to each peak is possible, but not their chemical nature.

1.2.7.2 Preferential evaporation

Compound semiconductors are formed by two or more atomic species (*e.g.* ZnO and MgO). For a binary semiconductor AB, A and B atomic species have specific evaporation fields F_{ev}^A and F_{ev}^B . If the difference between these evaporation fields is large enough, the atomic species with lower F_{ev} can partly field evaporate in significant quantities between laser pulses. For example, if $F_{ev}^A < F_{ev}^B$, the atoms of the specie A have a high probability to leave the tip between laser pulses, see equations (1.2) and (1.7). This phenomenon is called “preferential evaporation” and it is said that A atoms “preferentially evaporate” (compared to B atoms), and lower A content will be detected. Because TOF measurements start at the instant at which a laser pulse reach the tip, the TOF of preferentially evaporated A ions will be partly wrong. This will increase the background noise in mass spectra. A selective loss of A atoms will occur leading to a A content lower than expected.

1.2.7.3 Production of neutral molecules

During field evaporation, neutral atoms and molecules can be produced. Clearly, neutrals are not accelerated toward the detection systems because they are not charged particles. This mechanism leads to a selective loss of atoms. Such issue is thought to affect in particular nitrogen and oxygen, but also elements of V-VI-group, where the direct emission of neutral N_2 , O_2 molecules can take place. Neutrals are generated in low field conditions. If the DC electric field is increased enough to ionize such molecules, these can be detected. It is thus possible to reduce the quantity of neutrals, but this may increase the preferential evaporation of other species.

1.2.7.4 Multiple detection events

Multiple-ion events occur when two or more ions are detected for the same laser pulse. Depending on the materials, the analysis conditions and the tip geometry, multi-ion events may be numerous. This is observed, for example, closed to low index poles. The local electric field is known to drastically increase when the diameter of the terrace decreases. This leads to bursts containing a large number of ions [52]. Phases with

very different evaporation fields may also produce numerous multi-ion events. The preferential retention of high evaporation field species at the tip surface is then observed. Burst containing large numbers of high evaporation field ions can occur, generating multiple-ion events. An example is provided by G. Da Costa *et al.* [38], analyzing [100] oriented Si wafers where a very high dose of ^{11}B atoms were implanted ($10^{17} \text{ at} \cdot \text{cm}^{-2}$). Because the evaporation field of B ($64 \text{ V} \cdot \text{nm}^{-1}$) is higher than that of Si ($33 \text{ V} \cdot \text{nm}^{-1}$), B is prone to strong retention effects. Even when a low detection rate is used ($0.006 \text{ event/pulse}$), burst involving B ions are observed. The use of a conventional DLD detector leads to a selective loss of B atoms due to pronounced pile-up effects. Contrariwise, using an aDLD detector (section 1.2.5.1) up to 30 ions on the same evaporation pulse can be detected. The ability to detect multi-ion events is in fact fundamental in order to measure the correct composition.

1.2.7.5 Dissociation phenomena

Dissociation of molecular ions may occur during their flight. This reaction is schematized in figure 1.10, where a mother molecular ion m_p is dissociated in two daughter ions m_1 and m_2 . Clearly, both total mass and charge must be conserved during this process. Because daughter ions are typically charged particles, these are accelerated by the electric field and can be detected. However, the measured TOFs of daughter ions are different from these expected for the direct mechanism of evaporation. Dissociation processes can be revealed thanks to the so-called correlation histograms [53]. These histograms represent the $\{m_1, m_2\}$ ion couples detected in multiple-ion events. Multiple events with $n > 2$ were taken into account along with the possible permutations of ion pairs involved in these events: *e.g.* a triple event, where m_1 , m_2 and m_3 ions are involved and split in $\{m_1, m_2\}$, $\{m_2, m_3\}$ and $\{m_1, m_3\}$ ion pairs (multiple-ion events with $n > 2$ are very few). The ion-pair order is not considered and the histogram is computed by imposing a diagonal symmetry. Ions can leave the tip exactly in coincidence with laser pulses, leading to the detection of multiple events in which ions exhibits the expected mass-to-charge ratios.

A simple model of molecular ion dissociation is proposed in ref. [53]. A molecular parent

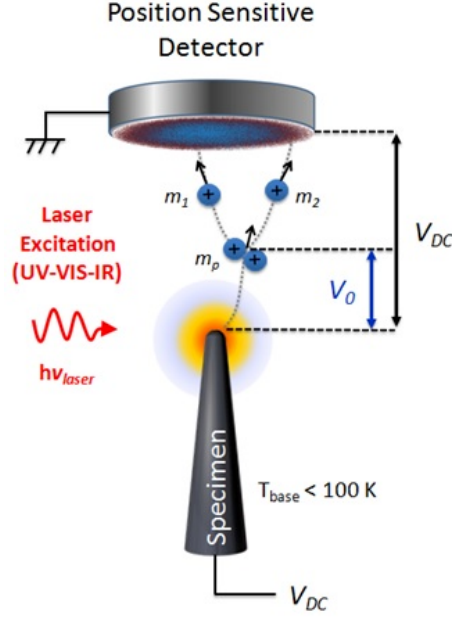


Figure 1.10: Schematic representation of the dissociation of a molecular ion into two daughter ions during its fly toward the detector.

ion with mass-to-charge ratio m_p is accelerated toward the detector and before reaching this is dissociated in two charged fragments with mass-to-charge ratios m_1 and m_2 . This reaction can be schematized as following: $m_p \longrightarrow m_1 + m_2$. However, the measured mass-to-charge ratio of daughter ions m'_1 and m'_2 are different from m_1 and m_2 if dissociation do not occur very close to the tip surface. The measured mass-to-charge ratios m'_i of daughter ions are provided by the equation 1.24:

$$m'_i = m_i \cdot \left[1 - \frac{V_0}{V_{DC}} \cdot \left(1 - \frac{m_i}{m_p} \right) \right]^{-3} \quad (1.24)$$

where V_{DC} is the DC voltage applied to the tip and V_0 the potential drop after which dissociation occurs. If $V_0 \ll V_{DC}$ the detected mass-to-charge ratios m'_i tends towards m_i .

1.2.8 Charge State Ratio metrics

In this thesis, we adopted the so-called Me^{2+}/Me^{1+} Charge State Ratio (CSR) metrics, which was enunciated for metallic elements, but it can be considered valid also for semiconductors. The main points which make advantageous to use the CSR metrics are the following:

- (i) The Me^{2+}/Me^{1+} CSR is related to the surface field. This relationship might be made quantitative through Kingham's post-ionization model [54]. In principle, the phenomenon of post-ionization takes place at a distance of several Å from the sample surface, and should be nearly independent of the material in which the atom was found if the evaporation takes place in the singly charged state. The charge state abundances of the evaporated ions are thus a function of the surface field. By inverting this function, it becomes possible to calculate an effective surface field F_{eff} . However, this effective field F_{eff} should only be considered as an estimate of the actual surface field F_S introduced in eq.(1.1) [55, 56].
- (ii) The Me^{2+}/Me^{1+} CSR can be defined as a local quantity, as it can be calculated within arbitrarily chosen 3D volumes. This is useful in order to map the local surface field and correlate it with the locally measured composition.
- (iii) The Me^{2+}/Me^{1+} CSR allows for studying the composition trends even in the case where the tip shape significantly changes during the APT analysis.

1.3 La-APT/ μ PL coupled “*in-situ*”

In the first two sections (1.1 and 1.2) we have described separately the working principle of two independent techniques: the μ PL and the (La-)APT systems. In this thesis the La-APT and μ PL spectroscopy were combined “*in-situ*”, within the same instrument. The combination of these two techniques was made with the aim to use an original multi-microscopy approach, which allows to better correlate and understand the physics involved in field-evaporation process and the emissive properties of the nanomaterials probed under a high electric field (≥ 10 V/nm). The advantage of this new machine is

to use the same laser excitation for both evaporating a tip specimen and for inducing the emission (μ PL emission) which can be detected while the sample is evaporating, as it is shown in figure 1.11. This process allows to strictly correlate the variation of the

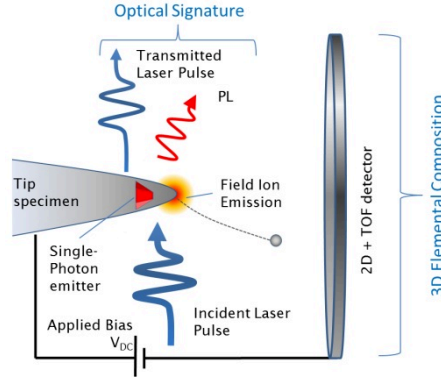


Figure 1.11: The core of the project: the combination between La-APT and the μ PL systems used to probe the sample under high electric field.

photoluminescence signal with nano-metric scale volumes of the tip evaporated during APT. Thanks to the development of a specially designed tomographic atom probe, it is shown that μ -PL can be successfully performed on a single atom probe tip during La-APT. In principle, the emission of single quantum light emitters (*e.g.* single QW or QD) or optically active defects can be revealed. This method can be extended to a wide range of bandgap materials, opening new perspectives for correlative studies of single atom probe tips. In this thesis, the “*in-situ*” configuration of the system setup was used in two different ways, in order to study two different materials: single-crystal diamond nanoneedles containing color centers and $ZnO/Mg_xZn_{1-x}O$ MQW heterostructure specimens. These two different methods will be described more in details in Chapter 3 and Chapter 5, respectively, below, the general working principle of the coupled system setup is introduced.

1.3.1 Experimental setup

A schematic representation of the combining μ -PL and La-APT is shown in figure 1.12. In a conventional La-APT machine the tip is illuminated by laser pulses which trigger

the emission of ions (figure 1.4 (b)).

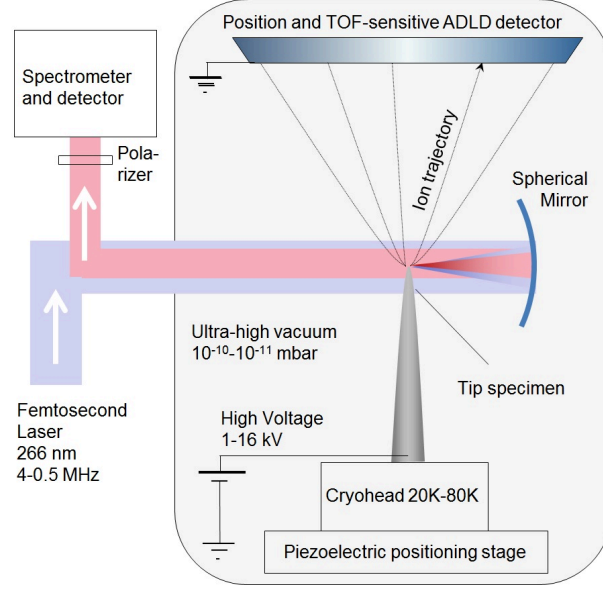


Figure 1.12: Schematic of the experimental setup: the coupled La-APT/ μ PL “*in-situ*”.

The absorption of laser pulses can generate μ PL emission from the tip. In a conventional APT instrument no optical elements are present in order to collect such signal. In this system a spherical mirror is introduced inside the analysis chamber, following the design proposed by Rigutti et al. [57]. The focal point of the mirror is in correspondence of the tip. Such configuration allows collecting the μ PL emission and focusing it outside the atom probe analysis chamber, where: a spectrometer, with a spectral resolution of 0.06 nm , and/or a streak camera, used to measure the variation in time of the μ PL intensity, can be placed. In the specific: the instrument is equipped with a tunable Ti:Sa laser which emits at 780 nm . A Third Harmonic Generator ‘THG’ (or Second Harmonic Generator ‘SHG’) is employed to select a wavelength of 260 nm (or 390 nm). The laser repetition frequency can be ranged between 400 kHz and 4 MHz . The laser is focused on atom probe tips with a spot size of around $1 \mu\text{m}$. The incident power can be varied between $15 \mu\text{W}$ to around $2000 \mu\text{W}$. A standard MCP/DLD detector is placed in front of the tip at a distance of $L = 17 \text{ cm}$. Such detection system is able to perform

analysis using laser repetition frequency up to 1.7 MHz . This characteristic drastically reduces the time required to perform La-APT compared to commercial tomographic atom probe, where the laser repetition frequency is 50 or 100 kHz . Anyway, as mentioned in section 1.2.5.1, the detection system currently in use does not support the detection of multiple-ion events due to difficulties related to the high acquisition frequencies. The exclusion of multiple-ion events has a major impact on the compositional measurements. In fact, in the semiconductor materials multiple-ion events are typically about the $5 \div 20\%$ of the total number of detected events. The accuracy of composition measurements of binary and ternary semiconductors measured by La-APT, or the coupled μPL /La-APT system, was demonstrated by E. di Russo *et al.* [58] to depend mainly on the range of the surface electric field. In the article [58], the investigation of the chemical composition of III-V and II-VI ternary alloys ($A_xB_{1-x}C$) gives a correct value of the site fraction (x) at ‘low’ field conditions, while at ‘high’ field conditions a preferential evaporation of mellic species was detected.

“*In-situ*” analyses with the coupled system were performed on $\text{ZnO}/\text{Mg}_x\text{Zn}_{1-x}\text{O}$ MQWs systems and the experimental protocol followed in order to perform the correlative analyses are reported in the section 5.2.1, Chapter 5. While, in the study of diamond nanoneedles with color centers, the APT-detector is not used as a nanoanalysis tool, but rather as position sensor for the laser spot, as it will be explained in the section 3.1, Chapter 3.

1.4 FIB/SEM specimens preparation

The potential of the developed multi-microscopy approach relies on the possibility of performing APT and μPL analysis on the same specimen. While the optical spectroscopy analysis has no particular requirements for what concern the geometry of the tip, APT and electron microscopy require the samples to be prepared under the form of field emission tips. Therefore, the μPL signals have to be acquired from specimens whose optically active region is contained within the typical volumes of a field emission tip apex (radius of $\sim 50\text{ nm}$ and depth of few hundreds of nm), as explained in section 1.3. The detection of the emitted PL signal could in principle be not an easy

task: let alone the difficulty which stems from the small volume of the emitting region (which in principle can be coped with using a sensible enough detection system), the main problem consists in the way in which specimens for APT and SEM analyses are prepared.

In order to obtain the needed small apex radii, the heterostructure samples of $ZnO/MgZnO$ were prepared through Focused Ion Beam ‘FIB’ annular milling [59], for which high energetic Ga ions are accelerated on the specimen surface following specific patterns (ring-shaped patterns, from which the name of the technique is derived), removing matter from the sample volume and sharpening it. The impinging ions can strongly modify the properties of the surface and implant below the specimen surface at depths which depend on their energy (or ion emission current) and consequently damaging the optical properties of the system, creating non radiative recombination centers for the generated charge carriers [60].

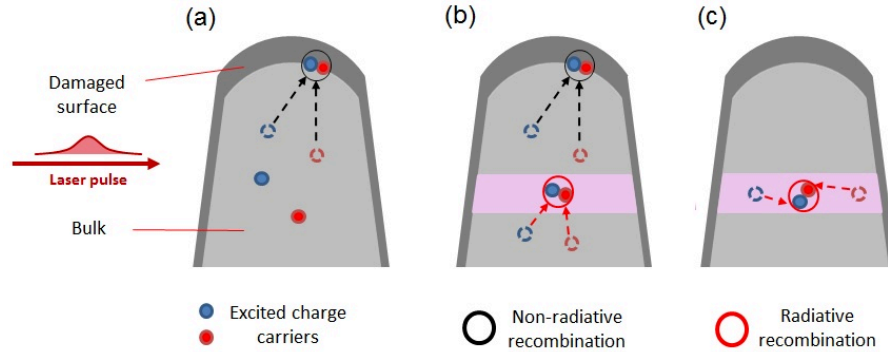


Figure 1.13: Non-radiative and radiative recombination process in annular milled field emission tips. (a) In single phase systems charge carriers generated in the bulk can travel to the surface and recombine within non-radiative recombination centers. In heterostructures, charge carriers can be generated in the bulk (b) or directly within the heterostructures (c) and then recombine radiatively within the heterostructures and far from the surface.

Notwithstanding the ion damage caused by the sample preparation procedures, a good μ PL signal could be obtained for all analyzed systems. While this result can be partially ascribed to the caution exercised during the last milling steps (deposition

of a protective capping over the milled surface and milling performed at $[1; 10] \text{ pA}$ at 30 kV and 50 pA at 2 kV with an angle of incidence of around 4°), the success of the analysis relies on the confining properties of the nanostructured systems analyzed, as schematized in figure 1.13: in specimens characterized by a single phase (a), charge carriers generated in the bulk can travel to the surface and recombine within non-radiative recombination centers. In low dimensional semiconductors, depending on the nature of the system and of the excitation energy (photon energy with respect to electron and hole ground states energy difference), charge carriers can be generated in the bulk (b), or directly within the heterostructures (c), and then recombine radiatively, within the heterostructures, and far from the surface (as their diffusion length is diminished by the quantum confinement provided by the heterostructures). The ZnO/MgZnO MQWs specimens were prepared using the SEM-FIB NVISION40 (Zeiss) microscope. The samples were prepared using the lift-out [61] and annular milling methods. On the surface of the specimen a trench of $\sim 20 \mu\text{m}$ length and $\sim 2 \mu\text{m}$ width is milled by FIB and separated from the rest of the specimen by means of a micromanipulator. Sections of this trench are cut and soldered on tungsten support tips by FIB deposition of Pt . Finally, the needle-like shape for the soldered sections required for the multi-microscopy analysis is obtained by FIB annular milling.

Differently from the ZnO/MgZnO specimens, diamond specimens, about which is reported in Chapter 2, section 2.5.1, are deposited on a Si substrate (001), and they have pyramidal needle shape. The diamond tips deposited above this substrate have different sizes, varying in the range from few microns to hundreds of microns, and their radius of curvature can be found in the range from few nm up to few microns. So, not all diamond needles are good candidates to be inserted into the APT chamber. In order to determine which diamond tips are good to analyse, optical microscope is used to observe them and the good candidates are fished and glued on a tungsten tip which serves as a support for the APT specimen. Diamond needles can be glued on the tungsten tip following two different ways:

- by micromanipulation under optical microscope, where individual needles are extracted from the powdered Si substrate and glued on tungsten support tips. The micromanipulation consists to dip the apex of the tungsten inside a silver con-

ductive epoxy glues and then to use the glue in order to pick up a diamond tip, from the Si substrate, where the diamond specimens are deposited.

- by micromanipulation within a SEM-FIB system. The diamond tips, deposited on Si substrate are observed by SEM microscope. A diamond tip with suitable size of apex radius is selected and it is soldered on the apex of a micromanipulator, by FIB *Pt* deposition. The diamond tip is extracted from the powdered Si substrate by means of the micromanipulator, figure 1.14(a) and soldered on a tungsten support tip, by FIB *Pt* deposition, figure 1.14(a). Finally, the micromanipulator is pulled away from the diamond tip with a rapid movement. This last step can result in the loss of the diamond specimen.

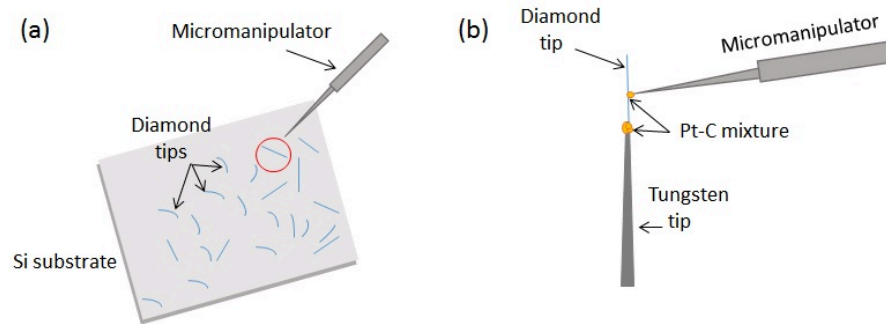


Figure 1.14: Schematic of diamond specimen preparation, using the SEM-FIB NVI-SION40 (Zeiss) microscope, by SEM point of view. In (a), the micromanipulator is approaching the selected diamond tip. In (b) the diamond tip is glued with a *Pt – C* mixture to the micromanipulator and to the tungsten support-tip.

We can summarize the advantages and disadvantages related to these two methods, as follows.

The preparation of diamond specimens by micromanipulation has:

- **the advantage** of allowing for an easier manipulation of the diamond tips, since the optical microscope is an instrument less complicated than the SEM-FIB system.
- **the disadvantage** that the apex radius can not be assessed.

The preparation of diamond specimens by SEM-FIB has:

- **the advantage** to give direct access to the sizes of the diamond needles during the assembly of specimens.
- **the disadvantage** that Ga^+ ions beam can damage the diamond tip, if directly focused on it. Furthermore, the last step, when the micromanipulator is pulled away from the diamond specimen, has low chances of success.

In conclusion, the preparation of diamond specimens results easier using the optical microscope. Then diamond specimen is observed by SEM or TEM, which have higher spatial resolution than the optical microscope, giving access to the nm scale. The diamond specimen preparation through the SEM-FIB method is really time-consuming. Therefore, I chose to prepare the diamond specimens by micromanipulation under optical microscope and to measure the geometry of the diamond specimens, by SEM, in a second step.

Chapter 2

Overview about diamond

2.1 Physical properties of diamond

Diamond is an allotrope form of carbon which is attractive for its luster, extreme hardness and high thermal conductivity. In order to understand from where these peculiar characteristics of diamond come from, a clear picture of the atomic configuration of the carbon atom and the way how it is bonded to other carbon atoms into the diamond lattice is needed. A single carbon atom has six electrons disposed into the electronic configuration $1s^2 2s^2 2p^2$. The two electrons in the 1s orbital are in the K shell (inner atomic shell), while the four electrons in the 2s and 2p orbitals are in the L shell (outer atomic shell). The carbon atom, as any element of the periodic system that belongs to the group IV, has four electrons in the outer shell. The more energetically advantageous configuration that it can have when it is bonded to other four carbon atoms occurs with the mechanism of the sp^3 hybridization, where the orbitals are directed along the tetrahedral directions. The $1s^2 2s^2 2p^2$ configuration does not give rise to the tetrahedral symmetry, because in the tetrahedral configuration, for each carbon atom there are four possible electronic shells that form directional bonds in four spatial directions, each shell involving an electron pair which has equal strength as the others. This situation occurs if we consider hybrid atomic orbitals as a rearrangement of the electrons in the L shell, with the promotion of one electron from the 2s orbital to the

2p orbital. The new orbitals due to the combination of the 2s and 2p orbitals are called hybrids and are depicted in figure 2.1

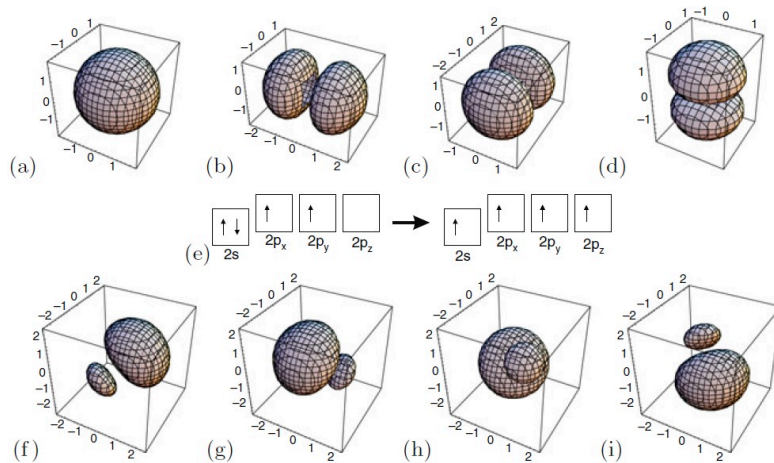


Figure 2.1: (a) the s orbital; in (b,c,d) the p_x , p_y , p_z orbitals; (e) the hybridization process (f,g,h,i) orbitals of the sp^3 hybridization [62]

In the sp^3 hybridization the 2s and the $2p_x$, $2p_y$, $2p_z$ orbitals blend in one single energy level and the resulting charge density is arranged in a regular tetrahedron, with elongated lobes each one forming an angle of 109.5° with each other, as reported in figure 2.2. As already said, the hybridization accounts for the tetrahedral symmetry, where the tetragonal carbon atoms are connected each one with other four carbon atoms sharing electrons in sp^3 hybrid orbitals. The resulting structure is a 3D lattice with tetrahedron structure.

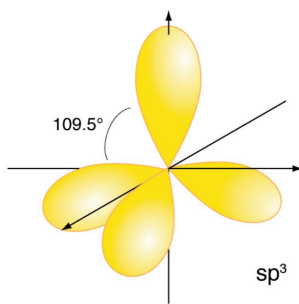


Figure 2.2: Charge density of sp^3 hybrid orbitals

2.2 Crystal Structure

2.2.1 Direct Lattice

Diamond has two crystalline structures, one with cubic symmetry (the more common and stable in nature) and the second one with a hexagonal symmetry (as the wurtzite structure with two identical atoms at the base). The most common diamond structure has the face centered cubic (*fcc*) lattice and the base consist of two atoms located at $(0, 0, 0)$ and $(\frac{1}{4}, \frac{1}{4}, \frac{1}{4})a_0$, where a_0 parameter is the constant of lattice. The *fcc* structure implies that the stacking order along the $\langle 111 \rangle$ direction is ABCABC and, in the $\langle 111 \rangle$ plane of the lattice, the distance between the lattice points, at room temperature and pressure, is $a = \frac{a_0}{\sqrt{2}}$, where $a_0 = 0.36683nm$ is the lattice constant [62]. The bonded atoms have a short length ($0.154nm$) and high bond energy ($711 kJ/mol$). The packing density of the carbon atoms that compose the diamond structure is about 0.34 [62].

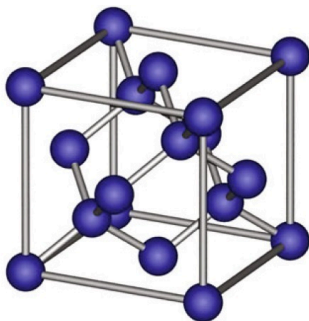


Figure 2.3: Unit cell of the diamond structure. The tetragonal bonds are indicated [62].

In (figure 2.3) the unit cell, that corresponds to the cubic symmetry is reported. It has an inversion center, located between two atoms of the base, *e.g.* at $(1/8, 1/8, 1/8)a$. The symmetry along the $\langle 111 \rangle$ direction is C_{3v} , as in the case of the zincblend structure, a rotation of $\frac{2\pi}{3}$ (C_3), around vertical axis.

2.3 Band Structure

Diamond is classified as an insulating material and it has a valence band with a set of three degenerate bands at the Γ point, as common to all group IV semiconductors. The electronic band structure shown in figure 2.4 is calculated from first-principles linear combination of atomic orbitals (LCAO) [63]. As we can observe in the figure 2.4, the minimum of the conduction band is set along the Δ direction, while the maximum of the valence band is aligned along the Γ direction, so diamond is classified as an indirect bandgap material. The energy bandgap $E_{gap} = 5.91 \text{ eV}$ was evaluated at cryogenic temperatures ($T \approx 0 - 20 \text{ K}$) and it corresponds to the energy difference between the point $\Gamma_{25'}$ of the valence band and the point X_1 related to the conduction band [63]. In agreement with the temperature dependence plot reported by Clark *et al.* [64], the energy gap of diamond decreases at the increasing of the temperature, so at room temperature its $E_{gap} \approx 5.46 \text{ eV}$.

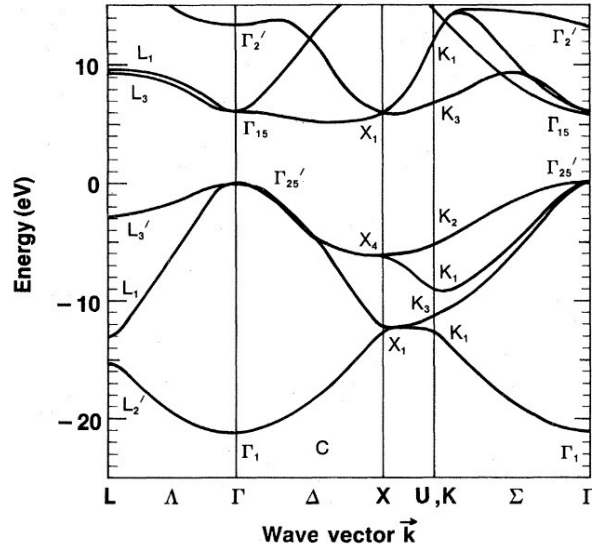


Figure 2.4: Band structure of diamond. The top of the valence band has been taken as the zero of energy. Several high-symmetry directions are indicated. The band structure shows that diamond is an indirect bandgap material, since the minimum of the conduction band and the maximum of the valence band are not aligned along the Γ direction [63].

2.4 Natural and Synthetic Diamond

Nowadays diamond can be classified into four different categories: natural, high-pressure synthetic, chemical vapor deposited and diamondlike carbon [65]. Natural diamond was formed around 3.3 billion years ago at high pressures and high temperatures more than 150km below the Earth surface in the area called mantle, which consists of volcanic magma. Natural diamond is the source of the expensive diamond gemstones, but in the last 100 years or so, the scarcity and the high cost of natural diamond have been challenged by the industrial production of synthetic diamond. In the 18th and 19th century several experiments were made in order to synthesize it, but for over one century were unsuccessful. It was not until 1955 that the first syntheses of diamond were achieved in: the USA (General Electric), Sweden (AESA) and Russia, ex-Soviet-Union, (Institute for high-pressure Physics). The advent of synthetic diamond and its rapid rise to industrial application have drastically changed the industrial market. Low-pressure diamond synthesis was discovered in the 1970's [65] and in 1980's a low-pressure vapor phase synthesis allowed to produce diamond in a coating form. This process is based on the method called chemical vapor phase deposition (CVD), that is a relatively inexpensive process and the material produced with this technique is called CVD diamond, vapor-phase diamond or diamond coating. In the CVD process a mixture of gas containing carbon are deposited at certain value of pressure and temperature on a substrate and after the removal of the template material, that serves as the substrate of the carbon deposition, a free-standing shape of diamond coating preserves its own integrity, normally in a polycrystalline form, as natural single-crystal diamond or high-pressure synthetic diamond. The diamond sample that I studied during my thesis were synthesized through the *Plasma Enhanced CVD* technique, a method of synthesis that will be explained better in the paragraph 2.5. Diamondlike carbon (DLC) is a class of amorphous carbon material that displays some of the typical properties of diamond (*e.g.* hardness, wear resistance and slickness [66, 67]). This kind of material is usually applied as a coating to other materials that could benefit from some of those properties. In order to understand the reasons of the development and applications for the diamond materials in competition with other materials it is necessary to go more in depth on its

crystal structure.

2.4.1 Mechanical properties

The mechanical properties of diamond can be distinguished in two main categories: the elastic and anelastic properties. Young's modulus, bulk modulus, shear modulus and Poisson's ratio are considered elastic or linear properties, since they are defined as the linear coefficients that come out from the relationships between stress and strain or other geometrical parameters of the material. These quantities can be summarized in a general way for single-crystal diamond and CVD diamond in the table 2.1.

Mechanical Property	Single-crystal diamond	CVD diamond
Bulk modulus (K)	433 <i>GPa</i>	443 <i>GPa</i>
Shear modulus (G)	502 <i>GPa</i>	507 <i>GPa</i>
Young's modulus (E), anisotropy (random) crystallites	[1050;1210] <i>GPa</i> 1143 <i>GPa</i>	\sim [500;1200] <i>GPa</i>
Poisson's ratio (ν), anisotropy (random) crystallites	[0.00786;0.115] 0.0691	0.075

Table 2.1: Some linear mechanical properties of single-crystal diamond and CVD diamond [68]

The Young's modulus defines the relationship between stress and strain of Hooke's law in a material, in the elastic regime of a uniaxial deformation. In the particular case of this thesis, the effect of an uniaxial stress along the $\langle 001 \rangle$ crystalline direction of single-crystal diamond nanoneedle is studied. In such case, the Young's modulus is defined as the linear coefficient of the stress and strain relationship of Hooke's law (2.1).

$$\sigma_3 = E \cdot \epsilon_3 \quad (2.1)$$

In the equation (2.1), the stress and strain are not given as matrix, but as the components of the stress (σ_3) and strain (ϵ_3) which act along the $\langle 001 \rangle$ direction.

The bulk modulus can be seen as the resistance of volume to change under an hydrostatic pressure, the shear modulus describes the material's reponse to a shear stress and the Poisson's ratio is the response in the directions orthogonal to an uniaxial stress. These elastic moduli are not independent and they can be connected for isotropic materials through the equations (2.2) and (2.3):

$$E = 2G(1 + \nu) \quad (2.2)$$

$$E = 3K(1 + 2\nu) \quad (2.3)$$

	Hardness (<i>GPa</i>)	Fracture toughness (<i>MPa · m^½</i>)	Fracture strength (<i>GPa</i>)
Ideal crystal	~110	...	~93
Single-crystal diamond	50-110	6-18	<1
Microcrystalline	118	13	7.1
Nanocrystalline	86	...	3.8

Table 2.2: Highest values reported for diamond non-linear mechanical properties [68].

Despite its brittle nature, diamond is known for its extreme hardness, which along with the fracture toughness and the fracture strength are non linear properties of diamond [68]. The hardness “*H*”, which is the ability of a material to resist deformation,[68], is normally connected with plastic deformation of the material, under an applied external force, and as the Young's modulus, it is a quantity that can be extracted from the stress-strain curve, for example during tensile stress tests. The fracture toughness describes the ability of a material containing a crack to resist fracture. The fracture strength is the ability of a material to resist failure and is designated specifically according to the mode of applied loading, such as tensile, compressive or bending.

In the table 2.2 the highest values measured for these anelastic properties of diamond are summarized as a function of the size and shape of diamond sample considered.

2.4.2 Defects in Diamond

Synthetic or natural diamond is never free of defects and impurities: this means that some carbon atoms, which compose the diamond lattice, do not occupy the lattice sites or can be substituted by other elements. These deviations can be due to some missing carbon atoms on the corresponding atomic site, named vacancies, or to the replacement of one carbon atom with an atom of different atomic number Z , called impurity. They can also be carbon atoms that are shifted from their atomic site and in this case the defect is called self-interstitial, but, again, if the interstitial is an atom with different atomic number Z with respect to the carbon atom, then they are called interstitial impurities. So, in general with the word “impurity” is designated the presence of atoms of different chemical specie inside of the crystal structure. These deviations are always accompanied by a relaxation of the surroundings host atoms. The lattice relaxation depends on the charge state of the defect and on the atomic radius of the kind of defect (*e.g.* a vacancy, a tetrahedral interstitial or an impurity) the symmetry of the system can be reduced, *e.g.* from tetragonal to trigonal, and therefore causes degenerate electronic levels to split. Such splitting is called the Jahn-Teller effect and it will be discussed more in detail in the section 2.5.2. Crystal defects and impurities modify the band picture of the absorption spectra of diamond by forming further discrete energy levels within the forbidden energy gap. Thus a comparison of the optical properties of the natural and synthetic classes of diamond can give valuable information concerning the diamond structure itself. Robertson, Fox and Martin, in 1934-1936 [69], suggested a way to classify diamond, based on the nature and amounts of impurities contained within the structure and they established two main groups of diamond: *type I* and *type II*. In order to detect the amounts and kind of impurities a wide range of experiments were performed and among them, nowadays the most common method is the **F**ourier-**T**ransform **i**nfrared spectroscopy (**FTIR**) [69]. This kind of analysis consists in sending a beam of IR radiation through a diamond sample and then from the absorption spectra recognizing the nature and the amount of the impurities that are bonded to the carbon atoms. Thanks to this method it was found that type I diamonds contain a sufficient number of nitrogen atoms to be detected, which is not the case for type II diamond

[69, 70]. These two groups are subdivided as a function of the nature of the impurities involved. Type I is subdivided in: type Ia which contains nitrogen atoms that replace the atomic carbon atoms in the lattice site or in interstitial positions. In type Ib nitrogen has replaced a carbon atom into the lattice site, but nitrogen atoms are isolated from each other, in literature they are called with several names: isolated nitrogen [71], substitutional nitrogen [72] and nitrogen centers [73]. Type II is subdivided in type IIa that contains no easily detectable nitrogen or boron impurities and type IIb that contains as well no-IR-measurable nitrogen impurities, but this type of diamond can contain boron impurities that are thought to be isolated single atoms that replace the carbon into the diamond lattice. Nitrogen and boron, due to their small atomic radii, fit easily within the diamond structure and they are present in all natural and synthetic diamond, these two elements are the only impurities that can be introduced into the diamond lattice with any degree of control [70]. The interaction of the IR radiation with nitrogen and boron impurity arrangement into diamond lattice cause distinctive features in the IR region of the electromagnetic spectrum, in particular each kind of type-related nitrogen and boron impurity causes a specific and unique absorption band or bands. Nitrogen is present in all natural diamond, with up to 2000 ppm in type Ia diamond, while boron is present in natural IIb diamond (up to 100 ppm) and in some doped IIb synthetic diamond (270 ppm). Apart for these two elements no others were found in concentration higher than 100 ppm, in type Ia and IIb diamond [74]. The presence of impurities within the crystalline structure of diamond can contribute to change in a considerable way the standard properties of this material. In order to give a more accurate classification of the properties of diamond the type of impurity included into the crystalline structure has to be taken into account.

Related to the optical properties “pure” diamond has a large energy band gap (E_{gap}), that gives it the widest optical transparency band of all known solids, which ranges from 220 nm (fundamental absorption edge) to the far IR. only two minor phonon absorption bands between 2.5 μm and 7 μm perturb the diamond’s transparency in the IR region [70, 75]. The optical transparency of diamond can be perturbed also by the presence of some defects into the crystal structure, which cause the appearance of intragap levels inside of the large band gap, most of which give rise to luminescence in the visible

range and that is the reason why these defects are called color centers. Some of these defects are known from the pionereeing analysis of Robertson et al. [69] and since they show specific absorption bands these defects are labeled as A, B1 and B2 bands of the diamond [70, 75, 76]. Also nitrogen complexes are one of the most common and studied defects in diamond. Among these defects the N3 system is the responsible of the blue emission observed in the vibronic band of natural diamond and it consists of three nearest-neighbour nitrogen atoms on the $\langle 111 \rangle$ plane “bonded” to a common vacancy [75, 77]. Other well known systems are the N-V centers [77, 78], which consist of a nitrogen atom and a first-neighbor vacancy in the carbon lattice of diamond and they can exist in two main electronic states NV^0 and NV^- . In particular, a more detailed description of the optical properties of the NV^0 centers is given in the section 2.5.2 of this Chapter.

2.4.3 Thermal and electrical properties

Lattice impurity	Thermal	Electric	Impurity	
	Conductivity ($\frac{W}{m \cdot ^\circ C}$)	resistivity ($\Omega \cdot cm$)	Nitrogen (ppm)	Others (ppm)
Ia	800	10^4 - 10^{16}	≈ 2000	...
Ib	800-1700	10^4 - 10^{16}	10^2 - 10^3	10^4 - 10^5
Ib	2000	10^{16}	1-100	...
IIa	2000	10^{16}	≈ 1	...
IIb	...	10 - 10^4	≈ 1	≈ 1000

Table 2.3: Thermal and electrical properties of different types of diamond

In the table 2.3 the main thermal and electrical properties of diamond are reported and, as discussed above, the value of these properties change drastically as a function of the type of diamond considered.

In this thesis we will focus mainly on the relation between the optical and mechanical properties of **PECVD** single-crystal diamond nanoneedles.

2.5 Description of the synthetic diamond needles

The high value of hardness (table 2.2) of single-crystal diamond hampers significantly a morphology modification of this crystal. This is the reason why, in order to get diamond samples as needle shape and an apex radius ' $R \leq 100\text{ nm}$ ' to analyze in the APT chamber (described in Chapter 1) it is important to use a technique of synthesis that allows to grow them already with the good size and shape as single crystal diamond nanoneedles. Micrometer scale single crystal diamond pyramidal needles were synthesized through PECVD technique by collaborators from the Department of Physics, at Moscow State University, in Moscow, Russia [79, 80] and in the next paragraph a more detailed description about the CVD process followed to grow the samples and the way how their characteristics were selected will be explained.

2.5.1 Synthesis procedure

Diamond growth using chemical vapor deposition is a *non-equilibrium* process, where the shapes of CVD diamond crystallites depend significantly on the kinetic parameters during the growth process. The CVD process consists in diamond or carbon deposition on a substrate of polished silicon 'Si' (001) wafers, with a thickness of $\sim 460\text{ }\mu\text{m}$ and $25 \times 25\text{ mm}^2$ size. Carbon condensation, from a hydrogen-methane gas mixture, is activated by a direct current (DC) discharge. The growth parameters that provide a stable DC discharge plasma and formation of the polycrystalline (001) textured diamond films were studied and found empirically to be [79]:

- the substrate temperature: $T = 900^\circ\text{C}$;
- the total gas pressure: $p = 9.5\text{ kPa}$;
- the gas mixture composition: $\text{CH}_4 : \text{H}_2 = 5 : 95$;
- the discharge voltage: $V_{DC} = 700\text{ V}$;
- the discharge current density: $j \sim 1\text{ A/cm}^2$

All these parameters contribute to determine the crystallographic orientation of the diamond crystallites in the grown film, quantified by the ratio of their growth rates along the different crystallographic directions. In particular, the ratio of the growth rates along the $\langle 001 \rangle$ and $\langle 111 \rangle$ crystallographic directions (V_{100} and V_{111} correspondingly), expressed by $\alpha = \sqrt{3} \frac{V_{100}}{V_{111}}$, is usually used to characterize the CVD process. The microneedles analyzed in this thesis are orientated along the $\langle 001 \rangle$ crystal direction and experimentally it was found that for the parameter α close to 1 the preferential growth of the diamond crystallites is along the $\langle 111 \rangle$ direction and the basic shape of the diamond crystallite is a cube, while for a value of α about 3 the fastest growth is along the $\langle 100 \rangle$ direction, changing the basic shape of the diamond crystallite to an octahedron. As a consequence, by varying the growth process parameters it is possible to change α [81].

A four stage model was suggested by [82] in order to explain the mechanism for the needle-shaped micro-diamond growth and oxidation.

1. The initial stage is the **ultrasonic treatment of the substrate with diamond powder** that produces seeds, which play a role in the formation of nucleation centers in the following CVD process.
2. Then the **condensation of carbon species** during CVD leads to the formation of diamond crystallites that have $\{100\}$ facets on their top and $\{111\}$ facets on their lateral surfaces. The formation of a crystalline diamond is accompanied by a hydrogen etching of its surface. The resulting diamond crystal shape depends on the balance between the material deposition and etching process.
3. Due to the higher etching rates, the surfaces corresponding to the $\{111\}$ facets contain a number of structure defects that provide sites for **secondary nucleation** on the $\{111\}$ facet. The secondary crystal growth during the CVD process takes place only on the $\{111\}$ facets, since the growth rate along the $\langle 100 \rangle$ direction is lower than along the $\langle 111 \rangle$ direction and this leads to a more ordered crystalline structure of the $\{100\}$ facets. The direct exposition of the $\{100\}$ facets of the initial nuclei get the specific structure of the polycrystalline film with the

micrometer sized pyramidal crystallites surrounded by the nano-sized diamond and disordered carbon phases.

4. The **oxidation process** for nano-diamond, graphitic phases and the smallest secondary nucleated microcrystalline diamonds is higher than for large diamond crystals and as result of this difference, small-size secondary crystallites are selectively removed. The oxidation process is performed at $T = 650^\circ C$, for $\sim 10h$, obtaining diamond microcrystallite with a perfect pyramidal shape terminated by $\{100\}$ basal facet (figure 2.5). The core diamond crystallites remain intact and not affected from the surrounding disordered material.

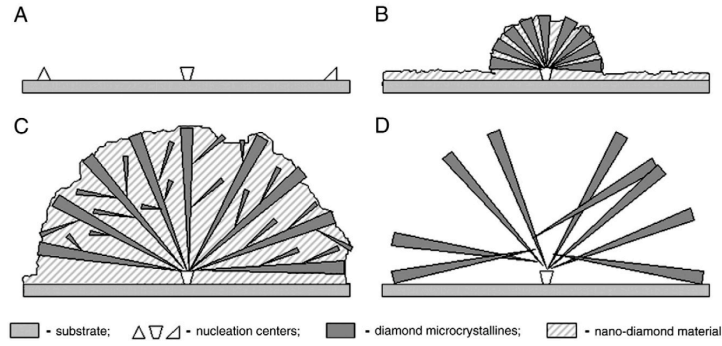


Figure 2.5: A schematic presentation of the formation for the bunch of the needle-like-micro-diamonds. (A), (B) and (C) are growth stages and (D) is a result of the thermal oxidation [82].

At the end of the CVD process, the diamond films synthesized were finally characterized by Raman spectroscopy [81], using as excitation source an argon-ion laser ($\lambda = 514.5nm$), where the presence of the narrow sharped line at $1330cm^{-1}$ confirmed that the film is composed by micro-sized diamond crystallites and eventually the weak wide band at $1580cm^{-1}$ represented a remaining amorphous carbon. The morphology peculiarities of the produced samples were examined by scanning electron microscopy (SEM) imaging [81] and by these observations, the growth team ascertained that the dimensions of the diamond pyramids are in the range of a few up to hundreds of micrometers, with the sharper apex radius of the pyramids varying in the range of $2nm$

to $20nm$. The diamond needles deposited above a silicon substrate have so the good size and shape with which they will be analyzed into the μ PL system.

The diamond pyramids microneedles are delivered, deposited on the Si substrate (001), where they were grown during the CVD process. The details about the preparation of diamond specimens is reported in section 1.4 of Chapter 1.

2.5.2 Diamond defects: focus on nitrogen vacancy centers

The single-crystal needle-like diamonds contain several luminescent defects due to the followed synthesis procedure. Among them the nitrogen-vacancy ‘NV’ and silicon-vacancy ‘SiV’ color centers are the most known and studied defects [83, 84, 85, 86, 87] and the concentration profile of these two kind of centers into the pyramidal diamond tips were performed from the russian collaborators through photoluminescence spectra, intensity mapping and fluorescence lifetime imaging microscopy [88]. These studies reveal that SiV centers are concentrated at the crystalline apex, while NV centers are distributed over the whole crystallite. The correspondingly concentrations of nitrogen and silicon related centers were evaluated to be around $0.24 \div 3.3 \times 10^{15} cm^{-3}$ and $2.5 \div 96 \times 10^{15} cm^{-3}$ into the whole diamond needle volume, as showed into figure 2.6.

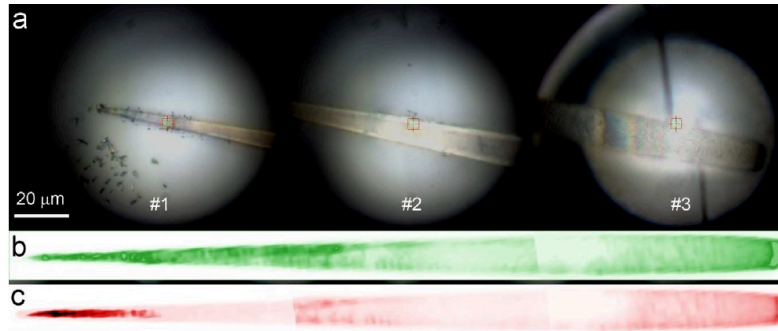


Figure 2.6: (a) Optical microscopy images of the diamond needle obtained (#1) near the apex, (#2) in the middle and (#3) close to the base of the tip. The PL emission mapping of the needle is obtained combining the light intensity distributions measured separately for the three area in the range (b) $[570; 580]nm$ and (c) $[730; 770]nm$ [89].

In this thesis, the NV^0 defect, which belongs to the family of the NV centers, was used as stress sensor in order to measure the stress induced onto the needle-like diamond sample by the applied electric field, during the piezo-spectroscopic analysis and in this section, the aim is to give the mainline about the structure and optical characteristics of these centers.

The nitrogen-vacancy ' NV ' centers emit in the visible range of wavelengths and for that reason they are included into the family of diamond defects known as color-centers. These defects consist of a substitutional nitrogen atom bond to a vacancy, oriented along the $\langle 111 \rangle$ crystalline direction of the diamond lattice, see figure 2.7, and they can have two stable charge-states: neutral NV^0 and negative NV^- , with photo-induced interconversion of these two states [90].

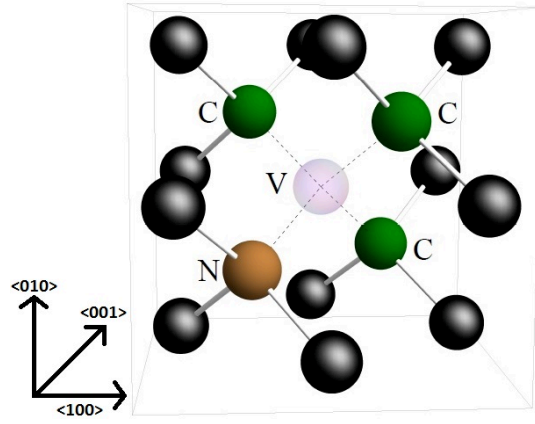


Figure 2.7: The NV center into the diamond lattice. In transparent is depicted the vacancy, in green the nearest neighbour carbon atoms to the vacancy, in brown the substitutional nitrogen atom and in black the next-to-nearest carbon neighbours to the vacancy [83]. At the bottom of the figure, on the left, the crystallographic system of referement.

Its electronic structure is built from three carbon dangling bond electrons and two electrons from the nitrogen lone pair orbital, which corresponds to a total of five electrons, for the neutral charge state, while for the negative charge state the sixth electron is captured from the lattice.

The first observations of the formation of the NV^- optical band in diamond *type Ib* was

made by du Preez in 1965 after radiation damage and annealing [91]. The hypothesis that the observed band was generated by a substitutional nitrogen-vacancy pair, came from the knowledge that *type Ib* diamond contains a significant concentration of single substitutional nitrogen (N_s) defects and the process of radiation damage and annealing creates mobile lattice vacancies. This hypothesis was supported also by experimental results, through which it was possible to associate to the center a trigonal symmetry C_{3v} along the $\langle 111 \rangle$ crystalline direction [3]. The optical band of the NV^0 defect was initially only observed in cathodoluminescence due to its weak photoabsorption signal and eventually observed in photoabsorption and photoluminescence by Davies [92]. Although Davies' studies were published in 1979, it was not until 1996, when Mita [93] observed correlated changes in the concentrations of NV^- and NV^0 under neutron irradiation, that it was proved that the center responsible of the NV^0 optical band was the neutral charge state of the NV^- center. Additional proofs to Mita's suggestion came by observations of photoconversion between the two charge states, which means that the NV center is able to switch from one charge state to the other. These two centers can be converted one to the other under different optical conditions: *e.g.* applying high laser intensity or varying the range of exciting wavelengths, but they can also be established independently [94, 95]. The transformation of one NV charge state into the other is called photochromic effect [96], since it changes the band gap between the two electronic states, which is converted into a color switching of the emitted radiation. The electronic transitions of the NV centers are embedded in the band gap of diamond, away from both the valence and conduction bands, that's the reason why these centers are known to be deep-level defects [97, 83]. The purely electronic transition, without involving phonons, associated to each center is called zero phonon line 'ZPL' and it corresponds to 2.156 eV (~ 575 nm) for the NV^0 center and 1.945 eV (~ 637 nm) for the NV^- center [93]. At room temperature, the ZPL transitions are assisted by the phonon-side-band which corresponds to diamond lattice vibrations and they are positioned at higher/lower position in energy, respectively in absorption/emission [95]. The sharp ZPLs and the well defined phonon-side-bands confirms that the electronic transitions occur between discrete levels that are "deep" within the diamond bandgap, such that the diamond valence and conduction band are not involved in the optical transi-

tion. Within ref. [90] it was found that the ground state of the NV^- defect is placed at $2.94eV$ with respect to the diamond valence band or at $2.6eV$ from the conduction band [90] and it is labeled 3A_2 level, while the excited state is located $1.946eV$ above the corresponding ground state and it is called 3E state [90]. The NV^0 optical band has associated a ground state level labeled 2E and an excited one, that is $2.156eV$ higher in energy, labeled 2A , as shown in figure 2.8. The experiments performed by Aslam *et al.* [90] demonstrated that the *dark-state* of NV^- center is the neutral charge state NV^0 . The *dark-state* of NV^- center is a non-flourescing state, that was obtained by Aslam *et al.* [90], exciting the NV^- defect with red-light, while the excitation with blue-light gives photo-induced ionization conversion of the NV^- center in the NV^0 .

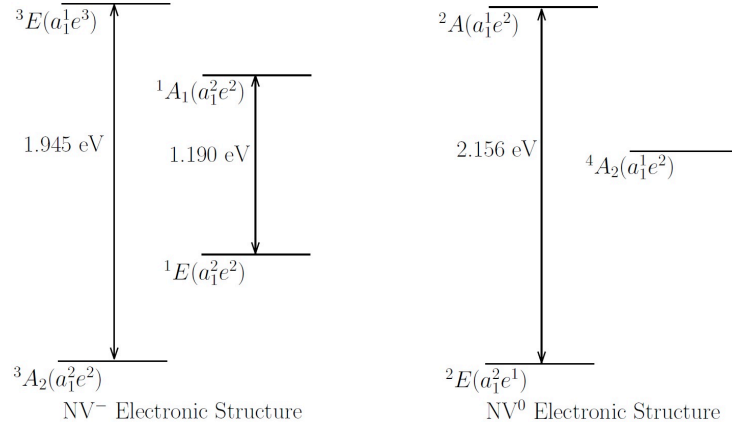


Figure 2.8: Schematics of the NV optical transitions. On the left, the electronic structure and ZPL transition of the NV^- are indicated, while on the right is depicted the electronic structure and ZPL transition related to the NV^0 center [90].

The optical transitions $A - E$ and $E - A$, respectively for the negatively and neutral NV center, are spin-conserving and they occur between the triplet ground and excited electronic states. Within ref. [98] the work directed by Reddy et collaborators reported for the first time the evidence of the spin triplet nature for the two NV centers. For what concerns the NV^- defect, electron paramagnetic resonance (EPR) measurements finally confirmed the triplet spin state, while for the NV^0 defect this confirmation came later due to the difficulty to detect the EPR signal related to this center [83]. It was found [97]

that the optical transition associated to the NV centers happens between the ground-state triplet and related excited-state triplet, while a non-radiative transition can occur between the excited-state triplet and an intermediate ground-state singlet of the NV centers. The spin-selective pathway decay between the two spin states, along with the long spin coherence times (up to $t = 1.8 \text{ ms}$) and well localized intraband electronic levels make them suitable as qubits for the realization of quantum devices [99]. The arrangement of the nitrogen impurity and a bonded vacancy into diamond crystal lattice produces a relaxation outward from the vacant site, followed by an electronic rearrangement into its surrounding and the characteristic NV intraband electronic energy-states. From PL studies related to the NV^0 center, Davies [100] concluded that the Jahn-Teller distortion on the NV^0 ground-state is $(0.14 \pm 0.07) \text{ eV}$, close to the value found later by a theoretical study reported by A. Gali of $\sim 0.09 \text{ eV}$, in agreement with the C_{3v} symmetry of the defect [101]. The Jahn-Teller effect consists to remove the degeneracy from the ground-state electronic level, which means to split one electronic state in two different levels, separated by $(0.14 \pm 0.07) \text{ eV}$.

The radiative lifetime of the NV^- center results around 13 ns and for the NV^0 center is around 20 ns in bulk diamond [102] and it is temperature independent. It was proved that in nanodiamond the radiative lifetime associated to these two centers is longer $\sim 25 \text{ ns}$ [99]. The change of the radiative lifetime as a function of the geometry of the sample therefore could be explained by the structural defects that appear into the diamond lattice, as instance cracks or grain boundaries due to different steps followed during the growth or synthesis of the material. The diamond needles, synthesized as reported in section 2.5.1, were probed by *fluorescence lifetime imaging spectroscopy* (FLIM) which revealed that the decay time of the NV centers depends on the position of the color centers along the tip [88]. In particular, it was found that, into the short time range scale of 25 ns , the decay time of these color centers increase by 2.1 ns near the apex of the tip and up to 8.9 ns towards the base of the pyramidal diamond tips. This behavior can be explained as a function of the structural defects inside the diamond needles which act as centers of non-radiative recombination.

SEM and TEM microscopy and Raman spectroscopy were used in order to get access to the crystal structure of the pyramidal diamond tips [103]. Through these techniques,

different regions of roughness and flatness were observed on the surface of the tips, as a function of the oxidation cycles that they received. Furthermore, by Raman spectroscopy it was found [103] that the diamond peak is present along the whole tip, in a continuous way, and other peculiar peaks related to graphitic carbon or specific crystallographic defects appear, in agreement with TEM measurements.

Relating to the photo-induced interconversion of the charge states between these two centers, known also as photochromic effect [96], several studies were carried out and it was found that the relative abundance of NV^- and NV^0 defects can depend on:

- impurities in the vicinity of the NV center [104];
- the optical illumination or exciting radiation, which can change the state of the NV^- into the NV^0 or viceversa, when they both coexist [105];
- the intense pulse excitation of single sites in nano-crystals, which can photo-ionize NV^- centers and generate stable NV^0 centers [106, 95].

In relation to the intensity and wavelength of excitation, also the range of time of excitation of these centers affects the conversion from one charge state to the other [95]. In the next Chapter we will focus on the optical properties of the NV^0 centers, while diamond specimens are immersed in high electric field ($\approx 10 V/nm$) and we will see how the optical properties of these color centers were used in order to study the mechanical properties of the diamond specimens, probed through a new experimental method of analysis.

Chapter 3

Photoluminescence-piezo-spectroscopy on diamond nanoneedles

In this chapter a new method to perform contactless piezo-spectroscopy of nanoscale systems by electrostatic field regulation is introduced. The analyses were performed within a laser tomographic atom probe ‘La-APT’ coupled *in-situ* with a microphotoluminescence ‘ μ PL’ bench, as described in the section 1.3, Chapter 1. By applying an intense electrostatic field and the laser radiation on diamond nanoneedles with color centers, it was possible to get access to their opto-mechanical properties. The study of the optical properties of these color centers allowed to:

1. measure the stress acting on the nanoscale diamond tips;
2. pave the way to an original optical contactless piezo-spectroscopy method for nanoscale systems under uniaxial tensile stress;
3. measure the electrostatic field at the apex of the nanometric diamond needles.

These three goals were reached by the study of the optical properties of NV^0 color centers present into diamond needles. Then the new method was used to study a diamond color center, whose nature is still not clear in literature [107].

3.1 Mechanism of induced stress on a diamond tip

The piezo-spectroscopic study of diamond needle crystals was performed into the coupled La-APT/ μ -PL setup, presented in Chapter 1. The application of the high electric field induces a large stress propagating inside the nanoneedle, indeed, often, during APT analysis, tips break. For conductive APT-samples, the relationship between the electric field applied to their surface (F_s) and the stress induced at their apex (σ_{apex}) is known to be (3.1):

$$\sigma_{apex} = \frac{1}{2}\epsilon_0 F_s^2 \quad (3.1)$$

The surface electric field (F_s) and the V_{DC} bias applied are proportional:

$$F_s = \frac{V_{DC}}{k_f R_{apex}} \quad (3.2)$$

where, the terms R_{apex} and k_f correspond respectively to the apex radius of the specimen and to a constant related to the needle shank angle and to the electrostatic environment of the needle. Therefore, the stress induced by the high electric field depends on the geometry of the probed tip. For non-conductive APT-samples, E. P. Silaeva *et al.* [16] proved that APT-specimens of dielectric materials (*e.g.* MgO), probed under a strong (1V/nm) static electric field within a La-APT system, are able to screen the electric field, confining its presence to their first atomic layers. This behavior is a consequence of the band-bending, induced by the high electric-field applied, that causes a significant cumulation of free carriers at their surface. The theoretical prediction of these phenomena was made in references [108, 109], in the case of low-resistivity semiconductors such as silicium, germanium and MgO tips, studied in ref.[16]. Following the results of E. P. Sileva *et al.* [16], eq.(3.2) and eq.(3.1) can be used also for non-conductive materials, such as diamond.

During the La-APT/ μ -PL analysis, the laser pulse was used in order to activate the electronic transitions of the optically active centers present into the APT-specimens. In particular, using the laser excitation energy into the UV range, $E_{exc} \sim 4.77 \text{ eV} < E_{gap} = 5.47 \text{ eV}$, a typical PL spectrum acquired from the diamond tip-specimens is shown in figure 3.1.

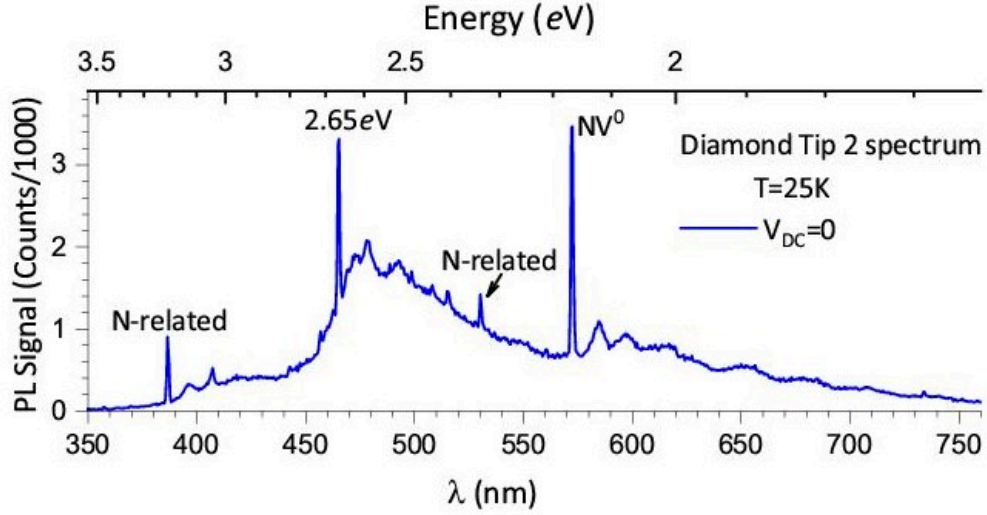


Figure 3.1: The PL signal of the diamond Tip 2, collected along the needle shank, around $3 \mu m$ from the apex, at $\lambda_{exc} = 260 nm$ and average $P_{exc} = 400 \mu W$. In the spectrum, different types of color centers can be identified, among them, the NV^0 center and the one with ZPL at $2.65 eV$, the focus of this study.

This spectrum was collected through a grating spectrometer with the highest spectral resolution of around $0.5 meV$, equipped with a nitrogen-cooled CCD camera.

The signal in fig.3.1 is obtained without applying any voltage on the specimen and focusing the laser beam at approximatively $\sim 3 \mu m$ from the apex. The laser beam waist, focused by a spherical mirror on the specimen, is about $1.5 \mu m$ and the position of the specimen is controlled by a closed feedback loop three-axial piezoelectric stage. In the spectrum in fig.3.1 is possible to recognize the emission of several color centers, with the zero phonon line ‘ZPL’ at given energy and associated phonon replicas. As outlined above, particular attention is dedicated to the NV^0 center, with the characteristic ZPL at $575 nm$ (or $2.156 eV$), and to the color center with ZPL at $468 nm$ (or $2.65 eV$). In the PL spectrum in figure 3.1 the signal related to the negatively charged NV^- center (ZPL at $\lambda = 637 nm$) is negligible or absent. That is due to the relatively poor concentration of this defect, detected at $\lambda_{exc} = 400 nm$, with intensity 10 times lower than the one obtained for the NV^0 defect [110]. Furthermore, the UV excitation wavelength can promote the photo-induced interconversion from the negative to the

neutral charge state of the NV centers [105]. The experimental procedure followed to acquire the spectra on diamond nanoneedles is described more in detail within the next section.

3.2 The NV⁰ defect as a stress-field sensor

If we zoom in on the NV⁰ peak, which appears into the spectra in figure 3.1 and we compare the spectra acquired at $V_{DC} = 0$ kV and at $V_{DC} = 16$ kV, the ZPL related to this center splits into two peaks, figure 3.2(a). As illustrated in figure 3.2(b), the ZPL at $V_{DC} = 0$ kV corresponds to the electronic transition between the excited state A_2 and the degenerate ground state E [90]. The V_{DC} bias acts as an external perturbation on the electronic ground state E , which splits into the E_X and E_Y levels and the $A_2 \rightarrow E_X$ and $A_2 \rightarrow E_Y$ electronic transitions correspond respectively to the PL emissions labeled as a and b , in agreement with the literature [84].

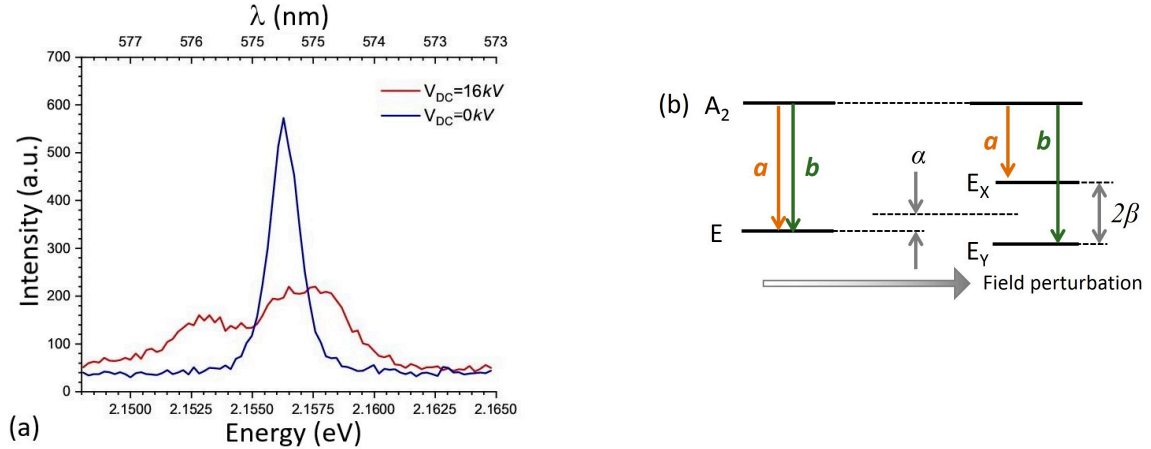


Figure 3.2: (a) μ PL spectra of the NV⁰ center, with and without bias. (b) Transition scheme of the NV⁰ center, illustrating the effect of the uniaxial stress on the different states of the level.

As far as it is known from literature [111, 92], the energy splitting of the degenerate ground state E can be interpreted as the effect of an external electric field (the Starck

effect) [111] or as the effect of a stress field (the Jahn-Teller effect) [92] or also a combination of both. The simplest hypothesis is that the electronic levels associated to the NV^0 center shift (Stark shift), because the electric field is not perfectly screened at the surface and it propagates inside of the sample. For the Stark effect, the relationship between the energy splitting (ΔE) and the bias applied (or the electric field) is linear, as it is reported in equation (3.3). In some cases, a quadratic dependence of the energy splitting, of the NV^0 electronic states, with the applied electric field was associated to a Stark effect by P. Tamarat *et al.* [111].

$$\Delta E \propto F_{applied} = \frac{V_{DC}}{k \cdot R_{apex}} \quad (3.3)$$

If we suppose, as predicted by E. P. Silaeva *et al.* [16] that the electric field is screened at the surface of the specimen, the electronic states of the NV^0 defect shift under the action of the stress, which propagates inside the sample. In that case, following eq.(3.1) the relationship between the energy splitting (ΔE) and the applied electric field is quadratic:

$$\Delta E \propto \sigma \propto F_{applied}^2 = \left(\frac{V_{DC}}{k \cdot R_{apex}} \right)^2 \quad (3.4)$$

In this case, the energy splitting is associated to the Jahn-Teller effect that the stress induces on the ground state E , which splits into two components E_X and E_Y , as outlined above, fig.3.2(b). The effect of the stress on the energy transitions can be expressed through a secular matrix acting on the basis of the E_X and E_Y states [92]:

$$V_{stress} = \begin{bmatrix} \alpha + \beta & \gamma \\ \gamma & \alpha - \beta \end{bmatrix} \quad (3.5)$$

The terms α , β and γ which appear into the matrix (3.5) are elements which define the general matrix of the stress tensor [92]. The relationship between the uniaxial stress and the measured energy splitting is given by the equation (3.6), when the only non-vanishing stress component in the crystal reference system (x , y , z) is considered along the z -axis, which coincides with the axis of the tip. Taking into account this constraint,

the energetic perturbation (3.5) is given by the matrix (3.6)

$$V_{stress} = \begin{bmatrix} A_1 + 2B & 0 \\ 0 & A_1 - 2B \end{bmatrix} \cdot \sigma_{zz} \quad (3.6)$$

In the matrix of the equation (3.6) the elements A_1 and B were determined in the literature [92], with $A_1 = -0.743 \text{ meV/GPa}$ and $B = -1.86 \text{ meV/GPa}$. The equation (3.6) can be written also in the form of the linear equation (3.7):

$$\Delta E_{a,b} = c_{a,b} \cdot \sigma_{zz} \quad (3.7)$$

with the coefficients $c_a = A_1 + 2B = -4.5 \text{ meV/GPa}$ and $c_b = A_1 - 2B = 3.3 \text{ meV/GPa}$. Since the Jahn-Teller effect induces a larger energy splitting of the two electronic states E_X and E_Y than the Stark effect, in order to distinguish between the pure Jahn-Teller effect and the superposition of this one with the Stark effect, we should be aware if the electric field penetrates or not inside diamond nanoneedles. In order to know that, Field Ion Microscopy ‘FIM’ experiments were performed, as reported by Lorenzo Rigutti *et al.* [57]. FIM measurements demonstrate that diamond tips screen the electric field, under a bias of several kV . In FIM the sample is biased at high voltage ($10kV$) and an imaging gas (Ne at $p \sim 10^{-5} \text{ mbar}$) is introduced in the vacuum chamber. The gas is field-ionized close to the tip surface by tunnel effect, if the field at the tip apex is higher than the ionization field of the gas (35 V/nm for Ne). Then, positive ions of Ne^+ are projected on the detector and an image of the surface of the samples with atomic resolution is obtained, as shown in figure 3.3. The temperature was kept at $T = 50K$ during the FIM experience. The formation of the FIM image (figure 3.3) proves that the electric field at the surface of the tip is higher than 35 V/nm . In absence of the screening effect, the electric field expected for the diamond tip (with $\epsilon_r = 5.7$) at the same experimental conditions (T , p and V_{DC}) is of the order of 0.2 V/nm , which is too low to field ionize the image gas. These experimental analyses were considered as a good proof to conclude that the electric field does not penetrate inside of the diamond tip, so, in the section 3.2.3, the energy splitting of the NV^0 ZPL is related only to the stress-field effect.

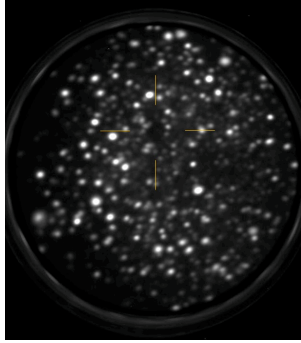


Figure 3.3: Field Ion Microscopy image of the apex of a diamond needle. The yellow markers approximately indicate the position of the $\langle 001 \rangle$ pole.

3.2.1 Experimental results obtained on the NV^0 stress-sensor: dependency on the bias

The diamond-tip specimens, as reported in Chapter 1, section 1.4, after the *fishing* step, are observed by SEM in order to get access to their geometry before the analysis. Here we report on the experiments performed on two different diamond tips, whose geometrical characteristics are resumed in the table 3.1.

needle specimen	apex radius R_{apex} (nm)	base radius R_{base} (nm)	length L (μm)
Tip 1	69	1200	48
Tip 2	150	1800	40

Table 3.1: Geometrical parameters of the analyzed diamond needles [57]

During the analysis the ~ 150 fs laser pulse of the La-APT/ μ -PL system was focused with a spherical mirror onto the diamond specimen with a beam waist of around $1.5 \mu\text{m}$. This large spot width is set in order to minimize the drift-induced variations of the evaporation rate, while the potential bias is applied on the diamond sample. The

same laser beam excites radiative transitions inside the specimen and the PL signal is collected and analyzed through a grating spectrometer, as outline in Chapter 1. The analyses were performed with an average excitation power $P = 400 \mu W$, the excitation wavelength at $\lambda_{exc} = 260 nm$ and the frequency of $\nu_{laser} = 500 kHz$. The exciting wavelength ($\lambda_{exc} = 260 nm$), which corresponds to an exciting energy of $E_{exc} \sim 4.77 eV$, cannot promote the electronic transition from the valence band to the conduction band of a pure diamond crystal, but it is enough to activate the emission from some impurities and color centers present into the diamond crystal lattice. During the experiments, the APT-detector is not used as a nanoanalysis tool, but rather as position sensor for the laser spot. The APT analysis were not performed for two main reasons:

1. a higher electric field ($>10 V/nm$) is required in order to evaporate the whole diamond specimen and, at high values of the V_{DC} bias, electrical discharges inside the APT experimental chamber can occur, with the risk to flash the specimen or to damage the sensors, which are inside or are connected to the chamber;
2. the probed color centers, through the μPL system, are present not only at the apex of the diamond nanotip, but within its volume, along all the length of the tip. The evaporation of the diamond specimen can be even more complicated if the sizes of the tip are too big in order to trigger the field ion evaporation.

The evaporation and the 3D APT-reconstruction of diamond nanotips containing color centers could be an interesting goal to reach in future studies, since the nature of some of these color centers, in diamond specimens as in other materials, likes SiC [112, 113, 114], still need to be discovered [115].

Therefore, the APT detector was used as a sensor of the laser spot position along the tip, because it is possible to collect a direct carbon evaporation, only when the laser spot is positionated on the needle apex. The APT 3D virtual reconstruction of diamond nanoneedle specimens was not carried out. The μPL signal from the NV^0 ZPL acquired with the laser impinging on or close to the apex of the needle 1 and needle 2, for different values of the voltage applied on the sample are reported in the spectra in fig. 3.4. As it is possible to observe, both the spectra show that the ZPL of the NV^0 center splits in two main components, labeled a and b . In the spectra related to the needle 1 further

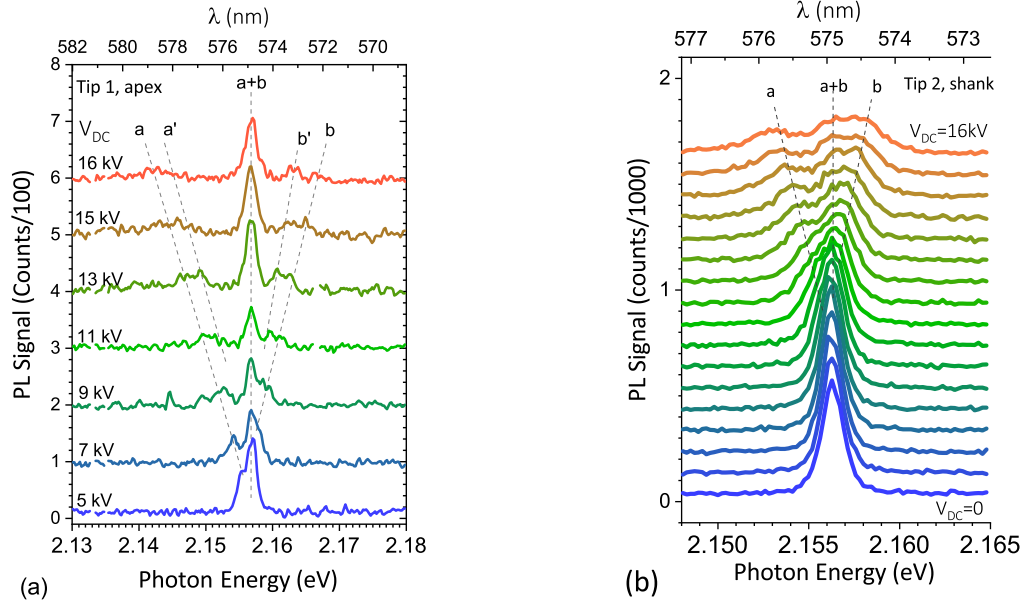


Figure 3.4: Optical study of the NV⁰ ZPL as a function of the applied bias. μ PL signal from the NV⁰ ZPL acquired with the laser impinging on the apex of the needle 1 (a) and the needle 2 (b) for different voltages applied to the specimen considered. The different spectra were vertically shifted to be readable. The NV⁰ ZPL splits up into two main components, labeled 'a' and 'b', and further components, 'a'' and 'b'', are visible at the highest voltages, for the needle 1. The nonsplit 'a + b' component remains visible due to the residual emission from the rest of the needle shank. The dash lines are guides for the eye.

components a' and b' are visible at highest voltages. The a' and b' components are the a and b lines, associated to the NV^0 electronic states, related to the centers placed further from the position where the laser spot is focused, but they are anyway excited. Indeed the laser spot covers a volume of $\sim 1\mu m \times (100nm)^2$, when it is positioned at the apex of the tip, an optic waveguide effect inside of the diamond nanoneedle is expected. A residual emission of the non-split component $a + b$ is present in all the spectra and it is due to the emission of the NV^0 color centers along the shank that are not affected by the effect of the V_{DC} bias. The plot in the fig. 3.5(a) reports the energy difference of the a and b peaks position with respect to the nonsplit component $a + b$, evaluated by the spectra in fig. 3.4, as a function of the bias applied. As it is possible to observe, the trend of the energy splitting of the lines a and b varies as a quadratic function of the bias applied V_{DC} , in agreement with the relationship (3.7), which takes into account only the effect induced by a stress-field on the electronic states of the NV^0 center. Therefore, the energy splitting observed into the spectra (figure 3.4) allows to determine the uniaxial stress acting along the needle axis, using the equation (3.7). The plots in fig. 3.5 are related to the spectra reported in fig. 3.4. In fig. 3.5(b) the dependence of the energy splitting of the a and b components on the square of the applied voltage is reported. The spectra are collected with the laser spot focused at a position assumed as the apex of the needle 1 and at $3\mu m$ from the apex position of the needle 2 (through the equation (3.7)). The energy splitting allows determining the uniaxial stress acting along the needle axis, which are reported on the right-hand side axis, according to the parameters c_a and c_b defined in literature. As deduced by the equations (3.1) and (3.2), the stress induced by the high electric field depends on the geometry of the probed tip. A schematic of the ideal and real shape of the diamond-needle is reported in figure 3.6. From the figure 3.6(a) it is visible that the apex of the needle can be approximated as an hemispherical shape and the shank of the needle as a truncated cone, as shown in fig.3.6(b). In agreement with this modelization, the stress acting at the apex of the sample can be considered as hydrostatic, while at distances from the apex equal to several R_{apex} , the resulting stress acting on the axial cross section of the needle is considered uniaxial, with the only non-negligible component that coincides with the needle axis. The resultant tension \vec{T} along the needle axis is

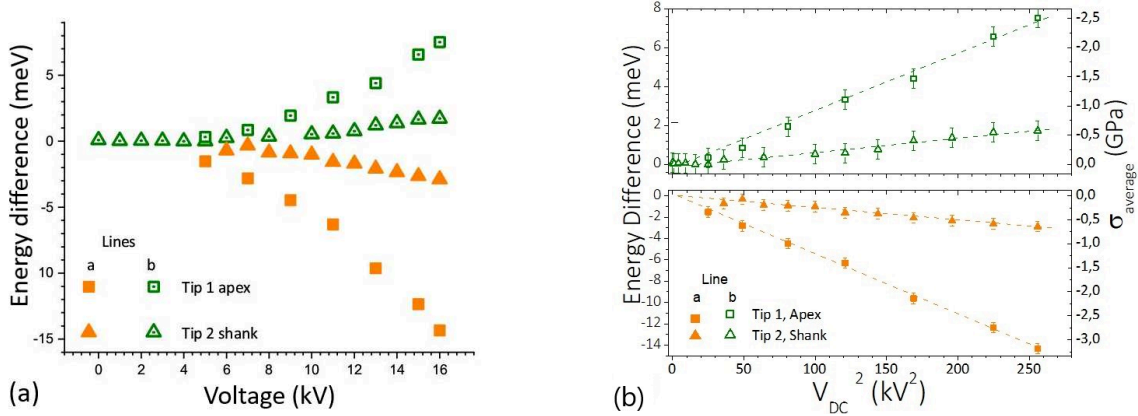


Figure 3.5: Dependence of the energy splitting of the ZPL of the NV^0 center (left-hand side axis) of the a and b components on the voltage applied (a) and the square of the voltage applied (b). The data were collected around the apex position of the Tip 1 and around $3\mu m$ from the apex of the Tip 2. In fig.(b) on the right hand side axis the related stress associated to the observed energy splitting is evaluated, according to parameters reported in literature [92].

defined as (3.8):

$$\vec{T} = \pi R_{apex}^2 \sigma_{apex} \hat{n}_{<001>} \quad (3.8)$$

and it is considered constant along the cone. The data, reported in fig.3.5(b), were collected with the laser spot focused at the apex of the diamond needle with a laser beam waist of $1.5\mu m$, which means that the signal collected comes from a region localized around the first $1.5\mu m$ below the apex of the needle. If the stress is considered as hydrostatic only at distances from the apex equal to R_{apex} and uniaxial from that position until the tip base, then the equation (3.7) can be used and considered as valid independently on the position where the laser beam spot impinges onto the diamond specimen.

In order to check out the C_{3v} symmetry of the NV^0 diamond centers, polarization-resolved analysis were performed focusing the laser spot at $\sim 3\mu m$ from the apex of the needle 2 and applying a positive bias $V_{DC} = 16 kV$. The uniaxial-stress-field acts along the needle axis, which corresponds to the $<001>$ crystalline direction and, as illustrated in fig.3.6(e), the exciting laser radiation has associated the electric vector

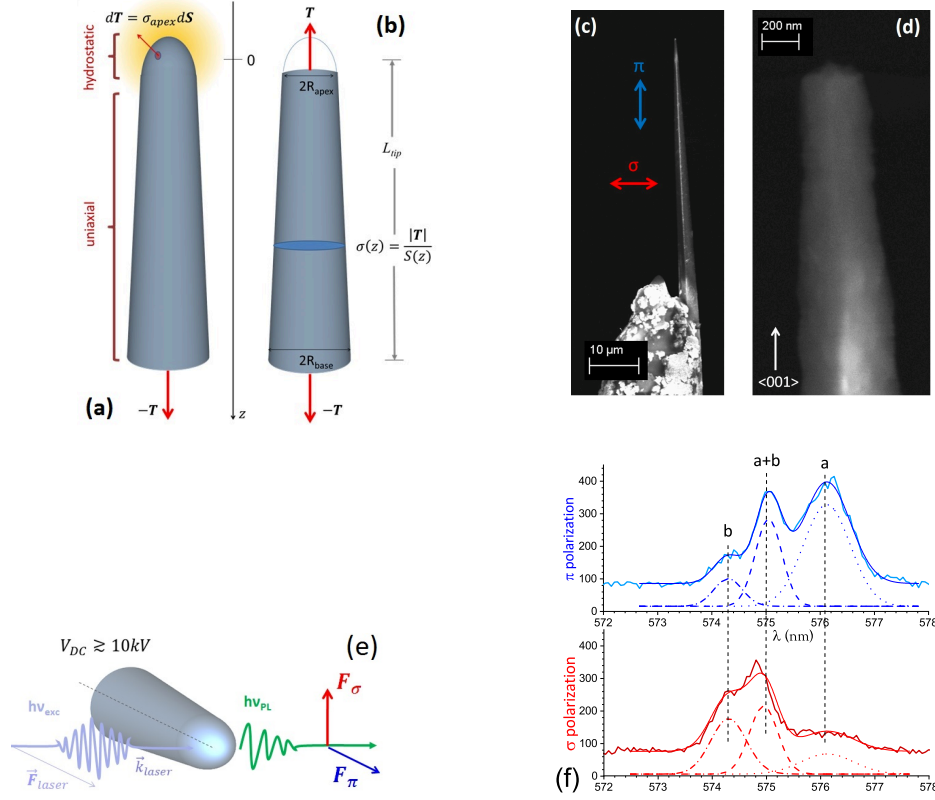


Figure 3.6: Stress model of nanoscale needles under high electric field. The image illustrates the generation of the hydrostatic stress at the needle apex (a) and its propagation along the needle as uniaxial (b). Scanning Electron Microscopy image of the diamond needle 2 (c), glued on the tungsten support; the π – and σ – directions correspond to the notation for the PL analysis; (d) magnification on the apex radius of the needle 2. (e) Schematic of the polar direction of the electric field associated to the emitted laser radiation and (f) polarization spectra of the analysis of the NV⁰ ZPL acquired on the shank of the needle 2 at $V_{DC} = 16$ kV.

F_{laser} , orientated along the same direction.

The polarization measurements were performed along different directions of the emitted signal with respect to the needle axis direction (parallel to F_{laser}), assumed as the reference direction. In the case labeled as π -polarization, the emitted signal is collected at the parallel direction (0° with respect to the reference direction), while the σ -polarization corresponds to the collection of the emitted signal at the perperpen-

pendicular direction (90° with respect to the reference direction). In both configurations (π - and σ - polarization), the ‘ a ’ and ‘ b ’ lines related to the NV^0 PL signal, under the stress-field, are visible, as shown in fig. 3.6(d). The ratio between the amplitude of the ‘ a ’ and ‘ b ’ peaks changes if we compare the spectrum collected at the π - *polarization* and the spectrum collected at σ - *polarization*. The polar representation of the area of the two components ‘ a ’ and ‘ b ’ of the NV^0 ZPL (fig 3.7), shows, in agreement with the literature [116], a trigonal C_{3v} symmetry, with the intensity of the ‘ b ’ (‘ a ’) line exhibiting a minimum (maximum) at 0° and 180° , π polarization, and a maximum (minimum) at 90° , σ polarization. The intensity ratio $\frac{b}{a}$ is equal to 0.46 in π polarization and to 3.5 in σ polarization, which is close to the literature values of 0 (π) and 3 (σ), respectively [117].

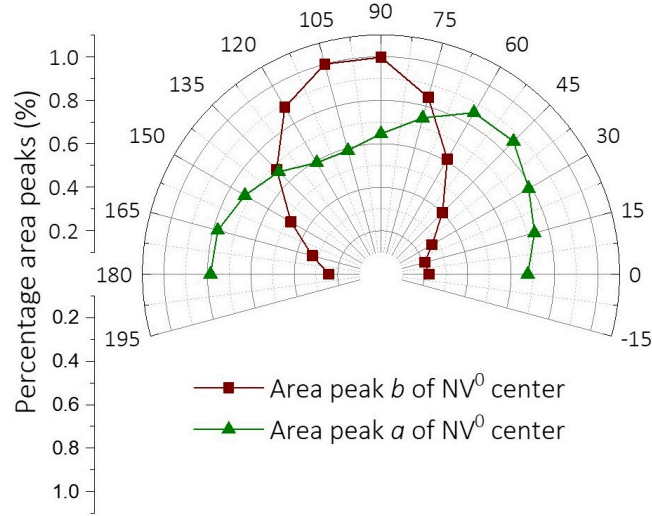


Figure 3.7: Polarization-resolved analysis of the NV^0 ZPL acquired at $\sim 3\mu\text{m}$ from the apex of the Tip 2.

3.2.2 Experimental results obtained on the NV^0 stress-sensor: dependency on the position

The piezo-spectroscopic study of diamond nanoneedles was performed not only in regions close to the apex of the diamond needle samples, but also at different positions

along the axis of the tip, in order to study the evolution of the stress along the tip and to verify if the exposed model fits well the data experimentally collected.

The propagation of the stress along the needle shank was approximated by a 1D model where the uniaxial stress is given by (3.9):

$$\sigma_{zz}(z) = \frac{|\vec{T}|}{S(z)} \quad (3.9)$$

where the axial cross section of the needle $S(z)$ is defined in the equation (3.10):

$$S(z) = \pi(R_{apex} + \frac{(R_{base} - R_{apex})z}{L_{tip}})^2 \quad (3.10)$$

all the variables which appear in the equation were defined into the table 3.1, respectively for the two probed diamond needles. The equation (3.9) can be written also by specifying the relation between the $\sigma_{zz}(z)$ uniaxial stress and the $\sigma_{zz}(0)$ stress at the apex of the tip, as reported in the equation (3.11):

$$\sigma_{zz}(z) = \sigma_{zz}(0) \cdot \frac{S(0)}{S(z)} \quad (3.11)$$

The spectra acquired at different position along the axis of the Tip 1, submitted to a bias $V_{DC} = 16kV$, fig.3.8(a), were fitted by the equation (3.9) or (3.11), in agreement with the 1D model, as showed in the plot in fig. 3.8(b).

The energy shift of the a and b lines allowed to evaluate different values of the stress as a function of the position along the tip. Then, the value of the stress at the apex $\sigma_{zz}(0) = \sigma_{apex}$, which appears in the equation (3.11), was estimated from the fitting of the data by the equation (3.11), taking into account the axial extension of the laser spot for the associated incertitude on the position where the evaluated stress could act along the tip. For instance, for the Tip 1 that value is $\sigma_{apex} = (7 \pm 1) GPa$, as it is reported in the plot in fig.3.8(b). In figure 3.8(c) the data related to the diamond needle 2 are fitted using the equation (3.9), where the axial extension of the laser spot is the absolute error associated to each position along the z -axis of the tip. The result of the 1D model fit yields a stress equal to $\sigma_{apex} = (1.8 \pm 0.3) GPa$, acting at the apex of the

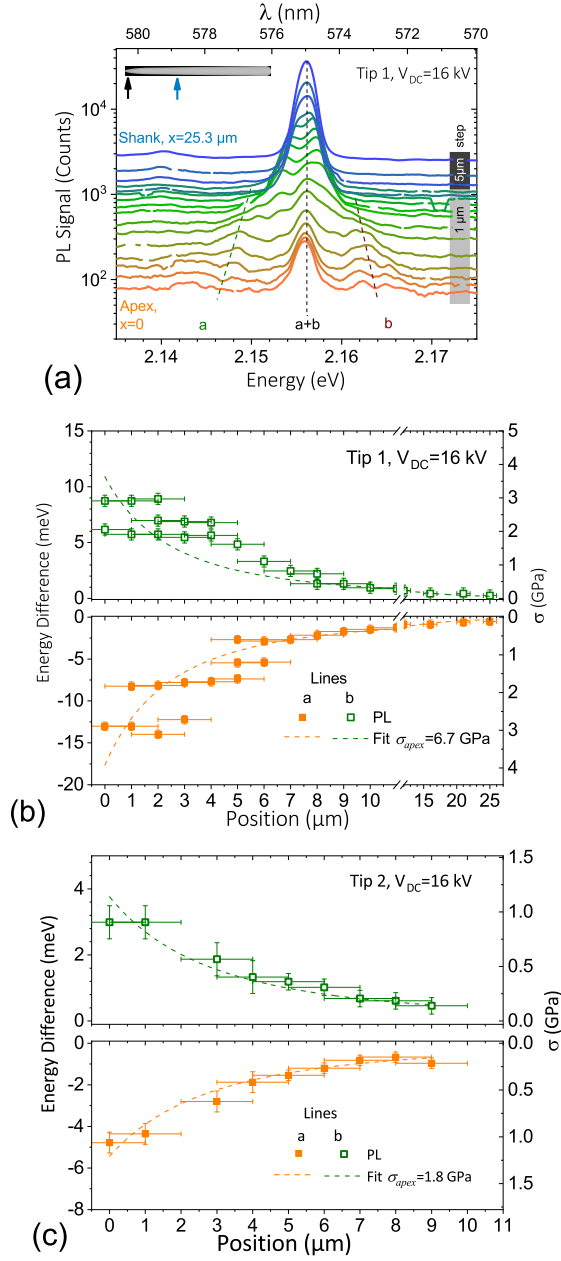


Figure 3.8: Spatially resolved study of the stress propagation along the needle axis. (a) μ PL spectra of the NV^0 ZPL acquired along the axis of the needle 1, at $V_{DC} = 16$ kV. (b, c) Energy splitting (left-hand side ordinates) of NV^0 components (a bottom and b top of the plot) and related uniaxial stress along the $\langle 001 \rangle$ (right-hand side ordinates) as a function of the position along the axis of the needle 1 (b) and needle 2 (c). The fit of the experimental data yields a value of the stress at the apex.

diamond Tip 2. From stress acting at the apex of these two tips, the corresponding electric field can be calculated by the equation (3.1): $F_S = (38 \pm 3) V/nm$ for the needle 1 and $F_S = (18 \pm 2) V/nm$ for the needle 2. The significant difference of the value of stress and electric field between the two diamond nanoneedles can be explained in terms of their geometry. The first needle has a sharper apex radius than the needle 2 and as consequence, at the same values of the V_{DC} bias applied, a higher stress is acting on the needle 1 than on the second one. The equation (3.2) allowed to evaluate the coefficients k_f for the two needles, which are, respectively, $k_f = (5.0 \pm 0.3)$ for the needle 1 and $k_f = (6.3 \pm 0.3)$ for the needle 2, which increasing value is expected as a function of the increasing shank angle of the needle. The stress evaluated at the apex of the Tip 1 ($\sigma_{apex} \sim 7 GPa$) is of the same order of magnitude of typical values of Peierls stress, reported within the articles [118, 119]. Since the Peierls stress is defined as the force needed to move a dislocation within a plane of atoms in the unit cell, then the magnitude of this force varies periodically as the dislocation moves inside the plane. The probed diamond nanoneedles contain a certain concentration of defects and not a perfect conic shape, figure 3.6(d), then shear components may develop, yielding dislocation movements close to the apex [120]. The apex stress of $7 GPa$ is also close to the value of the yield strength of diamond with extended defects [121]. The diamond needles analyzed were observed by SEM also after the analysis and they were crack-free and did not exhibit fractures. As reported into the published article [57] about the piezo-spectroscopic study on diamond nanoneedles, the evaluation of the stress is useful also in order to compare our results with the values of strain reported from previous works based on cantilever systems [122, 123, 124, 125]. The conversion between the evaluated apex stress and the related strain comes from the Hooke's equation: $\sigma_3 = E \cdot \epsilon_3$, defined in the section 2.4.1 of the Chapter 2. Considering the Young's modulus of diamond, $E = 1050 GPa$, then it is possible to estimate an upper bound for the electrostatically induced strain state of $\epsilon_{zz} \approx 0.3\%$. In the single-crystal diamond cantilever system, the maximum value obtained for the strain is $\epsilon \approx 0.25\%$, which is very close to our case. The difference between the cantilever system for the application of a mechanical stress and the electrostatically induced stress is that in the first case, the system can also work in compression, while in our case only in tension. Anyway, through this new

piezo-spectroscopic technique is possible to probably obtain higher values of the tensile strain, using smaller tip radii, but at the same time field-evaporation will simultaneously occur.

3.2.3 Experimental results obtained on the NV^0 stress-sensor: investigation of the radiative lifetime

The characterization of the NV^0 color centers was performed also by time resolved μ PL measurements (TRPL). These kind of measurements were useful in order to study the temporal dynamic of the recombination processes. Indeed, when the laser radiation is absorbed by the sample, electron-hole pairs are generated between the intra-gap levels and their quantity depends on the laser pulse power. As time passes, the number of carrier pairs which did not recombine decrease, so, it follows that the PL intensity signal is related to the lifetime of the radiatively recombination processes. The time dependence of the number of excited electron-hole pairs is proportional to the intensity of the collected PL signal. The time dependence of the PL signal can be expressed as:

$$I(t) = I_0 e^{-\frac{t}{\tau}} \quad (3.12)$$

where: I_0 is the PL intensity at $t = 0$ s, τ is the lifetime associated to the luminescence signal of the neutral-nitrogen vacancy, with ZPL at $\lambda = 575$ nm. As reported into the section 2.5.3 of Chapter 2, the NV centers were largely studied in literature and the value of their radiative lifetime ' τ ' is not affected by the temperature range at which they are observed [126], but it depends on the structure and structural defects present into the diamond studied (*e.g.* bulk [102]: $\tau = 20$ ns, nanodiamond [99]: $\tau \sim 25$ ns, for the single-crystal diamond needles [88]: $\tau = (2.8 \pm 0.3)$ ns and Hanzawa *et al.* [126] found two different values of decay time associated to the NV^0 center: $\tau = 2$ ns and $\tau \sim 9$ ns, respectively for the short and long component of the decay curve, for synthetic Ib diamond samples).

The fig.3.9(a) shows the 2D colormaps which were recorded by streak camera (at $P = (5.0 \pm 0.5)$ mW, $\lambda_{exc} = (260 \pm 5)$ nm and $T = 25$ K). The 2D datasets, related to

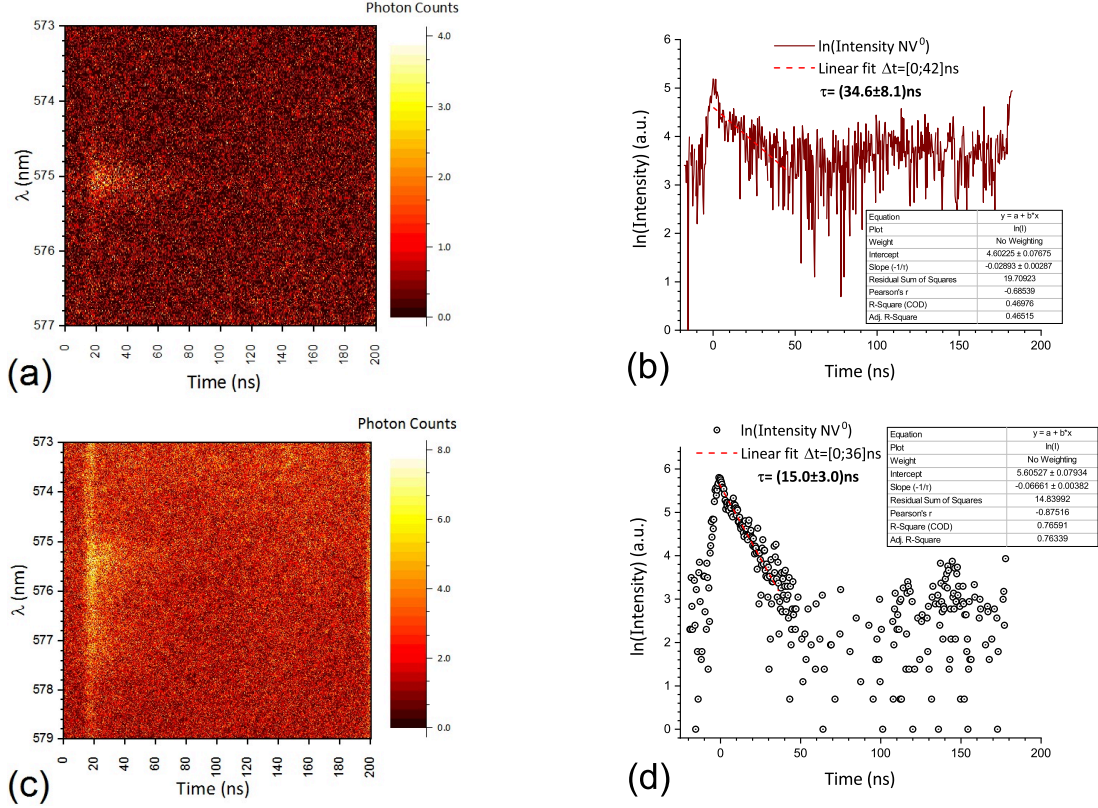


Figure 3.9: Time distribution of events of the 575nm line (NV^0 center), detected at $T=25$ K, $\lambda_{exc} = 260$ nm, beam power of $P_{exc} = (5.0 \pm 0.5)$ mW, focusing the laser on the same position (at the apex of the diamond tip). The 2D colormap (a) was obtained without applying any bias. While the 2D colormap (c) was acquired at $V_{DC} = 16$ kV. In both, (a)-(c), 2D colormaps the brown color is associated to the lowest number of detected events and the white color to the highest ones. The (b)-(d) integrated spectra of the events, over the energy ranges of the NV^0 peak: $[574; 576]$ nm, are related, respectively, to the color maps (a) and (c). Integration time ranges are indicated, in (a)-(c), on the streak detection map with bars of the corresponding colors. The acquisition time of the data collected at $V_{DC} = 0$ kV, (a)-(b), is 1 hour, while the acquisition time of the data collected at $V_{DC} = 16$ kV, (c)-(d), is 12 hours. Red dashed lines correspond to exponential decay adonlyment in linear scale (b)-(d).

the figures 3.9(a) and (c), were integrated over the restricted wavelength range $\Delta\lambda = [574; 576]$ nm, in order to obtain the related decay curves, as shown in figures 3.9(b)

and (d). The decay curve is characterized by a single peak with a really short rise-time (comparable with the time resolution of the streak-camera of $\Delta t \sim (6.0 \pm 1.2) \text{ ns}$) and longer decreasing tail. The radiative lifetime is experimentally determined by fitting the decay curves with decay models, equation (3.12). The 2D colormap in fig. 3.9(a) was acquired without applying any bias, $V_{DC} = 0 \text{ kV}$, focusing the laser spot ($d_{spot} \approx 1.5 \mu\text{m}$) on the apex of the diamond needle 2 and the acquisition time was one hour. For the 2D colormap in fig. 3.9(c), the position of the laser spot was not changed, but a bias equal to $V_{DC} = 16 \text{ kV}$ was applied and the acquisition time of the measurement was 12 hours. Despite the increasing of the acquisition time, the measurements, of both 2D colormaps, show low signal/noise ratio, which is clearly visible from the related decay curves fig. 3.9(b) and (d). This low signal/noise ratio, shown in fig. 3.9, is supposed to be related to the low amplitude of the NV^0 PL-signal, when the laser spot impinges on the apex of the diamond tip. The decay time, evaluated by the decay curve in fig. 3.9(b), without applying any bias, is $\tau = (34.6 \pm 8.1) \text{ ns}$, with an incertitude of $\sim 24\%$, due to the low signal/noise ratio. The spectra in fig. 3.9(d), obtained by the 2D colormap in fig. 3.9(c), shows a better quality of the signal/noise ratio. The NV^0 decay time is evaluated to be: $\tau = (15.0 \pm 3.0) \text{ ns}$, with an incertitude of $\sim 20\%$. Unfortunately, we have only one result related to the decay time, evaluated respectively with and without applying any bias, close to the apex position. The different values of the decay time obtained at $V_{DC} = 0 \text{ kV}$ ($\tau = (34.6 \pm 8.1) \text{ ns}$) and $V_{DC} = 16 \text{ kV}$ ($\tau = (15.0 \pm 3.5) \text{ ns}$), suggest that the high bias affects also the lifetime associated to the NV^0 radiative emission, as it is expected by a changement of the geometry of the diamond tip or the relative distance between the atoms due to a strain/stress effect acting on the diamond needle (at $V_{DC} = 16 \text{ kV}$). But the results obtained cannot be considered conclusive. Another measurement at $V_{DC} = 16 \text{ kV}$ was performed in short time scale (5 ns), along the shank of the tip. The decay curve is reported in fig. 3.10(a) and the related acquisition time is around $\approx 2 \text{ hours}$.

The characteristic decay time of the NV^0 decay curve in fig. 3.10(a) was found to be $\tau = (1.34 \pm 0.42) \text{ ns}$. That value, obtained through the linear fit, equation (3.12), indicates that in short range time a fast decay time seems to occur, in agreement with what reported by Malykhin *et al.* [88]. The NV^0 decay curves acquired without bias,

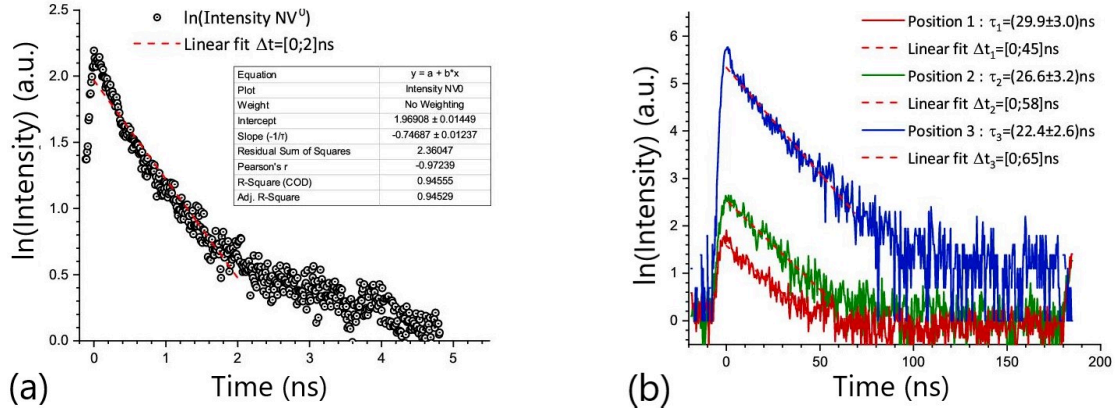


Figure 3.10: Time dependences of the photoluminescent 575nm line (NV⁰) decay on (a) short and (b) long time scale. Excitation wavelength is $\lambda_{exc} = 260 \text{ nm}$ and the beam power is $P_{exc} = (5.0 \pm 0.5) \text{ mW}$. Red dashed lines correspond to exponential decay adonlyment in semi-logaritmic scale (a) and (b).

on long time scale (200 ns), at three different positions along the diamond needle shank are reported in fig.3.10(b) and each signal was acquired in a range of time of $\approx 2 \text{ hours}$. The three different positions are disposed in increasing order, moving from the apex towards the base of the diamond tip and the related decay times are:

- position 1: $\tau_1 = (29.9 \pm 3.0) \text{ ns}$
- position 2: $\tau_2 = (26.6 \pm 3.2) \text{ ns}$
- position 3: $\tau_3 = (22.4 \pm 2.6) \text{ ns}$

These results show that the decay time of the NV⁰ centers evolves along the diamond tip and it seems to decrease as the diameter of the diamond tip becomes larger. The average value of the decay time acquired at these different positions is $\tau = (26.3 \pm 5.0) \text{ ns}$ is in quite good agreement with the decay time previously reported in literature: $\tau = (29.41 \pm 6.98) \text{ ns}$ [99] and $\tau = (28 \pm 1) \text{ ns}$ [110], for nanodiamond samples. The decay time ' $\tau_1 = (29.9 \pm 3.0) \text{ ns}$ ' at the position 1, the closer to the diamond tip apex, is also comparable with the value ' $\tau = (34.6 \pm 8.1) \text{ ns}$ ' calculated from the decay curve in fig.3.9(b).

In ref.[88], fluorescent lifetime imaging spectroscopy ‘FLIM’ was used in order to evaluate the decay time related to different color centers present into the same kind of diamond tip specimens. In this article [88] it is reported that a decrease in size of the diamond crystal corresponds to an increment in lifetime, in the long time range scale, of the NV centers. So, the lifetime of the NV centers in a diamond needle is expected to decrease from its apex towards its base. Since the internal structure is quite similar over the length of the diamond tips, the only explanation for this variation of the characteristic decay times, in particular for the NV^0 and SiV centers, was associated to the reduction of the crystallite thickness of diamond needles. In ref.[99], cited in the section 2.5.3 of Chapter 2, is reported that “in agreement with local density of states (LDOS) theory, as the crystal size becomes smaller, an increase of the NV^0 lifetime is expected and as the size of nanodiamond decrease, a decrease of the lifetime, which could might be related to a preferential coupling to non-radiative pathways, is expected”.

For what concerns the study of the bias on the radiative lifetime of the NV^0 centers, we can conclude that this study gives some clues to think that the stress induced by the high bias decreases the decay time of these color centers, but further experimental proofs are required.

3.3 The color-center at $2.65eV$

The piezo-spectroscopic study performed on the NV^0 center was achieved using the coupled La-APT/ μ PL setup as an original optical contactless-piezo-spectroscopic system.

Thanks to this new technique the stress-field sensitivity of the nitrogen-vacancy ‘ NV^0 ’ center was compared with the one of the color center detected with ZPL at $468nm$ or $2.65 eV$ in the wide-spectrum in fig.3.11. The reasons why it was decided to study this color center can be classified in this order:

1. Looking at the whole spectrum at $V_{DC}=0kV$, in fig.3.11, the ZPL of the center at $2.65 eV$ has almost the same intensity as the NV^0 center, so the $2.65 eV$ and the NV^0 have both a good PL signal at the exciting wavelength, $\lambda_{exc} = 260nm$,

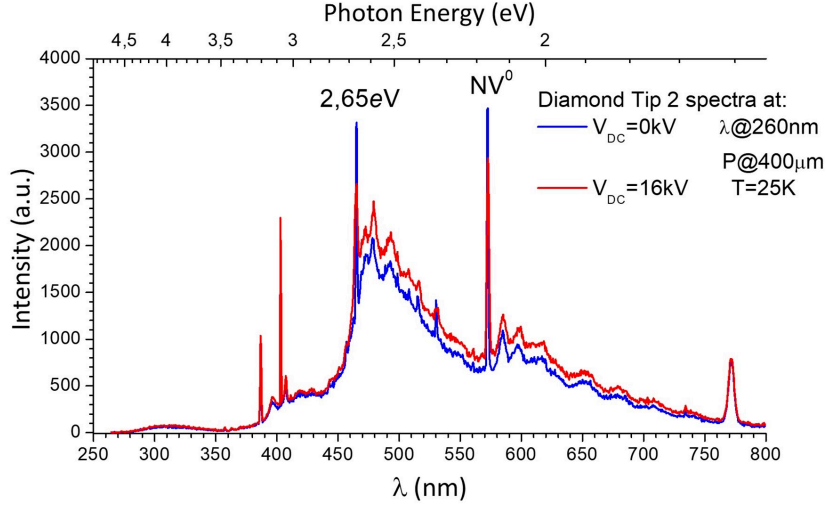


Figure 3.11: PL signal of the diamond Tip 2, at the experimental conditions reported in caption of fig.3.1. The blue spectrum was acquired without bias, while the red one at $V_{DC}=16\text{kV}$ and in both the spectra the focus is on the signal of the 2.65 eV center and the NV^0 .

selected to perform the analysis.

2. The PL signal of the center at 2.65 eV is visibly affected by the applied V_{DC} bias, as it is shown in the spectra in fig.3.11.
3. The potential of the center at 2.65 eV as a stress-sensor was never tested and also the structure and symmetry of this center are not well known in literature[6, 116, 4].

As demonstrated in ref. [57], the NV^0 optical transition can be controlled by a stress/strain field and this kind of study opens the way to the realization of strain-coupled hybrid spin oscillator systems, where the NV center spins interact with the resonant phonon modes of a macro-mechanical resonator through crystal strain. Some applications of these systems are reported in the articles[122, 123], where the NV centers were chosen for their ability to couple to external strain fields. In figure 3.11, at $V_{DC} = 0\text{ kV}$, the NV^0 peak and the one with ZPL at 2.65 eV have comparable amplitudes, while, under the bias $V_{DC} = 16\text{ kV}$, the intensity of the 2.65 eV center decreases more than the

intensity of the NV^0 center. This trend suggests that the 2.65 eV color center could be also more sensitive to the stress-field than the NV^0 defect. In order to observe and compare the energy splitting of the peaks, as it was done for the NV^0 defect, a restricted region of the spectra, centered on the value of the ZPL of the interested defect, is acquired with a grating density of 1200 groove/mm and $\lambda_{blaze} = 400\text{ nm}$. That choice allows to increase the spectral resolution since 0.5 meV , which allows to appreciate the expected energy shift of the peaks, of the order of some meV for the NV^0 defect. Before to move to the experimental analysis related to the 2.65 eV center, it is worth to point out that the nature of this color center was largely discussed in literature[107]. For instance, in agreement with the energy range where this defect can be detected $E_{ZPL} = [2.648; 2.654]\text{ eV}$, it was supposed that it corresponds to the TR12' diamond defect. The TR12' is called like that, because its ZPL is 10 meV blue-shifted with respect to the TR12 color center [127, 5]. The 2.65 eV center was observed on most of the as-grown chemical vapor deposition (CVD) diamond films studied by Iakoubovskii *et al.*[5]. Unlike the TR12 center, which anneals out at 800°C , the intensity of the 2.65 eV center was almost constant in CVD diamond films grown annealed up to 1000°C [6]. The potential of the 2.65 eV center as a stress-field sensor was never tested before[4, 6, 128], but the TR12 center was observed in the PL spectrum of diamond decades ago, by Davies *et al.*[4], and piezo-spectroscopic studies were performed on it, in order to determine the strain susceptibility and the symmetry of this center. The measured strain susceptibility (sensitivity) of this center is lower than the one of the NV^0 center and the corresponding symmetry was not established[4]. Concerning the structure of the TR12 center Mainwood *et al.*[129], suggested that this center contains an interstitial carbon in a hexagonal site. Recently, Naydenov *et al.*[130] have demonstrated the ability of the TR12 center as single photon emitter, fueling interest about this color center and the related TR12' or the 2.65 eV center. About the TR12' center, Iakoubovskii *et al.*[5] suggested that it is a stressed TR12 center, with the stress generated through the lattice or some neighboring impurity, but the symmetry of this center is still not well known. In the next section, the contactless piezo-spectroscopy of the 2.65 eV center is used to prove that this color center could be a better candidate than the NV^0 center for the fabrication of strain-mediated coupling systems. Thanks to polarization-resolved $\mu\text{-PL}$

measurements, under strain field, more information about the symmetry and structure of the 2.65 eV center was obtained.

3.3.1 Piezo-spectroscopic study of the center at 2.65eV: dependence on the V_{DC} bias

Contactless piezo-spectroscopy studies were performed on three diamond specimens, synthesized by PE-CVD technique, as explained into section 2.5.1 of Chapter 2. The exact geometry of two of these samples was measured by scanning electron microscopy (SEM) and in the table 3.2, the geometrical characteristics of these two diamond specimens are reported.

needle specimen	apex radius R_{apex} (nm)	base radius R_{base} (nm)	length L (μm)
Tip 2	150	1800	40
Tip 3	71	500	21

Table 3.2: Geometrical parameters of the analyzed diamond needles [115]. The Tip 2 is the same specimen used for the piezo-spectropic analysis of the NV^0 center.

The SEM images of these two samples are reported in figure 3.12.

The experiments were performed at the same conditions reported for standard APT analysis: $T < 25 K$ and $p < 10^{-7} Pa$, applying a tuning positive bias $V_{DC} = [0; 16] kV$, and as for the NV^0 centers, using an excitation wavelength of $\lambda = 260 nm$ and average power of $P = 400 \mu W$. Also in that case, an incertitude of $1.5 \mu m$ has to be associated to the laser position on the tip, which corresponds to the waist of the laser beam, when it is focused on the diamond needle specimen during the analysis. In particular, a series of PL spectra was acquired for the 2.65 eV center and the NV^0 center with the laser spot focused on the apex of the needle 3, for different values of applied bias, from 0 kV to 16 kV, as reported in figure 3.13(a) and (b). The spectra of the NV^0 center are shown for comparison and as reference for the evaluation of the stress acting at the apex of the diamond needle, labeled ‘Tip 3’.

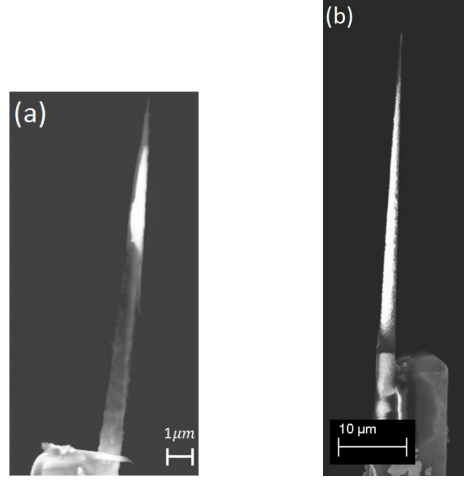


Figure 3.12: SEM images of the diamond nanoneedles: (a) the Tip 3, acquired with at magnification scale of $1\ \mu m$ and (b) the Tip 2, acquired at a magnification scale of $10\ \mu m$

The spectra of both the supposed TR12' center and the NV^0 center, at low bias, consist, within $1\ meV$ of spectral resolution limit of the setup, of single emission peaked at $E_{ZPL} = 2.65\ eV$ and $E_{ZPL} = 2.156\ eV$ respectively. At higher biases ($V_{DC} > 8\ kV$), the line splits up into two components, denoted as 'a' and 'b', which shift: 'a' towards lower energy and 'b' towards higher energy, as the bias is increased.

As explained in the section 3.2, the 'a' and 'b' lines which appears in the spectra of the NV^0 center (fig.3.13(a)) correspond to two different electronic transitions activated by the effect of the stress-field on the E ground state level of the NV^0 center. In analogy, the 'a' and 'b' lines, which appear in fig.3.13(b), can be associated to electronic transitions activated for the $2.65\ eV$ center under the effect of the stress field. Differently from the NV^0 , where the 'a' and 'b' lines have almost the same amplitude (fig.3.13(a)), in the $2.65\ eV$ center, the 'a' line has lower amplitude than the 'b' line, as visible in fig.3.13(b). Moreover, at high biases, a new b' line is visible, but none a' line is observed, probably because of its lower intensity, that it is covered by the noise level. The b and b' lines are attributed to two different centers, simultaneously excited by the laser beam, but subjected to a different perturbing stress-field, probably because they are placed at different positions inside the tip. The relationship between the energy splitting of the

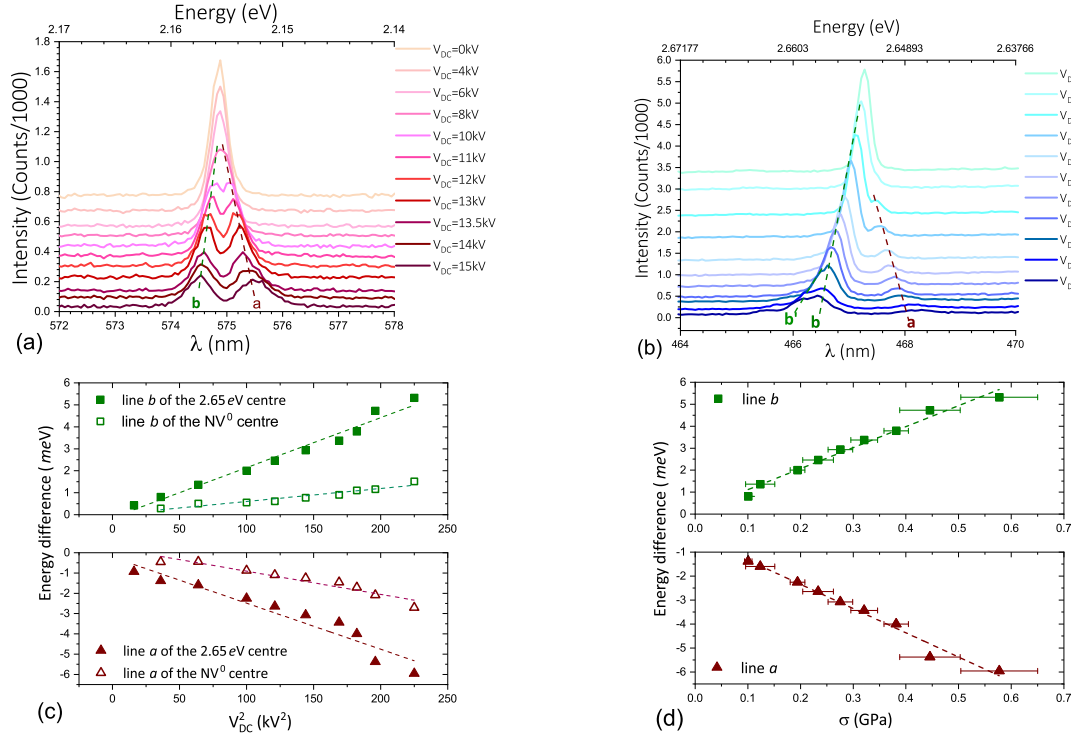


Figure 3.13: μ -PL signal acquired with the laser impinging on the apex of the diamond Tip 3, at different values of applied V_{DC} . The spectra related to the NV⁰ ZPL (a) and to the ZPL of the 2.65 eV center (b), which are vertically shifted for clarity. The ZPL at 0 kV, when the bias is increased, splits up into two main components 'a' and 'b' and the dashed lines are guides to the eye. (c) Dependence of the energy splitting of the 'a' and 'b' components on the square of the applied voltage, related to the spectra (a) and (b). (d) Dependence of the energy splitting of the 'a' and 'b' components of the 2.65 eV center with the stress along the needle axis <001> (crystal orientation).

‘*a*’ and ‘*b*’ lines is a quadratic function of the applied bias, as reported in the equation (3.7) and it is shown in figure 3.13(c). The uniaxial stress, acting on the diamond Tip 3, is evaluated by the equation (3.7), where the value of the NV^0 coefficients are taken by ref.[92] and the energy difference corresponds to the split positions of the peaks reported in the spectra in fig.3.13(a). The $\Delta E_{a,b}$ related to the NV^0 center can be used in order to calibrate the tensile stress at a fixed z position, as a function of the applied bias. The evaluated uniaxial tensile stress at $z \approx 0 \mu m$, as reported in fig. 3.13(d), was found to vary in the range: $\sigma_{average} = [0; 0.6] GPa$ with the variation of $V_{DC} = [0; 14] kV$. Also for the 2.65 eV center the trend observed between the energy splitting, $\Delta E_{a,b}$, of the ‘*a*’ and ‘*b*’ lines as a function of the average value of the applied stress, $\sigma_{average}$, is linear, in agreement with the equation (3.7). That equation can be written for the 2.65 eV center, as:

$$\Delta E_{a,b} = k_{a,b} \cdot \sigma_{zz} \quad (3.13)$$

Where the coefficients of proportionality in the equation (3.13) are obtained by the linear fit of the data reported into fig.3.13(d). Their values: $k_a = -(10.7 \pm 0.3) meV/GPa$ and $k_b = (10.0 \pm 0.3) meV/GPa$ are larger than the values of the $c_{a,b}$ NV^0 coefficients, by more than a factor 2. But, as discussed for the NV^0 analysis, the large laser beam waist does not exclude systematic errors related to the excitation of other color centers close to the apex position. A different position of the NV^0 or 2.65 eV centers can translate in a significant different stress state acting on one or the other. For this reason, spatially-resolved PL measurements were performed on Tip 2.

3.3.2 Piezo-spectroscopic study of the center at 2.65eV: dependence on the position

In parallel to what was done for the NV^0 center, the PL spectra of the 2.65 eV color center were acquired at different positions of the laser spot with respect to the apex of the Tip 2, applying a constant bias $V_{DC} = 16 kV$. When the laser is focused close to the apex of the needle, the ZPL of the 2.65 eV center splits up into different components, similarly to what shown into fig.3.13(b) and as showed into fig.3.8(a) for the NV^0 center. The energy splitting of the ‘*a*’ and ‘*b*’ lines for the two centers is plotted as a function

of the laser spot position with respect to the apex of the needle in figure 3.14.

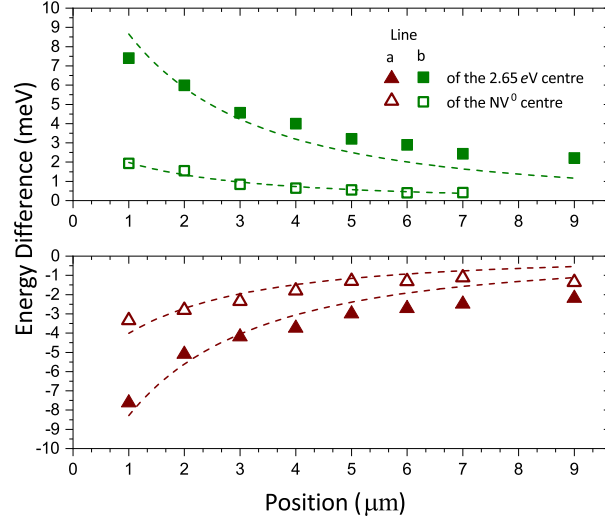


Figure 3.14: Evolution of the energy splitting related to the ‘*a*’ and ‘*b*’ lines related the 2.65 eV and the NV⁰ centers as a function of the position along the axis of the tip (<001> crystal direction).

Looking at the data reported into the plot in figure 3.14, the $\Delta E_{a,b}$ of the NV⁰ color center is higher than 1 meV up to 4 μm from the apex, but it progressively decreases to zero. The behavior of the 2.65 eV center is similar to that of the NV⁰ center, but the spectral shift is higher than 2 meV up to the furthest position of 10 μm. As discussed above, in section 3.2.2, and proved in ref. [57], the value of the uniaxial stress, at the coordinate z , for a circular cone geometry, depends strictly on the geometrical parameters of the tip (R_{apex} , R_{base} and L_{tip}), in agreement with the equation in the equation (3.10). For what concerns the Tip 2, the value of the stress acting at its apex: $\sigma_{apex} = (1.8 \pm 0.3) \text{ GPa}$ [57] was evaluated from the fit of the experimental data, related to the NV⁰ center, reported in fig. 3.8(c), through the equation (3.10). Therefore, using the equation (3.13), the value of the two coefficients, related to the 2.65 eV center, are evaluated: $k_a = -(11 \pm 1) \text{ meV/GPa}$ and $k_b = (10.0 \pm 0.5) \text{ meV/GPa}$. These values of the coefficients k_a and k_b , on the Tip 2, are in good agreement with the values obtained on the diamond Tip 3, so they can be considered as a new result related to the

2.65 eV center, since the value of these coefficients was evaluated with two independent methods. From the equations (3.7) and (3.13) it follows that the ‘ c_a ’ and ‘ c_b ’ or the ‘ k_a ’ and ‘ k_b ’ coefficients are related to the dipole moment associated to the NV⁰ and the 2.65 eV center, so the 2.65 eV center has an average dipole moment around two times larger than the NV⁰ defect.

3.3.3 Polarization spectroscopic study of the center at 2.65 eV under V_{DC} bias

In order to get more information on the symmetry of the 2.65 eV center, polarization-resolved PL spectroscopy was performed on the diamond Tip 3, while it was subjected to a bias of $V_{DC} = 16$ kV. For what concerns the polarization study of the NV⁰ center, the polar representation of the area of the two components ‘ a ’ and ‘ b ’ of its ZPL (fig.3.15(a)) confirms the trigonal C_{3v} symmetry of this center, in agreement with the literature [116].

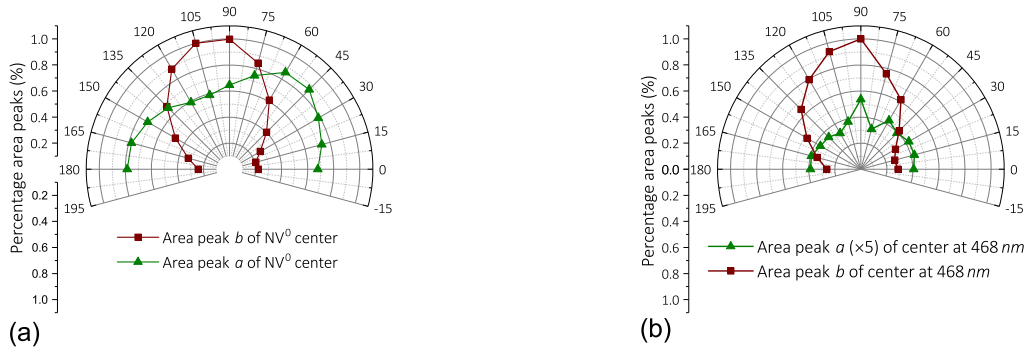


Figure 3.15: Polarization-resolved analysis of the NV⁰ ZPL (a) and the 2.65 eV center (b) acquired on the the apex of the diamond Tip 3.

In the case of the 2.65 eV center, the ‘ b ’ line follows the same polarization behavior of the ‘ b ’ line of the NV⁰ center, but, in agreement with what observed in figure 3.13(b), its intensity is higher than the intensity of the ‘ a ’ line almost of a factor 10. The ‘ a ’ line of the 2.65 eV center shows an increase in intensity of about 10% in π -polarization,

compared to the σ -polarization. Also, even though the polar behavior of the ‘ a ’ and ‘ b ’ lines of the 2.65 eV center are similar to the split components of the NV^0 , the intensity ratio $\frac{b}{a}$ is 3 in π -polarization and 10 in σ -polarization, which is incompatible with the monoclinic I or the triclinic symmetry, suggested in literature for the TR12 and TR12’ centers[117, 6, 4, 128].

In summary, the piezo-spectroscopic measurements performed on the 2.65 eV centers, which are present into needle-shaped diamond crystal, with nanometric apex radius and the axis oriented along the $\langle 001 \rangle$ crystal direction, allowed to conclude that:

1. the splitting of the 2.65 eV center is twice as large that of the NV^0 center. This result was confirmed by two different methodologies in order to vary the uniaxial tensile stress and on two different samples.
2. the symmetry found out for the 2.65 eV center, along the $\langle 001 \rangle$ direction, does not confirm the monoclinic I and also not the trigonal one. In order to determine the symmetry, piezo-spectroscopy should be performed applying uniaxial stress along different crystal directions.
3. since the 2.65 eV color center is largely present into the needle-shaped nanoscale diamond tips, it can be a valid alternative to the NV-centers in the framework of nanoscale probes of electromagnetic fields.

The study about the 2.65 eV color center was recently published in the article[115].

3.4 Multi-photon excitation of the NV^0 defect into the IR range

The multi-photon absorption (MPA) is a process that can occur in band-gap materials only if the energy of two or more absorbed photons ($n \cdot h\nu$) is higher than the energy gap ($\Delta E > E_{gap}$) or equal to the intragap electronic transitions ($\Delta E = E_e - E_g$) of the probed material. E_e and E_g label the energy of the excited electronic state and the energy of the ground electronic state, respectively, as reported in fig. 3.16.

In order to promote an electronic transition through a two- or multi-photon absorption, the photons have to be absorbed within a range of time given by the Heisenberg lifetime: ($\Delta t = \frac{\hbar}{\Delta E}$), which is of the order of a few fs for ΔE corresponding to the visible light spectral range.

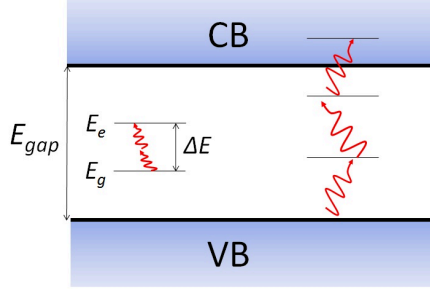


Figure 3.16: Schematic of the multi-photon transition.

Considering the easier case: two-photon absorption (TPA) causes transmission of light through a medium to be power dependent. The simultaneous absorption of two photons is a non-linear process that takes place with significant rates only at high optical intensity. For a single photon absorption, linear process, the absorbed intensity is directly proportional to the incident intensity:

$$I_{abs} = \alpha \cdot I_{inc} \quad (3.14)$$

with ‘ α ’ as linear coefficient of proportionality. While, for a two-photons process, the relationship between the absorbed intensity and the incident intensity is given by the equation (3.15):

$$I_{abs} = \alpha \cdot I_{inc} + \chi^{(2)} \cdot I_{inc}^2 = (\alpha + \chi^{(2)} \cdot I_{inc}) \cdot I_{inc} \quad (3.15)$$

The term $(\alpha + \chi^{(2)} \cdot I_{inc})$, which appears in the equation (3.15), can be re-defined, in analogy to the equation (3.14), as α' . TPA is more probable if the photon energy $h\nu$ is between: $\frac{1}{2}\Delta E < h\nu < \Delta E$ and in general for MPA the condition is expressed as in

(3.16):

$$\frac{1}{n}\Delta E < h\nu < \Delta E \quad (3.16)$$

where n is an integer that indicates the number of photons involved in the process. Differently from the TPA, where the relation between the absorption coefficient is linearly dependent to the optical intensity (equation (3.14)), for MPA the absorption coefficient is proportional to the $(n-1)^{th}$ power of the optical intensity, while the absorption rate is proportional to the n^{th} power of the optical intensity. It follows that the absorption rate is small at low or moderate optical intensity, but it becomes dominant for very high optical intensity.

The MP excitation of NV centers was recently demonstrated to be possible in the IR-range of wavelength by Peng Ji *et al.* [131]. This process of excitation of NV color centers is extremely advantageous for biological imaging, but also for quantum information processing, since the fluorescence signal is widely separated by the excitation one. In ref.[131] is showed how the number of photons involved in the MP transition associated to the NV⁰ centers, under high value of power, depends on the selected near-IR excitation wavelength. In ref.[131], three excitation wavelengths were selected, $\lambda_1 = 535 \text{ nm}$, $\lambda_2 = 1060 \text{ nm}$ and $\lambda_3 = 1210 \text{ nm}$, and for each selected wavelength a plot of the fluorescence emission intensity of the NV centers as a function of the power applied is reported. In particular, for the NV⁰ center, 1, 2 and 3 photons are involved in the excitation process at λ_1 , λ_2 and λ_3 , wavelength, respectively. In my study I used a 1038 nm excitation wavelength and the laser power ranged between few mW up to hundreds of mW , in order to observe the expected two photon transition by the NV⁰ centers. Furthermore, piezo-spectroscopic study was performed using IR excitation. Since the IR light can penetrate deeply into biological tissues with little scattering or damage [132], this study could be helpful to demonstrate the application of nanodiamonds for biological sensors of local stress.

3.4.1 Experimental results

The IR-PL spectroscopy and the piezo-spectroscopy were performed at the excitation wavelength of 1038 nm . The same fs -laser system, which was described in section

1.3 of the Chapter 1, has been used for these studies. The IR-excitation wavelength ($\lambda_{exc} = 1038 \text{ nm}$) is not enough in order to promote the electronic transition between the ground and excited state of the NV^0 defect with a single photon absorption, but this electronic transition can occur with the absorption of two or more photons. As already said, the MPA is a phenomenon which requires specific constraints and high power in order to occur. By applying high intensity *fs*-laser on nanodiamond samples, another non-linear effect can be induced in these samples: the generation of a super-continuum (SC) spectra. More details about this phenomenon are reported in ref.[133]. The probed diamond nanoneedle (Tip 4) was glued to the tungsten support tip by the FIB technique, using *Pt* deposition, as mentioned in the section 2.5.2 of Chapter 2.

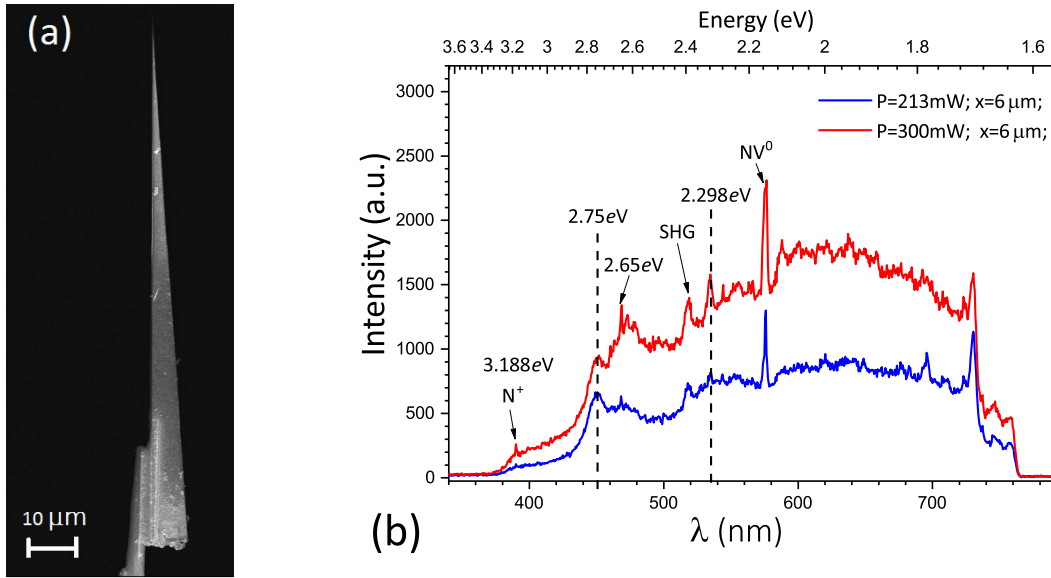


Figure 3.17: (a) Scanning electron microscopy image of the diamond (Tip 4), glued to the tungsten support tip by field ion microscopy technique. (b) The PL signals obtained on Tip 4, excited with the 1038 nm *fs*-laser at different values of laser power. The color centers at 389 nm , 468 nm and 575 nm are MP excited.

A SEM image of the analyzed diamond needle is reported in fig.3.17(a). The PL spectra, fig.3.17(b), are acquired at laser excitation power $P_{exc} > 200 \text{ mW}$. The MP excitation activates the electronic transition of three different color centers, that have already been detected in the PL wide spectrum acquired with the 260 nm laser. The

two peaks at 468 nm and 575 nm are respectively the 2.65 eV color center and the NV^0 center, while the signal peaked at $\sim 519\text{ nm}$ is the second harmonic generated (SHG) by the IR-laser wavelength (1038 nm). The color center peaked at 389 nm or 3.188 eV is a nitrogen (N^+) related center, which is well known in literature [77] and the two signals which appear peaked respectively at 450 nm or 2.75 eV and at $\sim 540\text{ nm}$ or 2.298 eV are peaks that are possibly related to some nitrogen-containing synthetic diamonds grown in the presence of Si and Ni, as reported in ref. [77].

In the next paragraphs, we focus mainly on the IR-analyses on the NV^0 center. The results are separated in three parts:

1. Dependency of the amplitude of the NV^0 on the illuminated position;
2. Piezo-spectroscopic study of the NV^0 center as a function of the V_{DC} applied bias;
3. Dependency of the amplitude of the NV^0 signal on the applied power.

3.4.1.1 Dependency of the NV^0 amplitude on the illumination position

As saw in section 3.2.2 of this Chapter, in order to study the effect of the V_{DC} bias in the PL spectra related to the NV^0 centers, the laser has to illuminate a region close to the apex of the diamond nanoneedle. Therefore, before to perform the piezo-spectroscopic analysis, at 1038 nm wavelength excitation, the study of the evolution of the amplitude of the NV^0 peak, as a function of the illumination position, was performed applying a fixed laser power of 450 mW . Each spectrum, in figure 3.18(a), was acquired at a different value of z that corresponds to the position where the impinging laser is focused with respect to the position of the tip apex: $z = 0\text{ }\mu\text{m}$. The negative values of z are related to positions along the shank of the tip, while the positive ones are related to positions outside the diamond needle. As reported in the plot in fig.3.18(b), the amplitude of the NV^0 center depends on the probed volume of the diamond tip, since it increases with the increasing of the probed volume. The two points at $-7.7\text{ }\mu\text{m}$ and $-6.6\text{ }\mu\text{m}$ show saturation effects, as visible in the spectra in figure 3.18(a). Since the impinging power was really high, the acquisition time of the spectra was kept below $\Delta t_{acquisition} < 10\text{ s}$, but, decreasing the $\Delta t_{acquisition} < 1\text{ s}$, the signal/noise ratio becomes too low. The

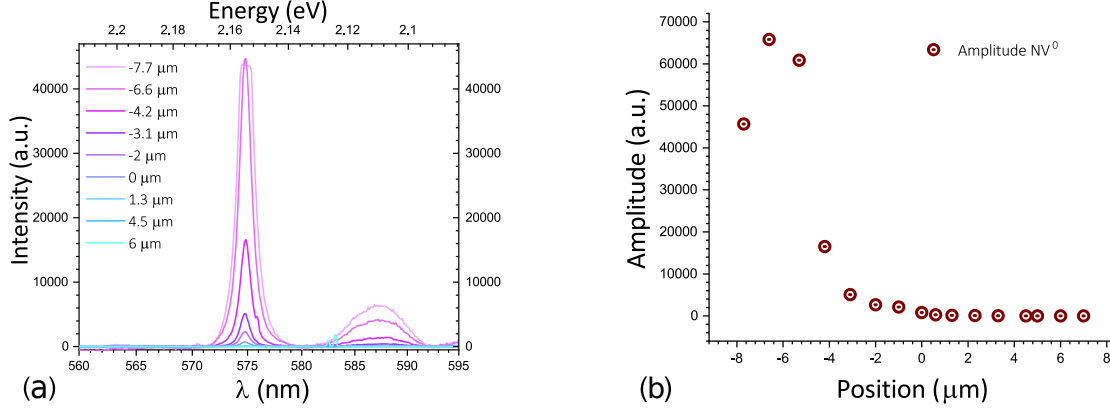


Figure 3.18: (a) μ -PL signal acquired with the IR-laser impinging at different positions with respect to the apex of the diamond Tip 4, at $P = 450$ mW, without bias and grating density 1200 *grooves/mm*. (b) The related plot where the amplitude of the NV^0 peak is reported as a function of the position, where the signal is acquired.

spectra in fig.3.18(a) were all recalculated for the same value of the acquisition time. From this first study, it is possible to conclude that increasing the integration time, at the same value of applied power, the range of positions $x = [-4; -2] \mu m$, corresponding to a distance $[2; 4] \mu m$ from the apex of the diamond tip could give an appreciable NV^0 signal in order to observe the effect of the V_{DC} bias acting on it.

3.4.1.2 Piezo-spectroscopic study of the NV^0 center as a function of the V_{DC} applied bias

Keeping the laser power fixed at $P = 450$ mW, it was chosen to perform the piezo-spectroscopic study on the NV^0 center focusing the IR-laser on the apex of the Tip 4, whose characteristics are reported in table 3.3.

needle specimen	apex radius R_{apex} (nm)	base radius R_{base} (μm)	length L (μm)
Tip 4	~ 62	~ 2	~ 94

Table 3.3: Geometrical parameters of the diamond Tip 4.

The IR-laser has a waist of $2\text{-}3\ \mu\text{m}$, so it cannot be perfectly focused on the apex of the tip, but this position has associated the uncertainty related to the size of the laser spot. The grating density used is the one with $1200\ \text{grooves}/\text{mm}$ in order to zoom on the restricted range of wavelengths around the NV^0 signal.

Looking at the spectra in fig.3.19(a), the NV^0 signal splits in two main components that, in agreement with the previous UV piezo-spectroscopic analysis and the literature [92], are labeled line *a* and line *b*, respectively, at high and low energies. Exactly as did for the UV analysis, through the equation(3.7) and the value of the coefficients $c_a = -4.5\text{meV}/\text{GPa}$ and $c_b = 3.3\text{meV}/\text{GPa}$, given by literature [92], it was possible to estimate the average value of the stress as a function of the selected value of the V_{DC} bias, at the position. The maximum average value reached for the stress, $\sigma_{average}(max) = (1.3 \pm 0.3)\ \text{GPa}$, corresponds to the max value of the applied V_{DC} bias ($14\ \text{kV}$).

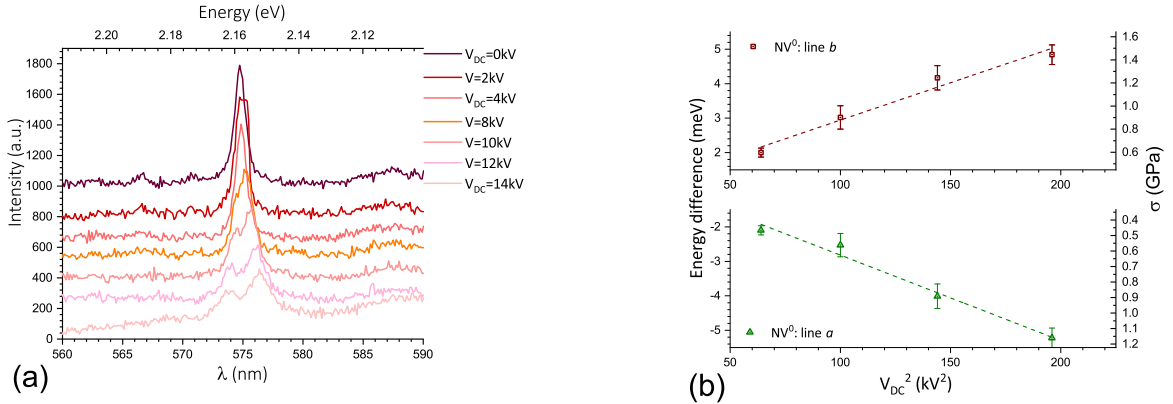


Figure 3.19: (a) μ -PL spectra acquired at different values of the V_{DC} bias, with the IR-laser impinging in a region close ($\sim 2 - 4\ \mu\text{m}$) to the apex of the diamond Tip 4, at $P = 450\ \text{mW}$ and grating density $1200\ \text{grooves}/\text{mm}$. In analogy with UV piezo-spectroscopic study, the plot, in fig.(b), reports the energy splitting of the NV^0 peaks, as a function of the different values of the V_{DC} bias and the related value of induced stress.

It follows that the NV^0 defect acts as an efficient stress-field sensor also when excited by IR-*fs*-laser, paving the way for interesting application of such color center as field-strain sensor for biological samples. The incertitude associated to the average stress

value is quite large in comparison to the UV measurements. The IR-laser spot has a larger diameter ($\sim 4 \mu m$) compared to the UV laser spot ($\sim 1.5 \mu m$) and, so, the measured average stress gives an higher value of the incertitude. By the piezo-spectroscopic study on the $2.65 eV$ color center, it was demonstrated that this color center shows higher strain sensitivity than the NV^0 center. Since its optical signature is detected also with the MP excitation in the IR wavelength, it follows that piezo-spectroscopy could be realized, for this defect, in the IR-excitation wavelengths. Further piezo-spectroscopic study with the IR-excitation laser could give access to other interesting informations about the $2.65 eV$ color center.

3.4.1.3 Dependency of the NV^0 signal as a function of the applied power

As mentionated in the equation (3.14) in the case of a MPA the absorption coefficient ' α ' depends on the $(n - 1)^{th}$ number of photons which participate to the MP process and that number figures out as the exponent of the optical intensity ' I ' or the applied laser power. If instead of considering the absorption coefficient ' α ', we consider the absorption rate ' R_{abs} ' of the optical emitter, then we have the following relation (3.17):

$$R_{abs} \propto A_{emitted} \propto \sum_{n=1}^{\infty} \chi^n P^n \quad (3.17)$$

In the equation (3.17), the optical intensity is replaced by the laser power ' P '. ' $A_{emitted}$ ' corresponds to the amplitude of the detected PL-signal and n indicates, as usual, the number of photons involved in the MPA. In summary, the relationship (3.17) affirms that the absorption rate is directly proportional to the intensity of the emitted signal and also to the n^{th} -power of the applied power. As already discussed, it follows that increasing the value of the power, an increasing of the MPA phenomenon is expected. The study of the amplitude of the NV^0 emitted signal as a function of the applied power was performed in order to know the number of photons which participate to the MP process. The measurements were performed in two different range of powers, the first time the power was varied within a range of high values $[40; 500] mW$, while the second time the study was performed within the range: $[2.5; 100] mW$, at low values

of power. In both situations the experiments were performed in a fixed position along the shank of the diamond needle, with the IR-exciting wavelength equal to 1038 nm and $V_{DC} = 0\text{ V}$. The first series of measurements was performed preliminarily on the the second harmonic (SHG) laser signal, in order to verify if the linear fit in $(\log\text{-}\log)$ scale, between the value of the amplitude of the SHG detected signal and the value of the applied power gave the expected value $n = 2$ of absorbed photons.

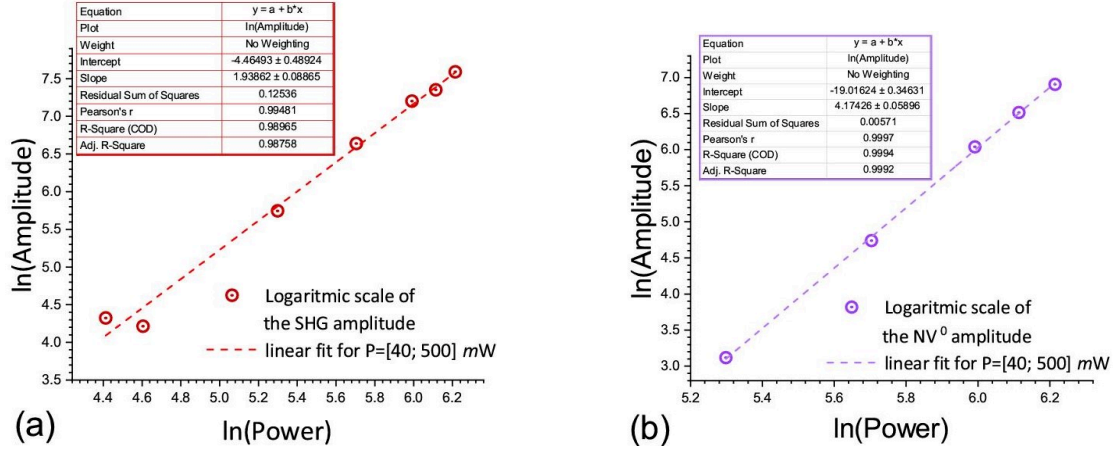


Figure 3.20: (a) Photo-emission amplitude of the second harmonic of the exciting laser (1038 nm) as a function of the exciting power, $P = [40; 500]\text{ mW}$ and in (b) the photo-emission amplitude of the NV^0 signal is plotted in the same range of power values. The values of the power and of the amplitude of the signal are reported in semilogarithmic scale. The dashed lines in both the plot correspond to the linear fit of the data and the related slope gave the number of photons involved in the MPA process.

The number of photons, involved in the generation of the SHG signal, is confirmed to be $n = 2$, as shown in fig.3.20(a). The fits on the SHG signal confirmed the results expected, so, the same method of analysis was used in order to fit the data collected by the PL signal of the NV^0 center as a function of the applied power, fig.3.20(b). But, differently by what was reported by Peng Ji *et al.* [131], the MP process was found to be a four photons process, instead of only two, for the NV^0 center.

For this reason, the measurements on the NV^0 center were repeated in a larger range of $P = [2.5; 107]\text{ mW}$, acquiring the NV^0 signal for more than ten different values of power. The related plot is reported in figure 3.21. The data don't show a unique trend.

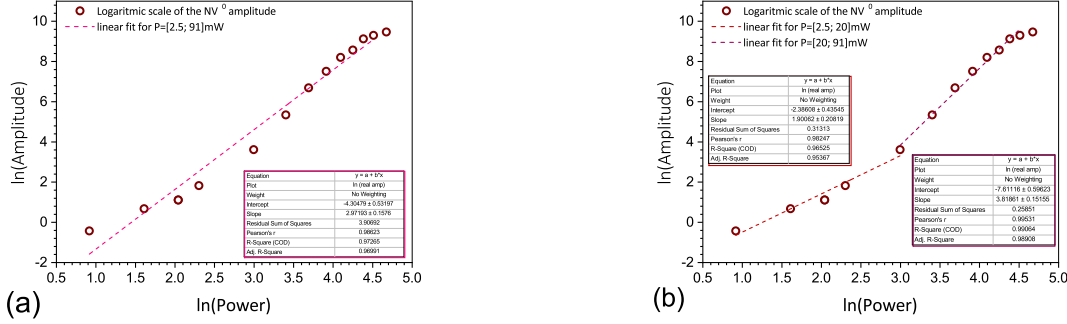


Figure 3.21: Photo-emission amplitude of the NV⁰ signal as a function of the exciting power. The values of the power and of the amplitude of the signal are reported in semilogarithmic scale. The dashed lines in both the plot correspond to the linear fit of the data and the related slope gave the number of photons involved in the MPA process. In (a) the fit of the data is performed in the power range $P = [2.5; 91] \text{ mW}$, with slope $n = 3$. In (b) the fit of the data is performed in two different ranges of power: $P_1 = [2.5; 20] \text{ mW}$ and $P_2 = [20; 91] \text{ mW}$, where respectively the slope of the fit is $n = 2$ and $n = 4$.

The data were fitted by a unique line in fig.3.21(a), while the data were fitted by two lines, in fig.3.21(b). In the first case (fig.3.21(a)) the slope of the fit results $n \approx 3$, which means that, in this case, three photons are involved in the MPA, anyway, this result is still not in good agreement with the literature [131]. In the second case, the fit was separated in two different ranges of values of power: $P_1 = [2.5; 20] \text{ mW}$ and $P_2 = [20; 91] \text{ mW}$ and the last data corresponding to the $P_{exc} = 107 \text{ mW}$ was discarded, since the corresponding signal was saturated. The fit in the first range of powers gives a slope equal to two, which means a TPA for the emission of the NV⁰ signal until $P_{exc} = 20 \text{ mW}$. While within the range of values $P_2 = [20; 91] \text{ mW}$, the slope of the fit gave a slope equal to four, which corresponds to the MPA of four photons.

From the present study about the NV⁰ PL-signal power dependency, it seems that the NV⁰ MPA does not depend only by the exciting wavelength, as reported in ref. [131], but also by the intensity of the exciting laser power. The MPA transitates from a two photons to a four photons absorption process, at high excitation power.

Chapter 4

Structural and optical properties of ZnO/MgZnO heterostructures

4.1 Introduction

Wide bandgap semiconductors risen in the recent years, increasing the production of high-power and high-frequency electronic devices (*e.g.* lasers and diodes).

The successful progress of this class of materials has come to the forefront thanks to the parallel improvement of the growth techniques, which allow to reach a better control on the growth parameters and then on the high quality of the grown materials.

One material whose research and study was largely boosted and expanded in the last 20 years is the zinc oxide (ZnO). Indeed, ZnO can now be grown, as bulk crystal, thin film and also as nanostructure, with a variety of techniques [134]. Among them, the Molecular Beam Epitaxy (MBE) leads to the availability of large area single bulk crystals and also high quality of thin films, with reduced concentration of extended defects. The open issue in the growth of bulk crystals and thin films is the need to employ a material with a lattice substrate which causes limited number of lattice defects in the grown one, due to the lattice mismatch related to the two materials, which can be exacerbated by their competing thermal expansion mismatch. In order to overcome the substrate problem a possible solution is the use of low scale systems materials, likes nanostructures

[134, 135]. The nanoscale systems can be strain free, offering more flexibility in strain engineering and also present efficient carrier confinement [135], in the case of quantum confined systems. In this chapter the quantum well, grown in a heterostructure of ZnO/MgZnO materials will be discussed in detail. In general, thanks to their peculiar characteristics (*e.g.* geometry, electronic distribution and surface/volume ratio), quantum confined systems are advantageous in order to enhance the opto-electronic performances of the new devices, as in the case of LEDs, and they can also find good applications as sensors [136, 137]. The rising importance of this low scale technology asks to pay particular attention also to the development of techniques able to probe with high spatial resolution the crystalline structure of these materials and also their physical properties.

In this chapter the main optical properties of quantum well heterostructures of ZnO/MgZnO, are linked to the crystalline structure of the analyzed material thanks to the recent experimental developments on correlative laser-assisted atom probe tomography and optical spectroscopy “*in-situ*” [138, 57]. The system, named “ μ -PL/La-APT”, has the advantages to determine the average alloy composition, compositional fluctuations in three dimensions, with sub-nanometer spatial resolution and the optical signature of the sample, during the experiment. The nano-specimen has to be a nanoscale volume of a sharp material tip (as seen in Chapter 1) and the 3D virtual reconstruction of the sample is performed through the elaboration of the collected data, in order to access to the constituent chemical species, size and shape of it and to correlate these features with the optical transitions characteristic of the studied system. The optical transitions of one material is the fingerprint of the distribution of its electronic states which are influenced by the structure of the material itself. It follows that probing a nanostructure through the μ -PL/La-APT setup the structural and physical properties (*e.g.* electronic, optical, mechanical, thermal) of the probed specimen can be outlined in only one experience.

4.1.1 ZnO/MgZnO heterostructures

The performances of semiconductors received a significant increase with the advent of quantum confined 2D systems, called quantum wells (QWs), heterostructures and, in general, over the past decades, through the developing of nanostructures and new materials. Here we focus on the physics of heterostructures, which are systems composed by different materials (at least two), where the geometry of the interfaces between the two materials can be complicated, as a function of the properties of the materials which compose the heterostructure [62]. The properties of charge carriers in layers of an heterostructure can be different from those of bulk materials, presenting: *e.g.* extremely high mobility, high radiative recombination efficiency or novel states of matter [62]. For this reason particular attention is dedicated to the growth method of these systems [139, 62, 140]. The simplest case is a planar interface between the two materials, *i.e.* in a layered system. In particular, heterostructures based on II-VI semiconductors can be obtained combining the physical properties of binary compounds and ternary alloy semiconductors composed by group II elements (*e.i.* Zn, Cd, Be, Mg) with group VI elements (*e.i.* O, S, Se, Te).

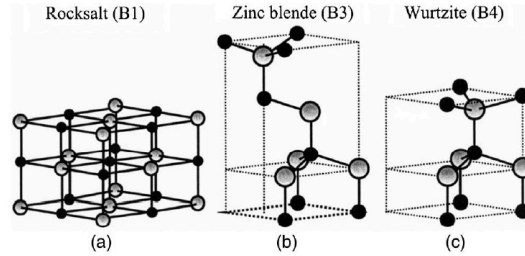


Figure 4.1: (a) Rocksalt, (b) zinc blende and (c) wurtzite structures. (*black spheres: O atoms, grey spheres: Zn atoms*) [141].

Most of the group II-VI binary compound semiconductors crystallize in either rock-salt or zinc blende or hexagonal wurtzite (wz) structure, which are showed in fig.4.1, where each anion is surrounded by four cations at the corners of a tetrahedron, and vice versa. The tetrahedral coordination is typical of sp^3 covalent bonding, but these materials also have a substantial ionic character that tends to increase the bandgap beyond

the one expected from the covalent bonding. ZnO is a II-VI compound semiconductor whose ionicity resides at the borderline between the covalent and ionic semiconductors. ZnO can assume either the wurtzite structure or the zinc blende or the rocksalt crystal structure, as a function of the different conditions (T, p) at which it is exposed. Under ambient conditions the thermodynamically stable phase is that of wurtzite. The zinc blende ZnO structure can be stabilized growing ZnO on cubic substrate, while the rocksalt phase of ZnO is obtained only at relatively high pressures. Here we report about the wz ZnO structure which has a hexagonal unit cell, fig.4.2, with two lattice parameters a and c , in the ratio $\frac{c}{a} = \sqrt{\frac{8}{3}} = 1.633$ (in an ideal wurtzite structure), and it belongs to the space group C_{6v}^4 in the Schonflies notation. The group C_{6v}^4 preserves the symmetry of the crystal including rotations by: $\pm 60^\circ$, $\pm 120^\circ$ and $\pm 180^\circ$ around the hexagonal axis. The basal plane lattice parameter (edge length of the basal plane hexagon) is universally depicted by a ; the axial lattice parameter (unit cell height), perpendicular to the basal plane, is universally denoted as c , as shown in fig.4.2.

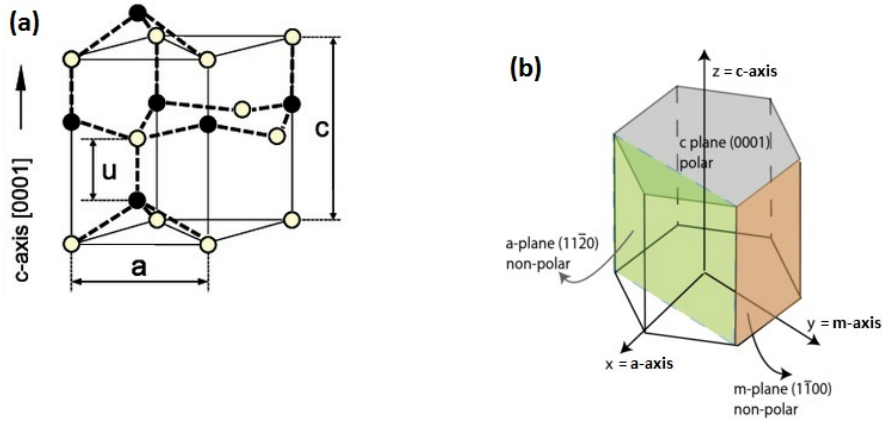


Figure 4.2: (a) Unit cell of the wurtzite structure, the two lattice parameters a and c and the u cell-internal parameter are indicated: *yellow spheres are referred to **Zn** atoms and black spheres to **O** atoms*. (b) Another conventional unit cell representation of the *ZnO* bulk material including the definition of the most relevant low-index crystal-surface planes. The polar *c-plane* and the two nonpolar *m*– and *a-planes* are shown in blue, red, and green, respectively.

The structure is obtained interpenetrating two hexagonal close-packed (*hcp*) sublattices (fig.4.2), each of which consists of one type of atom displaced with respect to each other along the threefold *c-axis* by the amount of a quantity labeled as $u = \frac{3}{8} = 0.375$ and called cell-internal parameter [141]. Each sublattice includes four ions per unit cell, every ion of one kind (group II, *e.i.* Zn) is surrounded by four ions of other kind (group VI, *e.i.* O) or vice versa, the ions are coordinated at the edges of a tetrahedron. In real ZnO crystal, the wurtzite structure deviates from the ideal arrangement, by changing the $\frac{c}{a}$ ratio and so the value of the lattice parameters a and c . These parameters don't deviate drastically from the theoretical value, but their ratio, $\frac{c}{a}$, is included within the range [1.593; 1.6035] [141] and the deviation from that of the ideal wurtzite crystal is probably related to lattice stability and ionicity [141]. Between the $\frac{c}{a}$ ratio and the u parameter a strong correlation exists, indeed when the $\frac{c}{a}$ ratio decrease, the u parameter increases in order to let four tetrahedral distances remain nearly constant through a distortion of tetrahedral angles. The difference between the the real value of $u = [0.383; 0.3856]$ [141] and the ideal value $u_{ideal} = 0.375$ is defined as $\epsilon_1 = u - u_{ideal}$. The ϵ_1 quantity was found to significantly affect the spontaneous polarization, P_{spont} , along the *c-axis*, in the wurtzite structure [62]. The origin of this kind of polarization in the wurtzite crystal structure is the intrinsic asymmetry in the relative arrangement of the Zn and O ions along the *c-axis*, [0001] direction. For that reason, the *c-axis* is called “polar direction”, while the *a-axis*, [11 $\bar{2}$ 0] direction, and *m-axis*, [1 $\bar{1}$ 00] direction, are non-polar axes [134], fig. 4.2.

The spontaneous polarization of ZnO cannot be directly measured [142], however when mechanical stress is applied on the surface of the wurtzite structure, the piezoelectric reponse of the material gives rise to the piezoelectric polarization reponse, P_{piezo} . The total effect of the contribution of the induced and the spontaneous piezoelectric polarization can then be measured and the total polarization P_{tot} is defined in equation (4.1):

$$P_{tot} = P_{spont} + P_{piezo} \quad (4.1)$$

The properties of band structure are determined by the symmetric properties of the semiconductor crystal and chemical binding of constituting elements. Based on the

atomic orbitals, the conduction band E_C is mainly constituted by first unoccupied s -levels or antibinding states, which derives usually from the cations, such as the $4s$ levels of Zn in ZnO . The corresponding valence bands E_V are formed by the highest unoccupied levels, which are p -levels or binding states, such as $2p$ -levels for the O in ZnO . The band structure of ZnO near the Γ of the Brillouin zone is depicted in fig.4.3, where the band structure $E(k)$ is expressed as a function of the k quasi-momentum. As shown in figure 4.3 (b), at Γ , three degenerate valence bands, E_V , coexist and by uniaxial crystal field of hexagonal wz crystal structure and by spin-orbit coupling, they are splitted in: *heavy holes* (hh), *light hole* (lh) and *split-off holes* ($s-o$) states. These electronic states are also labeled, in literature [62]: “A-band”, “B-band” and “C-band”, as in fig.4.3(b), from higher to lower energies. Since ZnO is a direct bandgap semiconductor, the energy difference between the bottom of the conduction band, E_C , and the top of the *heavy hole* state at the Γ point is the material bandgap.

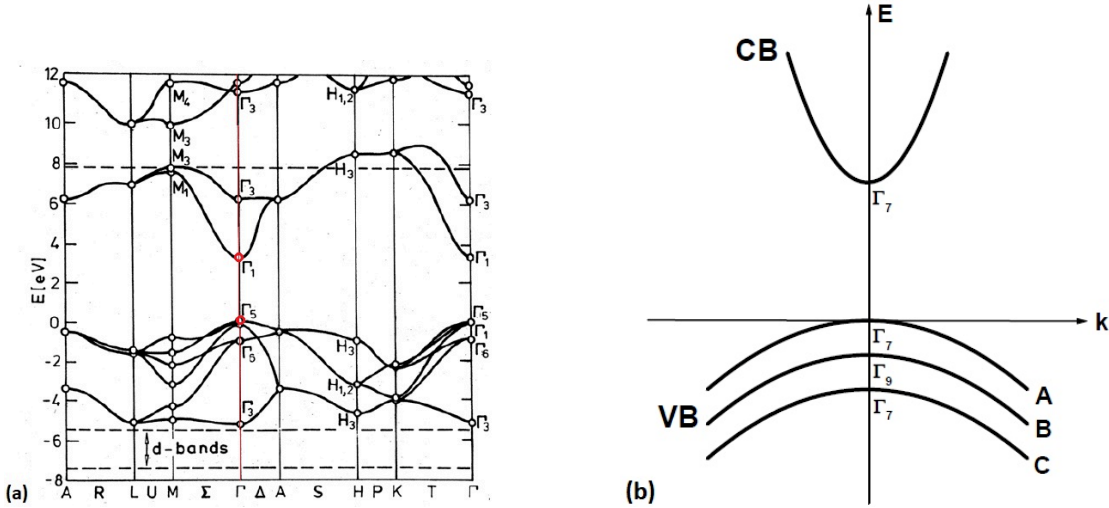


Figure 4.3: (a) Band structure of ZnO in wurtzite structure, calculated using the HSE hybrid functional [134]. The energy of the valence-band maximum (VBM) was set to zero. As a direct bandgap material, the bandgap of ZnO is calculated along the Γ direction of the Brillouin zone. (b) Simplified band structure with conduction band and three valence bands of ZnO . Zoom in a surrounding of the Γ point in the Brillouin zone depicted on the left (a).

As said above, the electronic band structure of a semiconductor depends on its chemical composition and on its crystalline structure. This means that, for example, polytypes with identical composition, but different crystal structure, have different energy gap. It also means that the bandgap can be continuously tuned by controlling the chemical composition of binary, ternary or quaternary alloys during the synthesis of the material. Modern heterostructures are often systems based on the alternated growth of binary compounds and ternary alloys. In order to avoid to grow heterostructures with extended defects, the lattice mismatch and the crystal quality of the single components has to be taken into account.

Comparing the size of the bandgap between II-VI semiconductors, as reported in fig.4.4, at ambient conditions, in wz crystal structure, ZnO presents wide direct bandgap energy $E_{gap} = 3.4 \text{ eV}$ and large exciton binding energy $E_{exc} = 60 \text{ meV}$; these characteristics allow to use this semiconductor as an active (emitting) element in optoelectronic, which provides ultraviolet (390 nm) excitonic laser action upon optical pumping at room temperature. As reported in ref. [134], over the past decades, a significant improvement in the quality of ZnO single-crystal substrates and epitaxial films was achieved and the epitaxy of ZnO films on native substrates can result in ZnO layers with reduced concentration of extended defects and, so, better performance in electronic and photonic devices [143]. Thanks to the improvements achieved in the epitaxial growth techniques, heterostructures containing ZnO alternated to a different material can be grown. The most important parameters to be checked for a heterostructure are:

- the lattice mismatch between the two grown materials;
- the bandgap of each layer and the valence and conduction bands band offset between individual layers.

Bandgap engineering in ZnO can be achieved by alloying with MgO and/or CdO. By the way the MgO and CdO assume the rock-salt structure, not the same crystal structure of ZnO (wz) and this can generate a big issue for ZnO-based alloys with high content of MgO and CdO. With a moderate content of MgO and/or CdO in the ZnO wz structure, the MgZnO and CdZnO alloys assume the wz crystal structure of the parent compound, still providing a wide range of bandgaps : $[3.2; 4.1] \text{ eV}$ [134]. The ternary alloy can be

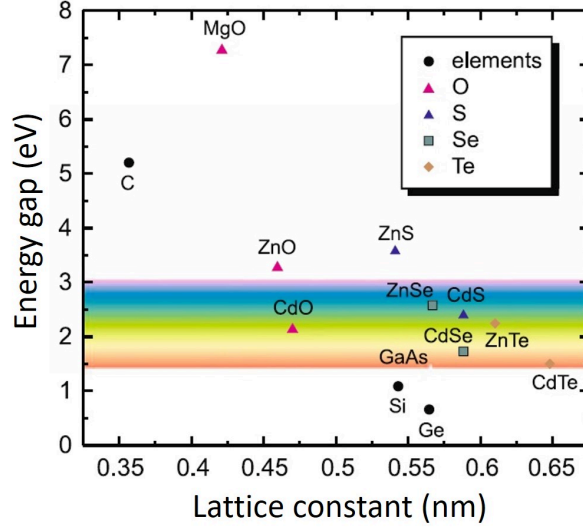


Figure 4.4: Bandgaps as a function of the lattice constant for various elements of the II-VI groups. The lattice constant of wurtzite semiconductors was recalculated for a cubic cell.

generally depicted with the following notation: $A_xB_{1-x}C$, where ‘ x ’ represents the fraction of substitutional atoms in the cation sublattice. In this notation, C represents an element of the VI group and A and B are elements of the II group, in this case: A corresponds to Mg or Cd, B corresponds to Zn and C corresponds to O. On the x parameter depends the energy bandgap and the fraction of the binary components Mg or Cd and ZnO in the ternary alloy, so it is an important parameter. Alloying ZnO with CdO leads to a reduction of ZnO bandgap, while an opposite behavior comes alloying ZnO with MgO, increasing the bandgap. Focusing on $Mg_xZn_{1-x}O$, this alloy has the hexagonal wz-structure for Mg concentration up to $x = 0.33$ and a cubic transition has been observed for Mg concentrations higher than $x > 0.45$ [144]. A two phase structure is observed for intermediate concentrations [145]. The bandgap of $Mg_{0.33}Zn_{0.67}O$ alloy increases until $E_{gap} = 3.99 \text{ eV}$ and in comparison to ZnO, an increasing in the exciton binding energy has been observed for MgZnO alloys [145]. In 2011, the growth of high quality of $Mg_xZn_{1-x}O$ films, with Mg concentration higher than 0.5, in wz structure, was reported [146], allowing to tune the energy bandgap in a wider range. The linear

relationship between bandgap and Mg-II site fraction was established, for the hexagonal phase [147], to be (eq.4.2):

$$E_{gap}(Mg_xZn_{1-x}O) = E_{gap}(ZnO) + b \cdot x \quad (4.2)$$

where $b = 2 \text{ eV}$. The Mg-II site fraction also changes the wz-lattice constants, indeed as the Mg concentration increases as the lattice parameter a increases and c decreases [148]. In figure 4.5(a) is plotted the relationship between the values of the a and c lattice parameters and the Mg concentration in $Mg_xZn_{1-x}O$, while in figure 4.5(b) is plotted the dependence of the energy bandgap of the $Mg_xZn_{1-x}O$ alloy on the Mg concentration, in the case of wz crystal structure and also for the rocksalt crystal structure.

In table 4.1, the main structural and optical properties of the ZnO , MgO and

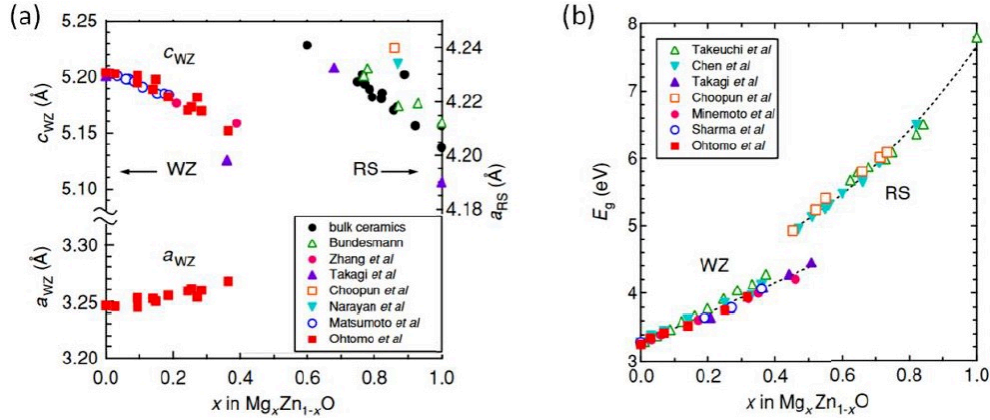


Figure 4.5: (a) Dependence of the a-lattice and c-lattice parameters and of (b) the bandgap on the Mg II-site fraction y (images readapted from ref. [145])

$Mg_xZn_{1-x}O$ are summarized and can be compared.

4.1.1.1 Band alignment in $ZnO/MgZnO$ heterostructures

Heterostructures based on $ZnO/Mg_xZn_{1-x}O$ are currently employed in the developing of systems and devices based on quantum confined effects and on interband or intersub-band transitions, as it will be explain in the section 4.1.2. Before to treat the optical

	<i>ZnO</i>	<i>MgO</i>	<i>Mg_xZn_{1-x}O</i>
$E_{gap}(eV)$	3.4	7.8	$3.37+2\cdot x$ [149]
a (nm)	3.2	4.2	$3.25+0.036\cdot x$ [149]
c (nm)	5.2	...	$3.34-0.063\cdot x$ [148]
stable crystal structure	<i>wurtzite</i>	<i>rocksalt</i>	$x \leq 0.33$ or $x < 0.5$ <i>wurtzite</i> [147] $0.33 < x < 0.45$ <i>rocksalt</i> [147]

Table 4.1: Main structural and optical characteristics of *ZnO*, *MgO* and *Mg_xZn_{1-x}O* at $T = 300\text{ K}$

properties of inside the quantum well (QW) or multi quantum well (MQW) system, it is important to visualize how the bandgaps of the *ZnO* and *MgZnO* are aligned at the heterojunctions between the two materials or properly inside the heterostructure.

As known, *ZnO* and *Mg_xZn_{1-x}O* are semiconductors with different bandgaps, which are grown in an ordered hierarchical way, alternating layers of one material with the second one. The two materials might have not only different bandgaps, but also different thickness: the thinner semiconductor, if it has thickness below the value of the “*de Broglie wavelength*” ($\lambda_{de\ B} \approx 10\text{ nm}$) and it has the lower bandgap value, constitutes the QW, while the thicker semiconductor, if it has thickness above 10 nm and the bandgap has the wider value, is called barrier of the QW. The relative position of the conduction and valence band, between the two semiconductors, (band alignment) is determined through the electron affinities χ , as depicted in fig.4.6.

The semiconductor electron affinity is the (positive) energy difference between the vacuum level and the conduction band edge. as a function of the different type of bands alignment, two kind of heterostructures are distinguished: type-I and type-II heterostructures. In the type-I structure, the lower conduction-band edge and the higher valence-band edge are both in the material with smaller band gap. In this way, electrons and holes localize there. In type II structure, a staggered lineup is present and electrons and holes localize respectively in the different materials. In the case of MQWs systems of *ZnO/Mg_xZn_{1-x}O*, we are considering a heterostructure of type I. At ambient conditions (p, T) and as wurtzite crystal structure, *ZnO* has a bandgap equal

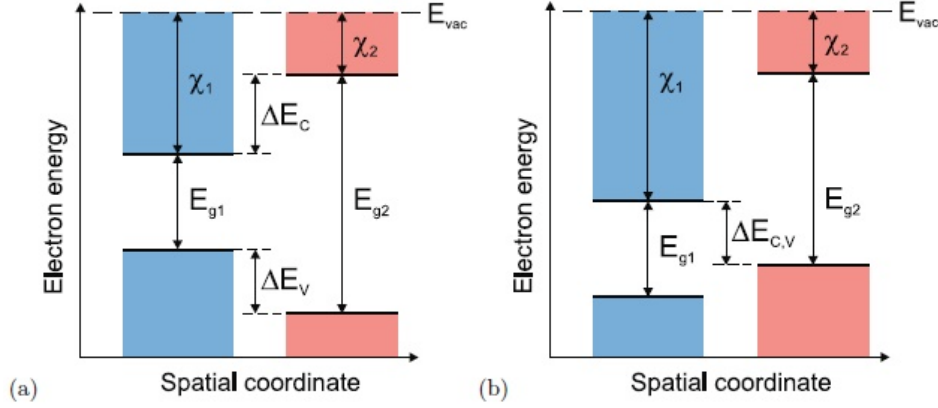


Figure 4.6: Position of band edges (band alignment) in (a) type-I and (b) type-II heterostructure.

to 3.37 eV , while the $Mg_xZn_{1-x}O$ bandgap varies as a function of the x concentration of Mg, as reported in the plot in fig.4.5(b). The bandgap of $Mg_xZn_{1-x}O$ as a function of x was observed to vary within the range: $[3.37; 3.99]\text{ eV}$, where the bandgap increasing up to 3.99 eV is observed for $Mg_xZn_{1-x}O$ wurtzitic structure for Mg concentration $x = 0.33$ [134]. The ZnO layers act as QWs and the layers of $Mg_xZn_{1-x}O$ as barriers of the QWs, appropriately tuning the growth conditions of the heterostructure. Unfortunately, as wurtzite layers, $ZnO/Mg_xZn_{1-x}O$ heterostructures exhibit built-in electric fields along the c -axis [0001] and this characteristic inevitably affects the electronic properties. So, in order to avoid this kind of limitation one strategy could be to grow the wurtzitic $ZnO/Mg_xZn_{1-x}O$ heterostructure using the non-polar a -axis or m -axis direction of growth. One important condition to tune in order to take advantage on the choice of the non-polar direction of growth is to precisely control the strain state of the $Mg_xZn_{1-x}O$ barrier, as a function of its layer thickness and x Mg concentration [150, 151], because the effect of the residual strain in non-polar layers of ZnO QWs is reflected on the QWs band structure, as explained by Chauveau *et al.* [150]. In particular, the (Mg,Zn)O samples investigated by Chauveau *et al.* [150], grown along nonpolar a -(11 $\bar{2}$ 0) or m -(1 $\bar{1}$ 00) directions by metal organic chemical vapor deposition (MOCVD), showed an evolution of the in-plane lattice parameter along the c - and m -directions until Mg concentration $x_{Mg} \approx 25\%$ and then the in-plane c -lattice parameter stabilizes. The

evolution of the c - and m - lattice parameters, for increasing x_{Mg} concentrations ($0 < x_{Mg} < 0.25$), has an anisotropic trend. Such anisotropy of lattice parameters generates:

- tensile strain, along the m -axis $[1\bar{1}00]$;
- compressive strain, along the c -axis $[0001]$.

This strain has an effect on the QWs that corresponds to a strong blueshift of the excitonic levels, which gives rise to a blue-shift effect in the QW-PLE signal, in agreement with the theory of the quantum well confinement and localization effects.

4.1.2 Carriers distribution inside the ZnO quantum wells

A QW is a thin flat layer of a semiconductor (typically below the size of the “*de Broglie wavelength*”) , that is grown between two thicker layers of different semiconductors, which constitute the barriers of the QW. In figure 4.7 is represented the electronic distribution in the conduction and valence bands at the heterojunction between a QW and the barriers related to a heterostructure of type I, like $ZnO/Mg_xZn_{1-x}O$, where $E_{gap,barr} > E_{gap,QW}$.

As we can observe in fig.4.7, carriers in a quantum well are confined only on the growth direction, z -axis, but they can freely move along the quantum well plane (x, y) . The carriers thus possess in-plane energy levels which depend on their in-plane wave vector \mathbf{k} and they are distributed in 2D bands. Neglecting the lattice periodic wave function, the total carrier envelope function is the product between the confined wave function $\psi_{n(e,h)}(z)$ and a plane wave $exp(i\mathbf{k}\cdot\mathbf{r})$, with $\mathbf{r}=(x,y)$. The Schrödinger equation of the system (eq.4.3), where $r = (x, y, z)$, can be splitted and solved separately for the in-plane and the on-axis components.

$$\frac{\hbar^2}{2m} \cdot \frac{d^2\psi(r)}{dr^2} + (E + V(r)) \cdot \psi(r) = 0 \quad (4.3)$$

The on-axis (z) solution yields a set of discrete levels, called subbands. The subband energy can first be estimated by approximating the barriers as infinitely high. In this ideal case, the energy $E_{n(e,h)}$ of the electron/hole subbands can be indexed as follows

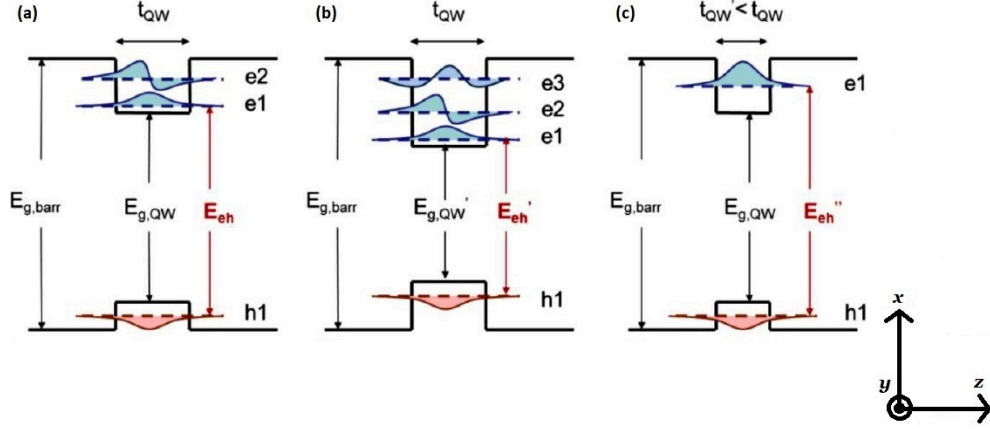


Figure 4.7: (a) Confined electron and hole energies and wave functions (sub-bands) within a rectangular quantum well of a given composition and thickness. Parts (b) and (c) show how the energy of the states and of the main radiative recombination evolves with quantum well composition and thickness, respectively.

(eq.4.4):

$$E_{n(e,h)} = \frac{\hbar^2 \pi^2 n^2}{m_{e,h}^* t_{QW}^2} \quad n = 1, 2, 3... \quad (4.4)$$

while the wave functions $\psi_{n(e,h)}(z)$ are completely confined within the quantum well and are given by the relation (4.5):

$$\psi_{n(e,h)}(z) = A_z \sin\left(\frac{\pi n z}{t_{QW}}\right) \quad (4.5)$$

where A_n is the normalization constant satisfying the condition that integral of the squared wave function over z is equal to unity. In the (eq.4.4), $m_{e,h}^*$ is the electron (hole) effective mass, which represents the electron mass of an electron inside of a crystal, where the electron interacts with the crystal fields. The electron (hole) effective mass differs from the mass of a free electron, of the classical equation: $E = \frac{p^2}{2m}$, but it allows to treat the electrons (holes) inside of a crystal as if they are free, for some k

values. The $m_{e,h}^*$ electron (hole) effective mass is defined in the equation (4.6).

$$m_{e,h}^* = \left(\frac{1}{\hbar^2} \frac{\partial^2 E}{\partial k^2} \right)^{-1} \quad (4.6)$$

As we can read in the equation (4.6), the $m_{e,h}^*$ electron (hole) effective mass results proportional to the slope of the energy band where the electron can move, so it depends on the QW composition.

One of the main effects of the quantum confinement is that the electron and hole ground states do not lie at the bottom of the conduction or valence bands characteristic of the QW phase, but are lifted of a certain amount, fig.4.7, which is called the *confinement energy* $E_1(e, h)$. As illustrated in fig.4.7(b) and (c), the electronic wave function becomes progressively less confined with decrease of barrier gap. Furthermore, a finite number of subbands can be accommodated in a QW with finite barrier height. The main optical emission taking place within a quantum well involves the electron and hole “ground states” ($n = 1$). The emission energy is given from (4.7):

$$E_{e,h} = E_{1e} + E_{1h} + E_{g,QW} \quad (4.7)$$

The terms which appear in the equation (4.7) all depend on the barrier composition and on the quantum well thickness t_{QW} . In the equation 4.7, the E_{ex}^1 term is omitted and this term, which labels the *exciton binding energy*, will be discussed in the next section more in detail. Looking at the pictures 4.7(b) and (c) and the equation (4.7) is clear that the QW *confinement energy* spacing becomes large for narrow wells (small t_W) and small effective mass $m_{e,h}^*$, while it reduces increasing the well thickness and effective mass. Real quantum wells are more complex than the basic description and representation given here. For instance, in real QWs, the finiteness of the barrier energy gaps yields an evanescent but non-zero wave function within the barriers and a decrease of the subband energy E_n . Alloy clustering within the quantum wells may occur and defects can be present as well. But, since the QWs size is usually less than 10 nm, the critical thickness to form dislocations in non-lattice matched epitaxial layers is never reached. This allows the growth of high quality non lattice-matched materials.

Alternating QWs with barriers leads to the formation of MQWs. The physics of MQWs is essentially the same as a set of single QWs. However, if the barriers are too thin, the wavefunctions associated to the confined states penetrates in adjacent QWs which form a periodic system called superlattice.

Another interesting consideration to do is about the effect of external or internal fields acting on the electronic states within a QW. For instance, QWs grown along a crystal direction with no inversion symmetry, as the in the case of wz crystal, exhibit polar properties leading to the Quantum Confined Stark Effect (QCSE). In that case, a spontaneous polarization develops and such polarization has opposite direction for the different heterostructure phases, a static sheet charge builds up at heterointerfaces. This spontaneous polarization is known also as pyroelectric effect and the sign of the charge depends on: the polarization values of the ZnO and $Mg_xZn_{1-x}O$, which compose the interface, and whether the ZnO is before or after the $Mg_xZn_{1-x}O$ along the polar direction.

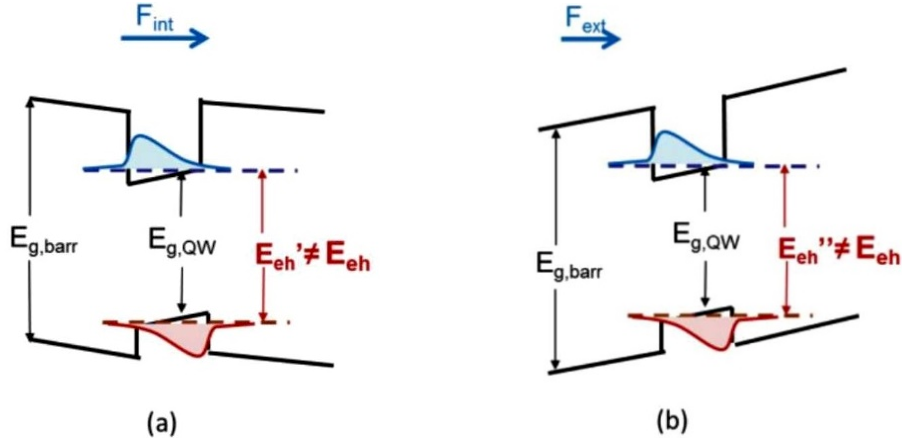


Figure 4.8: (a) Confined electron and hole energies and wave functions (sub-bands) within a rectangular quantum well exhibiting the buildup of an internal field (the term $E_{e,h}$ refers to a zero-field system). (b) Confined electron and hole energies and wave functions (sub-bands) within a rectangular quantum well across which an external field is applied.

Furthermore, along the growth direction each heterostructure phase is coherently strained on another and such strain may set up a further polarization, which increases

the concentration of carriers at the interfaces, as consequence of the piezoelectric effect. These carriers confinement translates into the presence of an electric field within the QW structure or, better, as an electric field discontinuity across the heterointerface, as shown in figure 4.8(a).

The effect of this internal electric field, shown in fig.4.8(a), which acts on the electronic states of the QW translates in shifts of the radiative recombination energy and intensity. The modification to the energy levels also depends on the thickness of the quantum well structure. If we consider the non-polar directions, which are the *a*-axis and *m*-axis in the wurtzite crystal, the QCSE is present only if an external electric field is acting on the quantum confined system. The potential profile at the heterointerface and the confined electron and hole wavefunctions are modified as effect of the electric field acting on them. Indeed, the electric field reduces the electron and hole energies with respect to the flat-band case and it spatially separates the wave functions of electron and hole. Differently from the effect of an internal electric field, comparing figures 4.8(a) and (b), it is clear that an external electric field tilts the valence and conduction bands of the barriers and QWs along the same direction, fig.4.8(b), reducing the electron-hole wavefunctions overlap, affecting also the optical properties of the system. Wurtzitic heterostructures of $ZnO/Mg_xZn_{1-x}O$, grown along the *c*-axis, due to the polarization presents along this crystallographic orientation, they have a built-in electric field that affects inevitably the optical/electronic properties of the system. Using the non-polar $a - [11\bar{2}0]$ or $m - [1\bar{1}00]$ surfaces of growth can avoid this limitation. In such case, in order to take advantage of non-polar heterostructures, it is a prerequisite to control precisely the strain state of the $Mg_xZn_{1-x}O$ barrier and the residual strain acting on non-polar ZnO QWs, as explained in the article [150].

4.1.2.1 Excitons

In the ideal case, at $T = 0\text{ K}$, the ground state of a semiconductor is depicted by the filled valence band E_V and the empty conduction band E_C . The absorption of a photon causes the transition of an electron in the conduction band and leaves a hole in the valence band.

If the characteristic thermal energy ($k_B T$) is sufficiently low, taking in account the effective mass $m_{e,h}^*$ model, the pair of excited electron and hole interacts each other through Coulomb field and form an hydrogen-like state called *exciton*. This bound state, *exciton*, induced by the attractive potential is characterized by an energy (4.8):

$$E_{ex}^n = -\frac{R_y^*}{n^2} + \frac{\hbar^2 k^2}{2M} \quad \text{with : } M = m_e + m_h \quad (4.8)$$

R_y^* is called Rydberg energy and it is defined as: $R_y^* = 13.6 \frac{\mu}{m_o \cdot \epsilon^2}$ (eV) and $\mu = \frac{m_e \cdot m_h}{m_e + m_h}$. The radius of the *exciton* is given by the equation (4.9):

$$r_{ex}^n = n^2 \frac{m_e^*}{\mu} \epsilon_r a_B \quad (4.9)$$

where $a_B = 0.53 \text{ nm}$ denotes the hydrogen Bohr radius and for the *exciton* the parallel one is r_{ex}^1 .

Two main categories of *excitons* can be distinguished:

- *free excitons*: if the *excitons* can move freely inside the semiconductor;
- *bound excitons*: if the *excitons* are associated with point defects of the semiconductor.

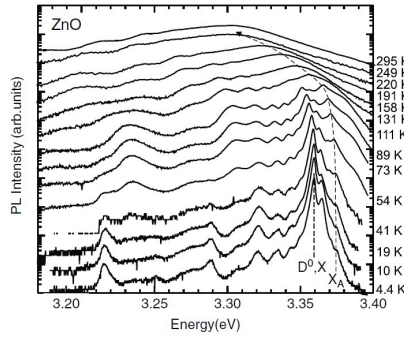


Figure 4.9: Temperature-dependent luminescence spectra of *ZnO* thin film. At low temperatures, the PL signal is dominated by donor-bound exciton transitions. The curved dashed line visualizes the energy position of the free-exciton transition (X_A), that becomes dominant at room temperature.

Excitons play an important role in optical properties of semiconductors, especially at low temperature, where the *exciton* recombination is the main mechanism for the light emission. Particular is the case of ZnO, where the recombination from *free-excitons* is observed even at room temperature, as shown in figure 4.9. This phenomenon will be explained better in the next section 4.1.3.

When the characteristic thermal energy ($k_B T$) of a semiconductor increases, the *exciton* interaction is replaced by the electron-hole recombination.

In QWs, the *exciton* radius eq.(4.9) is lower than in bulk materials, at least in the direction perpendicular to the QW, so the *exciton* binding energy may increase up to 4 times as large as the bulk value. Furthermore, the ZnO excitonic binding energy (60 meV) can be increased up to 120 meV in the ZnO/MgZnO MQs, due to quantum confinement effects [140].

4.1.3 Carrier localization and radiative recombination in ZnO/MgZnO heterostructures

As previously seen, the energy bands of a semiconductor system (*e.g.* binary compound, alloy, heterostructure..) are determined by its crystal structure and chemical binding of the constituting elements. Some structural features (*e.g.* alloy disorder, defects, dislocations...) and compositional fluctuations at the layer interface, in a heterostructure, may lead to formation of local minima in the material band structure, where carriers can localize and radiatively recombine. As demonstrated in the case of the MgZnO alloy, by Y. Hu *et al.* [152], alloying of the ZnO wurtzitic crystal with different concentration ‘ x ’ of Mg can be done in two possible ways: the Mg atoms can substitute the Zn ions in the ZnO crystal lattice or they can be partially incorporated in interstitial positions. In both cases, the concentration ‘ x ’ of Mg, in the $Mg_x Zn_{1-x} O$ alloy, affects the structural, electronic and optical properties of the ternary alloy. In the case of interstitial Mg-doping it has been proved that $Mg_x Zn_{1-x} O$ conductivity increases until $x < 15.89\%$, while it abruptly decreases for x above that value. This phenomenon, which inevitably affects the electronic and optical performance of the system, provokes local minima or deformation of the energy band as a function of the local Mg-doping in the ZnO

structure. One way to observe and measure the localization energy, in an alloy or at the heterointerfaces of a heterostructure, consists in varying the temperature in a certain range of values, for example as reported in the articles [153, 154, 139], from few Kelvin until room temperature. Indeed, at very low temperature carriers are trapped in local minima of the band structure and their thermal energy is not enough to move from one minimum to a deeper one. Such situation is called “*freeze up*” regime, depicted in figure 4.10(I). If we study the photoluminescence signal of the electron hole recombination, it corresponds to the average of the localized energy states. Increasing the

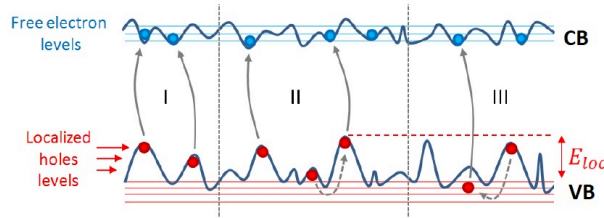


Figure 4.10: Scheme of interband transitions at different temperatures, in presence of alloy compositional fluctuations.

temperature, the bandgap is reduced following the Varshni’s empirical law [62], and we enter into the “*thermalization*” regime, fig. 4.10(II). In this regime the carriers trapped in local minima have enough energy to thermalize (jump) to the lowest minimum in their neighbors and, as consequence, the recombination energy is decreased with respect to the Varshni’s empirical law of a quantity which corresponds to the localization energy E_{loc} , as represented in fig. 4.10(II). Then increasing more the temperature free carriers can recombine and the electron hole recombination is in agreement with the estimated value through the Varshni’s law, this situation corresponds to the “*delocalization*” regime, fig. 4.10(III). The transitions between different recombination regimes produces the characteristic “S-shape” in the photoemission signal.

In figure 4.11 are reported the PL spectra related to evolution of the $Zn_{0.85}Mg_{0.15}O - ZnO - Zn_{0.85}Mg_{0.15}O$ signal at different thermal ranges: $T_I = [10; 50]$ K, $T_{II} = [70; 150]$ K and $T_{III} > 150$ K. Looking at the peak related to the ZnO-single quantum well (SQW), fig. 4.11, its energy first (T_I range) shows a redshift and then a blue shift (T_{II} range) followed by an another redshift, at $T > 150$ K, exhibiting the so-called “S-shape” [154].

In the article [154], the ‘S-shape’ behavior is explained within the model of localized

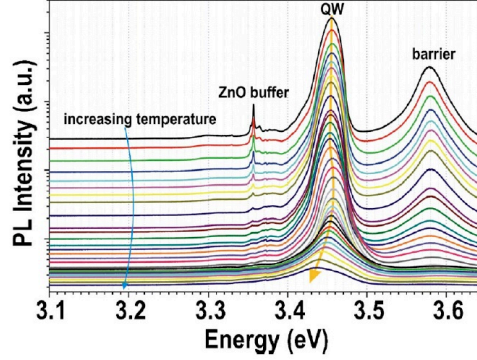


Figure 4.11: PL spectra of a $Zn_{0.85}Mg_{0.15}O - ZnO - Zn_{0.85}Mg_{0.15}O$ sample from the article [154]. The *S-shape* shift with increasing temperature is indicated by the orange arrow.

excitons, in agreement to what reported above and depicted in figure 4.10. In the Zn-MgO/ZnO/ZnMgO heterostructure, at the lowest temperatures, excitons are localized even in shallow lateral potential fluctuations due to the roughness of the ZnMgO-ZnO interfaces. When the temperature increased, excitons from shallow lateral potential fluctuations are delocalized and they can diffuse to regions with larger well widths and hence lower transition energies (redshift) with respect to the bandgap evaluated by the Varshni’s law [62]. The excitonic transitions in correspondence of regions of local minima of the bandgap is dominant at intermediate temperatures and the overlapping of this region, which corresponds to the blueshift photoemission, gives a PL emission in agreement with the bandgap energy, according to the Varshni equation [62]. The ‘S-shape’ behavior in the ZnO/MgZnO heterostructure was investigated along both the *c*- and *m*-axis directions [155]. In a quantum confined system, such as a QW, the carrier localization phenomenon asks to take into account more conditions. First we have to take into account that the emission energy is shifted towards higher energy, eq. (4.10), compared to the energy bandgap of the semiconductor constituting the well.

$$E_{PL,QW} = E_{gap} + E_{hh}^1 + E_e^1 - E_{ex}^1 \quad (4.10)$$

E_{hh}^1 is the energy related to the first excited state in the valence band, for *heavy holes*, and E_e^1 is the energy of the first excited state in the conduction band, while E_{ex}^1 is the exciton binding energy. In agreement with the equations (4.4) and (4.10), the energy bandgap of the QW can be tuned choosing its well thickness ' t_{QW} '. Furthermore it has to be considered in case of polar QW heterostructures, *e.g.* ZnO/MgZnO, if the QW-growth direction is along a polar plane or not. If the structure is grown along a polar direction, then the QW results affected by QCSE which reduces the electron-hole wavefunction overlaps and decreases the intensity of the PL emitted signal or the probability of the electron-hole recombination, as reported in the article [156]. In order to avoid the QCSE, heterostructures should be grown on non-polar planes. It's clear that carrier localization phenomena inside QWs can lead to significant variations of the emission energy. In the $Mg_xZn_{1-x}O$ alloy, localization phenomena can be related to local variations of the Mg concentration ' x '. Indeed usually, the concentration in alloys is not perfectly uniform and the PL emission signal usually comes from regions of the alloy, where the Mg concentration is lower and the MgZnO energy gap decreases its value.

4.1.4 Stress and Strain tensors of hexagonal systems

The deformation of a crystal lattice under the effect of an applied mechanical force can be described in terms of the relative displacements of the atoms of the lattice. This displacement of the ions that compose the crystal is accompanied by a new disposition of the electrons. In agreement with the classical theory of the elasticity, we can ignore the microscopic atomic structure of a crystal and consider it as a continuous medium [62]. Therefore a general deformation of the solid can be described in terms of a continuous displacement field $\vec{u}(\vec{r})$, specifying the vector displacement of the part of the solid that has the \vec{r} vector as equilibrium position. In particular, for a single atom placed at \vec{r} , in an arbitrary Cartesian system, the new position \vec{r}' is defined as (4.11):

$$\vec{r}' = \vec{r} + \vec{u}(\vec{r}) \quad (4.11)$$

When the spatial variation $\vec{\nabla} \cdot \vec{u}(\vec{r})$ of the vector \vec{u} is small, the elastic energy can be written as (4.12):

$$U = \frac{1}{2} \cdot \int \left(\frac{\partial u_j}{\partial x_i} \cdot C_{klmn} \cdot \frac{\partial u_n}{\partial x_m} \right) \cdot d^3\vec{r} \quad (4.12)$$

The C_{klmn} is the tensor of the elastic coefficients. The strain ϵ_{ij} , defined as (4.13), is a second rank tensor that gives the displacements relative to all atoms in the crystal lattice:

$$\epsilon_{ij} = \frac{1}{2} \cdot \left(\frac{\partial u_i}{\partial x_j} + \frac{\partial u_j}{\partial x_i} \right) \quad \text{with } i, j = 1, 2, 3 \quad (4.13)$$

In the equation u_i are the displacement vectors along the three axes of the Cartesian coordinate system. This tensor is referred to as strain tensor and is usually reported in its matrix form:

$$\epsilon = \begin{pmatrix} \epsilon_{11} & \epsilon_{12} & \epsilon_{13} \\ \epsilon_{21} & \epsilon_{22} & \epsilon_{23} \\ \epsilon_{31} & \epsilon_{32} & \epsilon_{33} \end{pmatrix} \quad (4.14)$$

By definition (4.13) the strain tensor is symmetric $\epsilon_{ij} = \epsilon_{ji}$. The diagonal terms (normal strain components) represent extension along the axis x_1, x_2, x_3 , while the off diagonal terms (shear or strain components) are related to rotations. The stress tensor represents the force applied per unit area of the crystal. This force, that can be due to an external perturbation or can be originated from the interaction of several regions into the crystal, can be represented as a second-rank tensor, equation (4.16), which is referred as the stress tensor (4.15):

$$\sigma = \begin{pmatrix} \sigma_{11} & \sigma_{12} & \sigma_{13} \\ \sigma_{21} & \sigma_{22} & \sigma_{23} \\ \sigma_{31} & \sigma_{32} & \sigma_{33} \end{pmatrix} \quad (4.15)$$

Strain and stress tensors are related within the limits of linear elastic theory by the Hooke's law:

$$\sigma_{ij} = \sum_{k=1}^3 \sum_{l=1}^3 C_{ijkl} \cdot \epsilon_{kl} \quad (4.16)$$

where the elements of the C_{ijkl} tensor are the elastic coefficients for the linear stress-strain relationship.

The inverse relation is mediated by the stiffness tensor S_{ijkl} (4.17):

$$\epsilon_{kl} = \sum_{m=1}^3 \sum_{n=1}^3 S_{klmn} \cdot \sigma_{mn} \quad (4.17)$$

The stress and strain tensor has $3 \times 3 = 9$ components each and therefore the elastic and stiffness matrix has $3^4 = 81$ independent elements each.

From the theory of elasticity, the σ_{ij} components are symmetric under this condition: $\sigma_{ij} = \sigma_{ji}$. Thus the equation (4.16) can be written as follows (4.18):

$$\sigma_{ji} = \sum_{k=1}^3 \sum_{l=1}^3 C_{jikl} \cdot \epsilon_{kl} \quad (4.18)$$

Subtracting the (4.16) from the (4.18) leads to the following result: $C_{ijkl} = C_{jikl}$. Combining the equation (4.16) with the symmetry property of the strain tensor $\epsilon_{kl} = \epsilon_{lk}$ (4.13), we obtain the new expression (4.19):

$$\sigma_{ij} = \sum_{l=1}^3 \sum_{k=1}^3 C_{ijlk} \cdot \epsilon_{lk} \quad (4.19)$$

Then comparing the equation (4.19) with the (4.16) we deduce that: $C_{ijkl} = C_{ijlk}$. These symmetric properties allow to express the stress and strain relationship as follows (4.20):

$$\sigma_i = \sum_{k=1}^3 C_{ik} \cdot \epsilon_k \quad (4.20)$$

where[62]:

$$\begin{aligned}
\sigma_{11} &= \sigma_1 & \epsilon_{11} &= \epsilon_1 \\
\sigma_{22} &= \sigma_2 & \epsilon_{22} &= \epsilon_2 \\
\sigma_{33} &= \sigma_3 & \epsilon_{33} &= \epsilon_3 \\
\sigma_{23} &= \sigma_4 & \epsilon_{23} &= \epsilon_4 \\
\sigma_{13} &= \sigma_5 & \epsilon_{13} &= \epsilon_5 \\
\sigma_{12} &= \sigma_6 & \epsilon_{12} &= \epsilon_6
\end{aligned} \tag{4.21}$$

In this reduced form the C_{ik} matrix consists of 36 independent constants whose knowledge is important to describe the elastic properties of the considered system. When the considered system is a crystal, due to the symmetries which characterize the lattice, the number of independent constants is reduced to 5 for hexagonal systems, as the wurtzite structure of ZnO. The Hooke's law then can be respectively expressed as follows:

$$\begin{pmatrix} \sigma_1 \\ \sigma_2 \\ \sigma_3 \\ \sigma_4 \\ \sigma_5 \\ \sigma_6 \end{pmatrix} = \begin{pmatrix} C_{11} & C_{12} & C_{13} & 0 & 0 & 0 \\ C_{12} & C_{11} & C_{13} & 0 & 0 & 0 \\ C_{13} & C_{13} & C_{33} & 0 & 0 & 0 \\ 0 & 0 & 0 & C_{44} & 0 & 0 \\ 0 & 0 & 0 & 0 & C_{44} & 0 \\ 0 & 0 & 0 & 0 & 0 & \frac{(C_{11}-C_{22})}{2} \end{pmatrix} \cdot \begin{pmatrix} \epsilon_1 \\ \epsilon_2 \\ \epsilon_3 \\ \epsilon_4 \\ \epsilon_5 \\ \epsilon_6 \end{pmatrix} \tag{4.22}$$

In the case of ZnO wurtzite structure the value of the five independent elastic constants (C_{11} , C_{12} , C_{13} , C_{33} , C_{44}) that appear into the matrix (4.22) has been largely investigated in literature [157, 158]. The table 4.2 shows a comparison between the values of the second order elastic coefficients (SOECs) of ZnO that, as reported in [159], were obtained through different theoretical models.

4.1.5 Strain effect on band structure of ZnO

The relative displacement of atoms within a crystal lattice affects the electron and hole states energies and probability distributions in two different ways: by directly modifying

SOECs	$C_{11}(GPa)$	$C_{12}(GPa)$	$C_{13}(GPa)$	$C_{33}(GPa)$	$C_{44}(GPa)$
PAW PBE [159]	197.5	112.2	97.9	204.3	34.24
Exp [157]	209.7	121.1	105.1	210.9	42.5
LDA [158]	209	85	95	270	46

Table 4.2: Second-order elastic coefficients of bulk ZnO.

the band structure of the system as the distance between atoms changes and by changing the polarization properties of the system, so that a non-uniform distribution of charges is obtained within specific crystal types and along specific directions. Here we focus on the first case, where the effects of strain are described within the framework of deformation potential theory, by additional terms in the effective Hamiltonian which are referred to as deformation potentials.

Deformation potentials:

The Hamiltonian of the strained system can be written as the sum of the unperturbed Hamiltonian and a contribution induced by strain:

$$H = H_0 + H_\epsilon \quad (4.23)$$

where the strain related term can be expressed in terms of the unperturbed crystal potential V and strain tensor components $\epsilon_{i,j}$ as:

$$H_\epsilon = \sum_{i,j} \frac{\partial V}{\partial \epsilon_{i,j}} \epsilon_{i,j} \quad (4.24)$$

For (4.24) to hold, the strain and the consequent variations from the unperturbed Hamiltonian have to be small. In this case, first-order perturbation theory allows expressing the relative band shifts (energy shift considered for the valence band) due to strain as a function of the deformation potential components, as reported in ref. [160, 149]. Both the conduction and valence band edges are affected by the strain-induced energy shift and deformation potentials can be defined for the two cases. More details on the way in which these terms can be generated can be found in literature [161, 162]. It is worth

noting that it is not usually easy to have access to the deformation potentials for the conduction and valence bands, separately. Deformation potentials for the band gap can thus be defined and the relative contribution from the shifts of the two band can be issued by first principle calculations [163]. The deformation potentials of the ZnO valence band (D_1 , D_2 , D_3 and D_4) were derived by Rowe *et al.* [160] and their values, are reported in table 4.3.

	D_1 eV	D_2 eV	D_3 eV	D_4 eV
ZnO	-2.66 ± 0.30	2.82 ± 0.30	-1.34 ± 0.30	1.00 ± 0.30

Table 4.3: Valence band deformation potentials (in eV) of ZnO [160], at T=77 K.

Chapter 5

Coupled “*in-situ*” μ PL/La-APT measurements of the ZnO/MgZnO MQWs system

5.1 The ZnO/MgZnO sample

The *ZnO/MgZnO* heterostructure analyzed is a MQW system and, by convention, *ZnO* indicates the material which composes the QWs, while *MgZnO* indicates the material which forms the barriers. The samples were grown on $10 \times 10 \text{ mm}^2$ *ZnO* substrates, oriented along the non-polar *m-plane* by plasma assisted molecular beam epitaxy (MBE), more details about the technique of growth can be found in the references [151, 164, 165]. The substrates were annealed at 1065°C under an oxygen (O) atmosphere to reveal the atomic steps. The atomic O was provided by a plasma cell at 420 W and its flow was set to $5 \text{ mm}^3/\text{s}$. The substrate temperature was set to 420°C . The Zn and O fluxes were adonlyed with a growth rate of $170 \text{ nm}/\text{h}$, in order to be close to the stoichiometry and to limit the defect concentrations. The structures consisted of a 150 nm ZnO buffer layer followed by 10 periods of ZnO-QW/MgZnO-barrier, as outlined in fig. 5.1.

The ZnO/MgZnO heterostructure has a wurtzitic crystal structure, the nominal Mg

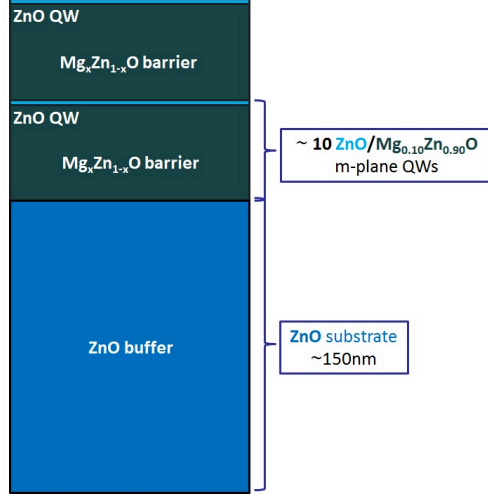


Figure 5.1: Schematic of the hierarchic structure of the ZnO/MgZnO MQW heterostructure.

concentration is 10% and the thickness of the barriers is $\approx 45 \text{ nm}$, while the thickness of the wells increases if we move from the base of the sample, the position closer to the substrate, towards the top of the heterostructure. The ZnO layer thickness range typically from 1.5 to 4 nm and the total length of the MQW heterostructure was kept below 150 nm in order to avoid plastic relaxation effects. As explained in the previous section 4.1.1 and in the articles [150, 151], the tuning of the *Mg* concentration in the *MgZnO* barrier plays an important role on the *wz*-lattice parameters that can give a residual strain along the *c-plane* direction and such strain can propagate within the ZnO QW. When the *ZnO/MgZnO* MQWs system is grown along the *m-nonpolar* direction, the situation is different. Indeed, as H.Matsui *et al.* [151] have demonstrated, the *MgZnO* layers repeat the surface structure of the underlying *ZnO* layers. Thus the *MgZnO/ZnO* interfaces in MQWs are periodically modulated by the substrate array. Furthermore, as known, as the *Mg* concentration '*x*' as the thickness of the QWs can be chosen respectively to tune the *MgZnO* and *ZnO* bandgaps. In the present case, ranging the thickness of the QWs between 1.5 and 4 nm we expect the effective bandgap between ≈ 3.9 and $\approx 3.4 \text{ eV}$, while for the *Mg_xZn_{1-x}O* barriers, the nominal thickness is $\approx 45 \text{ nm}$, while the nominal *Mg* concentration x_{Mg} is to evaluate by the PL-spectra,

using the equation (4.2), and it can be compared with the value obtained by the APT reconstruction.

5.1.1 Morphological and structural characteristics of the APT specimens

In order to investigate the structural, compositional and optical properties of the $ZnO/Mg_xZn_{1-x}O$ MQWs system, through the coupled APT- μ PL setup, the specimens were prepared following the standard lift-out procedure. The preparation of the specimen by SEM-FIB was introduced in the section 1.4, Chapter 1. The most important aspect during the preparation of specimens by focused ion beam (FIB) is to preserve their structure. Indeed ion implantation can take place, causing amorphization/damaging, particularly of the topmost 3-4 periods of the MQW system. In the worst case, the presence of damaged regions extending the whole surface can lead to a non radiative recombination of carriers, reducing the optical μ PL emission from a single field-emitter. Far from the surface, the crystalline properties of the samples are preserved and the generation of electron-hole pairs is still possible under μ PL analysis. FIB preparation of MQWs systems is used, since the quantum confinement carrier localization prevents the non-radiative recombination at the surface of the specimens.

After that the chunk was milled down with the characteristic apex radius $\approx 50\text{ nm}$, in order to study the morphological properties of the $ZnO/MgZnO$ MQW system, the sample was observed/analyzed by scanning electron microscopy “SEM”. Without repeat the process of fabrication of APT-specimens, reported in the first Chapter, here we limit to remind that in order to observe the sample through SEM technique, the materials, which compose them, have to be conductive. The two $ZnO/MgZnO$ specimens, reported in this thesis, are conventionally called tip A2 and tip A3. In order to acquire the SEM images of the two samples, reported in figure 5.2(a) and (b), the samples were kept inside a vacuum chamber at room temperature and $p = 1.33 \cdot 10^{-5}\text{ mbar}$. The electronic beam was selected at $V_{DC} = 5\text{ kV}$ and, at this value of the V_{DC} bias, the maximum spatial resolution reached, it is $\approx 1.5 \div 2.5\text{ nm}$, as reported in ref. [15].

The geometrical characteristics of the tips A2 and A3 are outlined in the table 5.1.

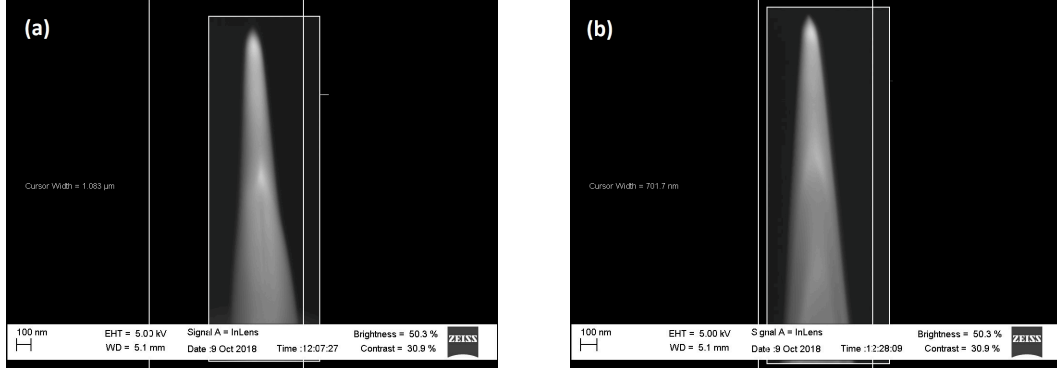


Figure 5.2: SEM images of the (a) tip A2 and (b) tip A3, which are ZnO/MgZnO MQW heterostructures. The SEM images were acquired at 100 nm scale.

needle specimen	apex radius R_{apex} (nm)	base radius R_{base} (nm)	length L (μm)
tip A2	53 ± 2	243 ± 2	2.170 ± 0.002
tip A3	51 ± 2	232 ± 2	2.290 ± 0.002

Table 5.1: Geometrical parameters of the analyzed ZnO/MgZnO MQWs heterostructures, evaluated by SEM measurements.

Thanks to this SEM-observations we have the geometrical information, about the given samples, that will be employed for the 3D-virtual APT-samples reconstruction. The SEM technique has a worse spatial resolution than the high-angle annular dark field (HAADF) and scanning-transmission electron microscopy (STEM) techniques. These two techniques were employed to carry out the morphological and compositional analysis of the first $ZnO/MgZnO$ nanoneedles analyzed through the coupled $\mu PL/La - APT$ system, by Simona Moldovan, as reported in E. di Russo's thesis [1].

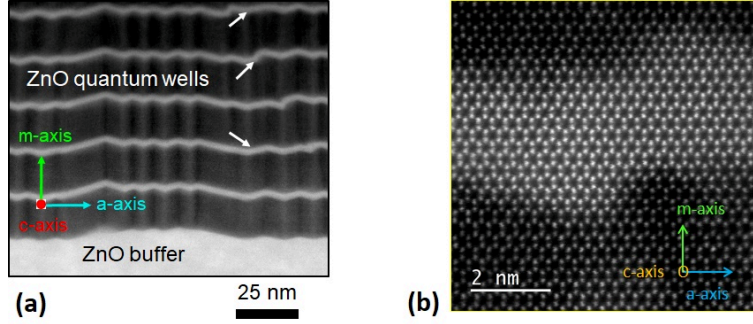


Figure 5.3: (a) STEM-HAADF image of a $ZnO/MgZnO$ atom probe specimen. The white layers are the ZnO QWs and the darker ones are the $MgZnO$ barriers; (b) Zoom in on a QW and the next barriers at the best STEM spatial resolution.

The images, of the $ZnO/MgZnO$ heterostructure, which appear in E. di Russo's thesis [1], at two different magnifications are reported in figure 5.3(a) and (b).

I choose to report these images, in order to compare, after the APT reconstruction of the tips A2 and A3, the differences and the affinities with this first $ZnO/MgZnO$ APT-specimen analyzed through the coupled $\mu PL/APT$ system.

In order to understand what is reported in figure 5.3(a) and (b), the working principle of the STEM-HAADF technique is subsequently summarized below.

In STEM, a highly focused electron beam is used in order to scan the specimen surface; such system is advantageous compared to a simple Transmission Electron Microscope (TEM), since it offers unique imaging modes, which give access to the spatial dimension of the heterostructures, with a spatial resolution of 0.09 nm , comparable to the atomic resolution. Furthermore, using STEM in dark field mode (HAADF), the intensity, of the STEM acquired images (*e.g.* fig. 5.3), scales with the atomic number Z of the ele-

ments within the specimen. Indeed, in HAADF mode, only electrons scattered at high angles ($\approx 30 \text{ mrad}$) are collected by an annular detector and no diffracted electrons and the images are formed by the elastically scattered electrons which have passed very close to the atomic nuclei (Z) of the specimen. In this way, the HAADF-STEM images are not affected by diffraction and high resolution structural information is obtained, allowing to distinguish between regions where the Mg atoms replace the Zn atoms in the ZnO ordered lattice, forming $Mg_xZn_{1-x}O$ alloy. The $Mg_xZn_{1-x}O$ barrier is darker than ZnO and the different shades of darkness related to the $Mg_xZn_{1-x}O$ alloy can be observed as a function of the Mg II-site fraction in it. Summing up, the decreasing of Mg II-site fraction in the $Mg_xZn_{1-x}O$ alloy increases the HAADF intensity.

The composition profile within the $MgZnO$ barriers is not uniform, figure 5.3, and in particular Mg -depleted or enriched regions along the a -plane are pointed out by the corresponding HAADF contrast. The high resolution-STEM-HAADF images, figures 5.3, reveal that the ZnO buffer used for the growth of that sample does not have a flat interface, but it shows an irregular V-groove grating profile and the same morphology is preserved by all the layers grown on this ZnO buffer. The V-groove grating profile of ZnO -QWs, along the m -axis, was explained by Matsui *et al.* [151, 165] in terms of the inhibition of interlayer transport due to a strong step-edge barrier. As shown in figure 5.3(b), no interdiffusion or other effects leading to compositional gradients are visible across the interface between the ZnO -QWs and the $MgZnO$ -barriers.

Due to the different adatom diffusion during growth along the c - and a -axis in the plane of layers, a spatially coherent corrugation develops starting from the bottom contact layer up to the cap layer. The $MgZnO$ segregation regions, outlined by the HAADF vertically different dark intensity shades, which occur below the minima of the V-groove grating profile, are due to compositional inhomogeneities rather than the non-uniform strain states, as demonstrated by E. di Russo *et al.* [166]. The Mg -II site fraction varies by $\pm 10\%$ in absolute values at the bottom and the top of the corrugations. In particular, the Mg nominal barrier thickness is of $t_{barr} = 15 \text{ nm}$ and looking at figure 5.3, within the $Mg_xZn_{1-x}O$ barriers, the darkest lines, which occur in correspondence with top groove edges, are the enriched Mg -regions ($x = 0.4$), while the regions with brightest contrast are found in correspondence with bottom groove edges and they indicate

the *Mg* depleted regions ($x = 0.3$). The values of the different *Mg*-concentrations were, also in that case, evaluated and confirmed, subsequently, by the complementary APT/ μ PL reconstruction analysis [167].

In the next sections, the collection and elaboration of the data, by the coupled “*in-situ*” μ PL/La – APT” system, is reported and finally the results obtained for the tips A2 and A3 are discussed.

5.2 The *in-situ* μ PL/La-APT analysis

The working principle of the coupled microphotoluminescence and the tomographic atom probe instrument were widely introduced in Chapter 1. The challenging idea of the “*in-situ*” approach allows to strictly correlate the variation of the PL signal with nano-metric scale volumes of the tip evaporated during the APT analysis. This method opens new perspectives for the study of optical properties of the semiconductor specimens probed, since it presents more advantages than a simple μ PL setup. For instance:

- differently by common μ PL analysis, the optical emission of single nano-objects, which are present in the APT-specimen, can be distinguished, since the APT analysis is based on the evaporation of the radiative centers which compose the specimen, layer by layer, particle by particle;
- with the coupled “*in-situ*” La-APT/ μ PL system a better spatial resolution ($<100nm$) than the μ PL spectroscopy ($\sim \frac{\lambda}{2}$) can be obtained;
- the coupled “*in-situ*” La-APT/ μ PL system allows correlating the PL emission with both morphology and composition of the specimen.

In the following sections, I will discuss about:

- the μ PL/APT protocol;
- the analysis of the collected data.

The $\mu PL/APT$ protocol is a method which allows to minimize the operation of manipulation of the specimen, since μPL and APT experiments are performed simultaneously. The data collected, following this protocol, correlate the optical and structural properties of the probed specimens. In order to yield the 3D sample reconstruction, the mass spectra, time-of-flight spectra are obtained by the elaboration of the collected data, as in standard atom probe experiment, and the change of the physical properties of the system during the experience, for different values of the V_{DC} bias, are reported.

5.2.1 Protocol for the correlative analyses

The possibility to run the μPL and APT experiments, at the same time and “*in situ*”, critically depends on the matching of the experimental parameters, which have to work for both analyses. Experiments were performed keeping the specimen under ultrahigh vacuum conditions ($p < 10^{-7} Pa$) and at low temperature: $T_{base} = 80 K$. The PL setup is the same one employed for the analysis on the diamond tips, described in Chapter 1 and Chapter 3. The laser wavelength was selected in the UV range, at $260 nm$, the laser repetition frequency at $0.5 MHz$ and the incident power was tuned at $600 \mu W$. These values allowed to have a good PL signal from the $ZnO/MgZnO$ specimen and to run, at the same time, APT analysis. As saw for diamond tips, the laser beam waist, focused by a spherical mirror on the tip specimen, is about $1.5 \mu m$.

The first step, before to begin the coupled μPL and APT experience “*in-situ*”, is to assure that the MQWs system is not too damaged by the FIB preparation and so that the heterostructure-needle preserves most of the optically active region. In order to check that, the sample is probed by only the laser beam, without any applied bias, focusing the spot laser on the apex of the APT specimen, where we expect to collect a signal by the whole heterostructure. The PL signal is collected and analyzed through a grating spectrometer with $320 mm$ focal length and with the highest spectral resolution of around $0.5 meV$, equipped with a nitrogen-cooled CCD camera. Generally, the first spectrum is acquired selecting the grating density with widest wavelength range, to be sure to acquire the signal from each component of the heterostructure. The μPL -spectra, related to the tip A2 and tip A3, are showed in figure 5.4. In both spectra,

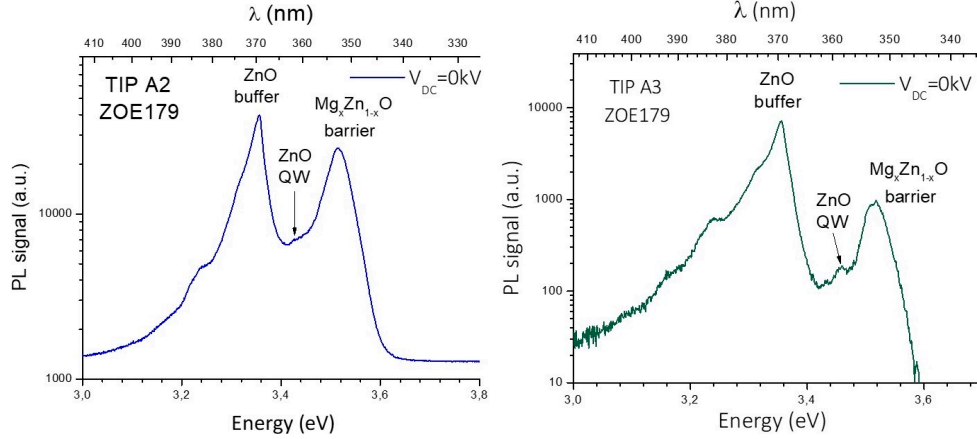


Figure 5.4: PL signal of tip A2 and A3, ZnO/MgZnO MQW heterostructure, without bias.

acquired without any V_{DC} applied bias the dominant peak appears at ≈ 3.36 eV and it is associated to the radiative recombination of the bulk ZnO substrate, the emission at ≈ 3.44 eV is associated to the recombination of the localized excitons in the ZnO-QWs and finally the broad peak centered at ≈ 3.51 eV is associated to the $Mg_xZn_{1-x}O$ barriers. Using the equation (4.2), reported in the section 4.1.1, the average value of the Mg II-site fraction in $Mg_xZn_{1-x}O$ barriers can be derived. The Mg-concentration was found to be: “ $x_{Mg} = (0.08 \pm 0.03)$ ”, such value will be verified and compared with the results of the APT-analysis. Both spectra show the signals of the three components peaked around the same average values, meaning that the thickness of the QWs and the $Mg_xZn_{1-x}O$ barriers average composition of the tips A2 and A3 is the same one or really close. Indeed, the two APT-samples were obtained by the same ZnO/MgZnO heterostructure. Once assured to have a good PL signal from the APT specimen, the coupled La-APT and μ PL experience begins. The APT acquisition data software was developed by G rald da Costa, at the University of Rouen. Through this software is possible to control and to choose the parameters that assist the laser-assisted field evaporation. In order to recognise the ions of the elements which constitute the given APT sample and to obtain the final APT 3D-virtual sample reconstruction, the different *mass/charge* [Da] ranges, where the peaks of the related different ions have more

probability to fall within, were selected, more details in section 5.2.2.1. In order to start the evaporation and the detection of the ions from the apex of the APT-specimen, the positive bias was manually increased, from $V_{DC} = 0 \text{ kV}$, at steps of $\Delta V_{DC} = 0.5 \text{ kV}$. When the detected impacting ions are of the order of magnitude 10^5 events , it is assumed that layers of ions by the apex of the tip start to evaporate and the detection rate is fixed at the optimized selected value: $\varphi = 0.0025 \text{ ions/pulse}$. This parameter can have fluctuations, $\varphi = 0.0023 \div 0.0028 \text{ ions/pulse}$, in correspondence of the interface between layers having different evaporation fields and as a function of the depth, since the geometry of the tip changes. A decreasing of the value of the detection rate is followed by a decreasing of the magnification of the reconstructed specimen. So, we choose to keep the detection rate automatically constant by the acquisition software. The correlated acquisition of the data, through the μPL -APT system, was manually piloted. Each time that one μPL -spectrum was acquired, $\Delta t \approx 120 \text{ s}$, it was noted down the number of detected ions, respectively: at the beginning and at the end of the recorded μPL -spectrum by the CCD. In this way, it was possible to follow in real time, during the layers evaporation, the evolution of the peaks related to the ZnO -MQWs, the MgZnO -barriers and the ZnO -substrate. The column headers of the table 5.2 outline the experimental variables which were recorded, step-by-step, in order to merge, at the end of the experience, the APT and μPL information.

The experiment was concluded when all the QWs and the barriers of the APT sample

# origin file	$\Delta t_{\text{acquisition}}$ (s)	# atoms beginning	# atoms end	V_{DC} (kV)	# evaporated QWs	Comments
...
:	:	:	:	:	:	:

Table 5.2: Column headers of the collected data during the coupled *in-situ* μPL -APT experiment. The table with the complete list of values is reported in **Appendix A**.

were completely evaporated and the software shows the detection of only zinc and oxyde events, related to the bulk substrate of the MQW heterostructure.

At the end of the specimen evaporation, the La-APT and μPL data are elaborated

separately and then put in correlation in order to merge the optical and structural information related to the $ZnO/MgZnO$ MQWs system studied. For sake of simplification, I choose to report, in the next sections, the experimental results related only to the tip A2, while the experimental results related to the tip A3 are reported in **Appendix B**. Indeed, both tips came from the same sample, labeled ‘ZOE179’ and the results are in good agreement.

5.2.2 Data acquired by the La-APT system

5.2.2.1 Mass spectrum

The $ZnO/Mg_xZn_{1-x}O$ APT-samples were analyzed along the direction of growth, the $[1\bar{1}00]$ crystallographic orientation, which corresponds to the m -axis. The *mass/charge* ranges were selected at the beginning of the APT acquisition, in order to measure the composition of the evaporated sample and to identify each peak in the mass spectrum.

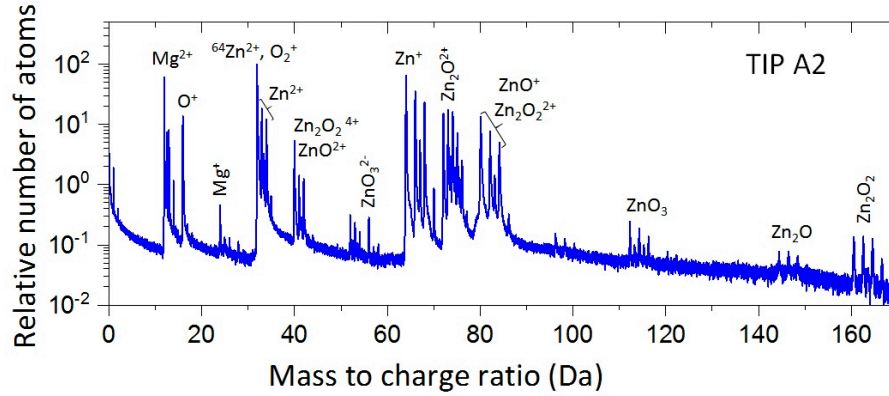


Figure 5.5: The mass spectrum related to the tip A2. The elaboration of the APT-data was realized by Pradip Dalapati.

In the mass spectrum of the $ZnO/MgZnO$ heterostructure, figure 5.5, peaks of several ions are grouped in different ranges and we can observe that:

- the isolated peak at 32 Da was interpreted as an overlap of $^{64}Zn^{2+}$ and O_2^+ ;

- the peaks within the mass range 39.78-42.10 Da were attributed to ZnO^{2+} and $Zn_2O_2^{4+}$;
- the peaks within the mass range 79.59-84.41 Da were attributed to ZnO^+ and $Zn_2O_2^{2+}$.

The zinc “Zn” has five isotopes: $^{64}Zn^{2+}$, $^{66}Zn^{2+}$, $^{67}Zn^{2+}$, $^{68}Zn^{2+}$ and $^{70}Zn^{2+}$, while oxygen “O” has three isotopes: $^{16}O^+$, $^{17}O^+$ and $^{18}O^+$. The relative abundances of $^{70}Zn^{2+}$ and $^{17}O^+$, $^{18}O^+$ are very small ($< 0.6\%$) so such species are not taken in account for the APT reconstruction, in the mass spectrum.

As noted above, $^{64}Zn^{2+}$ and $^{16}O^+$ ions have the same *mass/charge* ratio, so they form a unique peak at $\approx 32 Da$. Since the natural abundance of $^{64}Zn^{2+}$ zinc isotope is known to be $\alpha_{64} = 0.483$, it is possible to evaluate the total amount of Zn and O atoms, using the following equations (5.1), (5.2):

$$N^{Zn} = N^{Zn_{66 \rightarrow 68}} / (1 - \alpha_{64}) \quad (5.1)$$

$$N^O = 2 \cdot (N^{32} - (1 - \alpha_{64}) \cdot N^{Zn}) \quad (5.2)$$

N^{32} is the number of events detected at the peak $m/n \approx 32 Da$. $N^{Zn_{66 \rightarrow 68}}$ is associated to $^{66}Zn^{2+}$, $^{67}Zn^{2+}$ and $^{68}Zn^{2+}$ isotopes. In the equation (5.2) the factor 2 is added, because each $^{16}O_2^+$ ion is composed by two oxygen atoms.

Within the mass range 31.94-35.20 Da, in figure 5.5, it is possible to calculate the respective total amount of zinc and oxygen. The same method has also been adopted in the mass range 39.78-42.10 Da and 78.41-88.50 Da.

Furthermore, as reported in E. di Russo’s thesis, it is important to consider that the DC evaporation field of the tip affects the atomic fractions of the detected ions which appear in the mass spectrum. The number of Zn^+ detected ions are observed to decrease when the DC field is increased and the Zn^{2+} ions don’t compensate them, while the O_2^+ are more abundant at high field conditions. For this reason is extremally important to choose and know with precision the experimental conditions adopted during the experiment. The charge-state-ratio Zn^{2+}/Zn^+ is extracted from the mass spectra by comparing intensities of Zn^{2+} and Zn^+ ions, respectively, in the 31.94-35.20 amu

and 63.85-70.12 amu mass ranges values. The Zn^{2+}/Zn^{+} ratio was used to evaluate the effective evaporation field, using the Kingham's curves, that Kingham's evaluated by his post-ionization model, introduced in the section 1.2.8. In the present case, $F \cdot k_f$ was $\approx 15 \text{ V/nm}$ for $E_{laser} = 1.2 \text{ nJ}$.

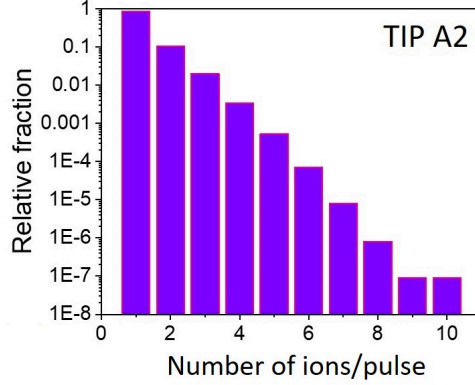


Figure 5.6: Distribution of multiple-ion events associated to the mass spectrum presented in fig 5.5. 87% of the total events is associated to single events, while the remaining 13% is associated to multi-ions detection.

The multiple-ion events were introduced in the section 1.2.7.4, Chapter 1. These events can depend on: kind of material, analysis conditions and tip geometry. The abundance of single events associated to the mass spectrum is $\sim 87\%$, while $\sim 13\%$ of the total number of events is associated to multi-ion events. The distribution of multiple-ion events associated to the mass spectrum are presented in figure 5.6. The multi-ion events may be numerous and phases with different evaporation fields may produce multi-ion events. In ZnO , the analysis of multi-ion events is difficult due to the Zn isotopes, so, many molecular ions and peaks can overlap. Furthermore, some dissociation reactions can lead to the production of some neutral fragments, which cannot be detected and so they constitute the loss information. Dissociations processes can be field-induced phenomena and they can take place very close to the tip surface. In order to take into account the impact factor of this process on the measured composition, Zanuttini *et al.* studied the dissociation of ZnO^{2+} ions [168]. They demonstrate that several dissociation channels exist for the ZnO^{2+} ions and they strongly

depend by the orientation of the ion with respect to the electric field. The reaction: $ZnO^{2+} \rightarrow Zn^{2+} + O$ produces a neutral fragment that is not detected at low field and that becomes post-ionized at higher field, in agreement with the ZnO behavior [1]. Therefore, during the field evaporation process, neutral molecules can be formed and since they are no charged particles, they constitute a selective loss of atoms which are no accelerated towards the detector. The study performed by Enrico *et al.* [167] demonstrated that, notwithstanding the La-APT technique is not exempt from compositional biases, accurate site fractions of semiconductors ternary alloys, likes $Mg_xZn_{1-x}O$, can be obtained at low surface field conditions. The experimental results were interpreted using a simple preferential evaporation model, described in ref. [167], which can be transposed to other semiconductor alloy systems.

5.2.2.2 3D reconstruction

During the APT experiments the applied bias increases slowly in order to counterbalance the effects of the increase of the apex radius. The 3D virtual volume specimen reconstruction was made applying the “standard reconstruction algorithm”. The experimental parameters for the reconstruction of the tips A2 and A3 are summarized in table 5.3.

	TIP A2
<i>Projection point</i> (m+1)	1.8
$F \cdot k_f$ (V/nm)	15
<i>Curvature factor</i>	0.8
<i>Detection efficiency</i>	0.4

Table 5.3: Tip A2 parameters given by the APT 3D-reconstruction: *projection point*, $F \cdot k_f$, *curvature factor*, *detection efficiency*.

For both the experiments, the detection rate “ φ ” was kept constant, in order to have a stable value of the magnification related to the 3D reconstruction. The hitmaps in figures 5.7 were collected along the whole experiment. In particular, in figure 5.7(a) the distribution of Zn^+ ions looks statistically mostly uniform except for a border side

effect. The hitmap in figure 5.7(b) reports the charge state ratio (CSR), section 1.2.8 of Chapter 1, of the Zn^{2+}/Zn^+ ions, which shows that the average surface field across the different regions of the whole APT specimen is quite uniform. Inhomogeneity of the electric field is highlighted by the bias of the Zn^{2+}/Zn^+ ions distribution present on the border of one side of the CSR hitmap.

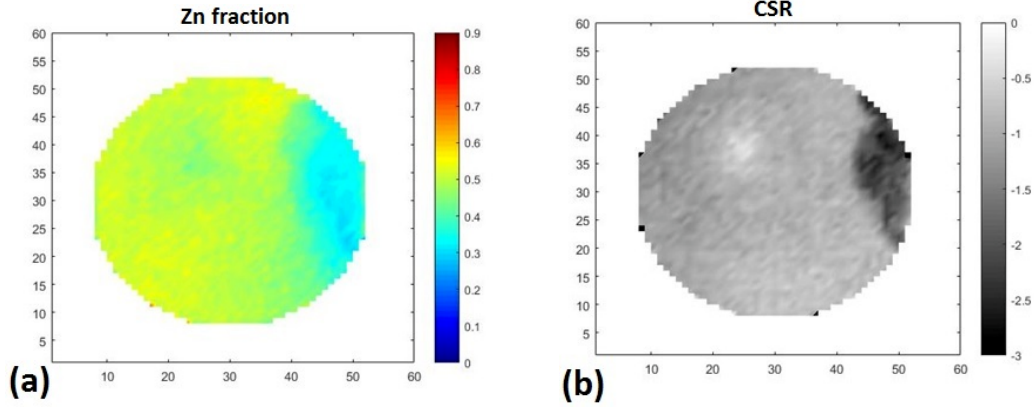


Figure 5.7: Hitmaps of: (a) the Zn atomic fractions visualized through detector statistics and (b) the Zn^{2+}/Zn^+ charge state ratio (CSR).

The reconstruction of the 3D volume of the tip A2, in figure 5.8(a) reports a certain percentage of the Mg^{2+} detected ions in blue and another percentage of the Zn^{1+or2+} detected ions in red.

The values correspond to the average measured composition along the crystal a -axis and the measured II-site fraction is calculated using the equation (5.3):

$$x = \frac{N_{Mg}}{N_{Zn} + N_{Mg}} \quad (5.3)$$

where N_{Zn} and N_{Mg} are respectively the number of zinc and magnesium ions detected. In order to study the $MgZnO$ barriers, a chart of the detected Mg II-site fraction was computed and the 2D distribution of the Mg II-site fraction is reported in figure 5.8(b).

The Mg II-site fraction chart shows that there is not a relevant variation of the Mg II-site fraction along the a -axis and the m -axis directions, inside the $MgZnO$ barriers.

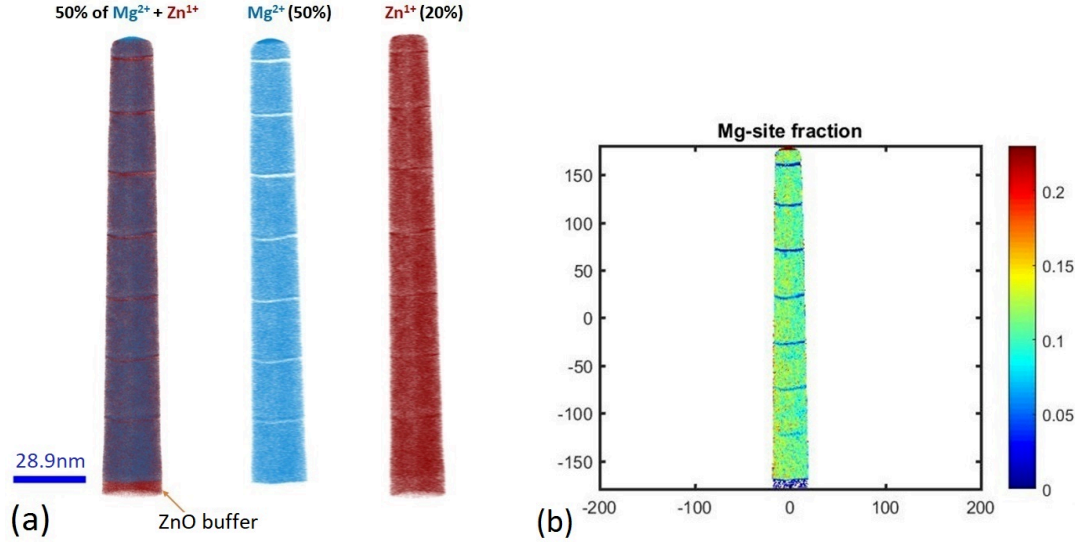


Figure 5.8: (a) 3D volume reconstruction of the tip A2 with both the Mg^{2+} and Zn^{1+or2+} ions, on the left side, and 3D virtual reconstruction only with the Mg^{2+} and Zn^{1+} ions, on the right side. (b) 2D-distribution of the Mg II-site fraction, calculated over a volume of $(30 \times 30 \times 40) \text{ nm}^3$.

5.2.2.3 Mg -concentration profile

The Mg II-site fraction profiles were studied along the:

- m -axis in order to get informations about the average value of the Mg II-site fraction along all the sample and in order to evaluate the QW thickness, observing the Mg II-site fraction variation across the QW;
- a -axis in order to investigate the Mg II-site fraction fluctuation inside the $MgZnO$ barriers.

In figure 5.9 is plotted the trend of the Mg II-site fraction detected during the APT-analysis and it looks quite regular, which means that also the evaporation field is almost constant. The average Mg II-site fraction along the m -axis, in fig. 5.9, is evaluated to be more near to 0.086 ± 0.018 , such as generally for the propagation of errors, in order to evaluate the error it has been used the semidifference related to the values of the Mg II-site fraction oscillations.

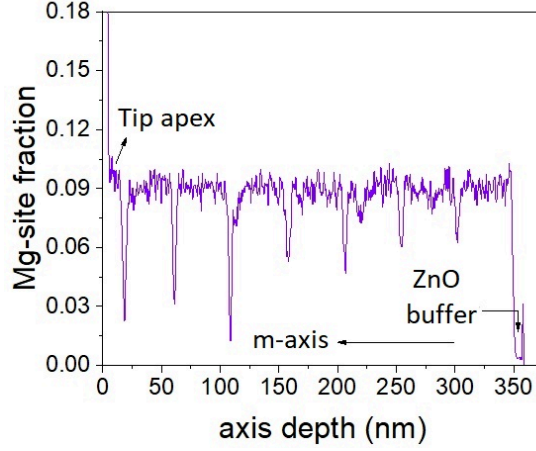


Figure 5.9: *Mg* II-site fraction profile measured along the *m-axis* direction. The minima are associated to a decreasing of *Mg* content that is abrupt in the QWs regions.

For convention, we started to enumerate with the lowest index the QW or barrier closest to the *ZnO*-substrate and then increasing the indexes of the QWs and barriers, sequentially, moving towards the tip apex.

In order to study the alloy fluctuation inside the *MgZnO* barriers, the *Mg*-profile along the *a-axis* was investigated. The profiles, in fig. 5.10, revealed that the *Mg* II-site fraction is almost constant within the barriers and the average value estimated for each *MgZnO* barrier is reported in the table 5.4. Along the *m-axis*, in correspondence of the crossing of each *ZnO*-QW, where the *Mg* concentration decreases, the FWHM of the *Mg*-peak profile fluctuation, fig. 5.11, was evaluated and also in this case the average values of the thickness of the QWs are reported in table 5.5.

Looking at the data collected in table 5.4, we can observe that, for the tip A2, the *Mg* II-site fraction inside the barriers is almost constant and it oscillates around an average value $\approx (0.088 \pm 0.008)$. Furthermore, also the QWs have not constant thickness and, in the specific case of the tip A2, the thickness of each QW was estimated and these values are listed in table 5.5, moving from the first QW towards the last one it is easy to compare the size of each quantum well with the nearest neighbors and to see that the QWs increase and decrease their thickness in sequence. The *Mg* concentration

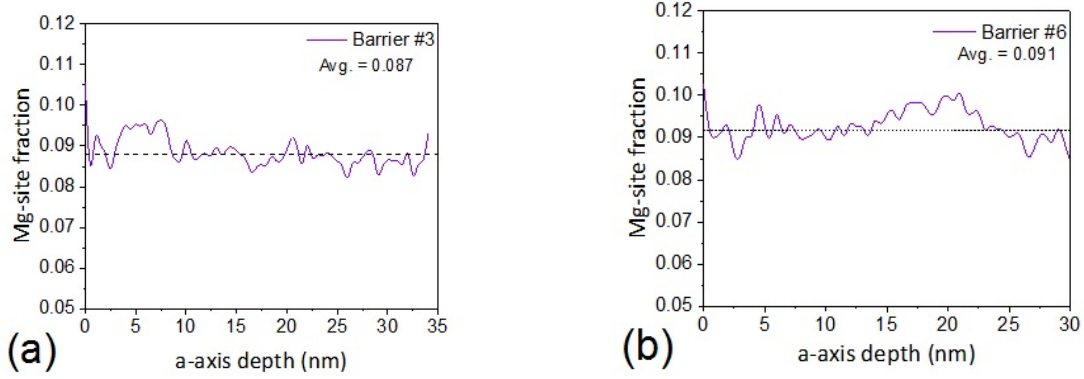


Figure 5.10: *Mg* II-site fraction profiles measured along the *a*-axis direction evaluated in a volume of $(30 \times 30 \times 40) \text{ nm}^3$ within the barrier 1 (a) and the barrier 2 (b). The maxima are associated to an increased *Mg* content, while the minima to a decreased *Mg* content. The dotted lines represent the average values of the *Mg* II-site fraction, which are equal to 0.087 ± 0.008 and 0.091 ± 0.009 , respectively. The analysis were performed by Pradip Dalapati.

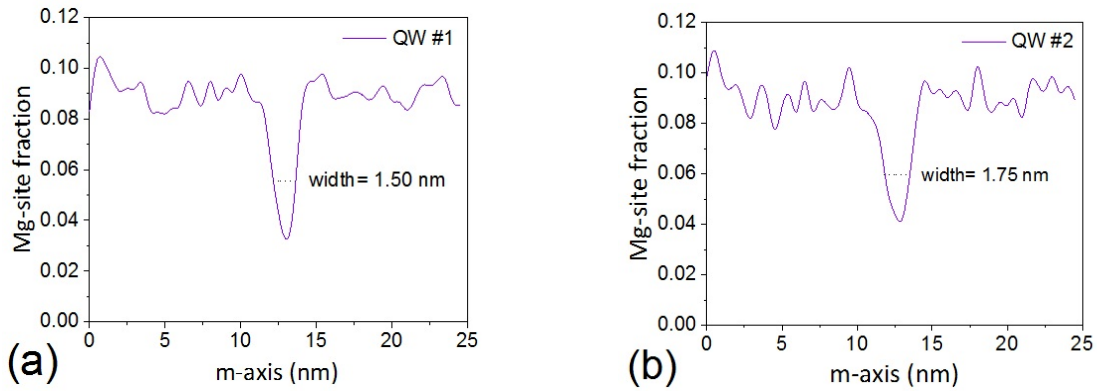


Figure 5.11: *Mg* II-site fraction profiles measured along the *m*-axis direction evaluated in a volume of $(6 \times 30 \times 25) \text{ nm}^3$. The FWHM of each minimum peak detected corresponds to the thickness of the related QW. The analysis were performed by Pradip Dalapati.

Barrier	Mg-site fraction
#1	0.087 ± 0.008
#2	0.085 ± 0.008
#3	0.087 ± 0.008
#4	0.087 ± 0.008
#5	0.089 ± 0.008
#6	0.091 ± 0.009
#7	0.088 ± 0.008

Table 5.4: The Mg II-site fraction evaluated as the profiles in figure 5.10.

QW	FWHM (nm)
#1	1.48 ± 0.13
#2	1.8 ± 0.2
#3	1.97 ± 0.16
#4	2.00 ± 0.14
#5	2.8 ± 0.3
#6	2.07 ± 0.13
#7	2.94 ± 0.15

Table 5.5: The QWs size, evaluated by the Mg II-site fraction profiles in figure 5.11.

evaluated by the APT reconstruction can be compared with the Mg II-site fraction, deduced by the signal of the $MgZnO$ barrier in the PL spectra related to the tip A2.

5.2.3 μPL analysis

Before introducing the PL experimental results, we remind that the μPL spectroscopy was carried out on tip A2 and tip A3, illuminated with a UV 260 nm laser focused on a spot size of $\approx 1\mu m$. The laser repetition rate was 0.5 MHz and the laser power was 600 μW . The specimens temperature T_{base} was kept at 80 K. In the next subparagraphs the data collected and the reported spectra are all referred to the tip A2.

5.2.3.1 Spectra before the evaporation of the sample

The PL spectra in figure 5.4 were acquired at $V_{DC} = 0$ kV. In these spectra, fig. 5.4, the signals related to each component of the $ZnO/MgZnO$ heterostructure are present: the peak of the ZnO substrate is at ≈ 3.36 eV, the signal of the QWs is at ≈ 3.44 eV and the signal associated to the $Mg_xZn_{1-x}O$ barriers is at ≈ 3.51 eV. If we compare the Mg -concentration, $x_{Mg} = (0.08 \pm 0.03)$, evaluated by the μPL spectrum, without bias applied, and the Mg -concentration evaluated by the Mg -concentration profile, $x_{Mg} = (0.088 \pm 0.025)$, in the 3D-APT reconstruction, we can conclude that these two values are consistent.

For the tip A2, the evaporation flux corresponding to a detection rate of $\varphi =$

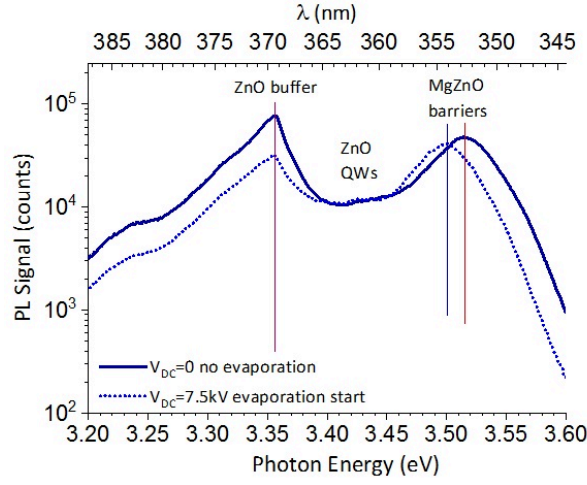


Figure 5.12: PL spectra collected at the beginning of the “*in-situ*” μPL -APT analysis. The blue curve is the signal of the tip A2, probed without bias and the dotted blue line is referred to the tip A2 at the beginning of the evaporation ($V_{DC} = 7.5 \text{ kV}$).

$0.0025 \text{ ions/pulse}$ started at $V_{DC} = 7.5 \text{ kV}$ and the PL-spectrum acquired at this V_{DC} bias corresponds to the dotted curve, in figure 5.12. The two spectra reported in figure 5.12, respectively at $V_{DC} = 0 \text{ kV}$ and $V_{DC} = 7.5 \text{ kV}$ were normalized at the same integration time and, as we can observe, the spectrum acquired at $V_{DC} = 7.5 \text{ kV}$ shows *red-shift* ($\Delta E = 15 \text{ meV}$) of the signals related to the $MgZnO$ barriers. This behavior should be related to the effect of the hydrostatic tensile stress on the apex of the APT-tip induced by the applied high electric field ($\approx 10 \div 100 \text{ V/nm}$), as demonstrated in ref. [57]. In order to verify this hypothesis, it is important to look at the trend of all the spectra during the analysis of the tip. Differently from the peaks related to the barriers and the ZnO substrate, the signal related to the ZnO QWs increases its intensity at the beginning of the evaporation process. In the next section, the evolution of the PL signal is carried forward until the complete evaporation of the heterostructure.

5.2.3.2 Spectra during the evaporation of the sample

Once the evaporation of the APT-specimen begins, the detection rate is fixed at $\varphi = 0.0025 \text{ ions/pulse}$ and the V_{DC} bias is automatically balanced by the APT software, in

order to keep constant the selected detection rate value.

The spectra reported in figure 5.13 show the optical signature related to the components which constitute the tip A2, during the ongoing evaporation process. Each spectrum (S_i) was collected at the same integration time ($\Delta t_{acquisition} = 150$ s) and at the end of the acquisition of one PL spectrum a new one was acquired.

The spectra reported in figure 5.13 show the trend of all the components present in the

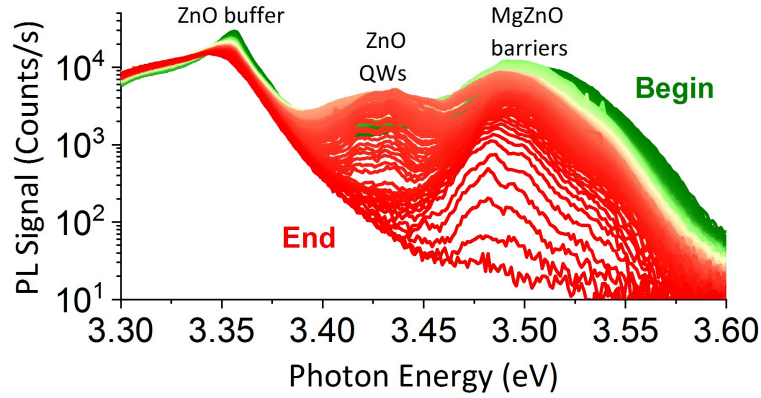


Figure 5.13: Series of spectra, detected during the μPL -APT analysis of the tip A2, where the spectral components progressively disappear due to the evaporation of the tip.

$ZnO/MgZnO$ heterostructure from the beginning of the evaporation process (pointed out by the green spectrum, labeled as ‘Begin’) until the end of the evaporation of the last barrier of the $ZnO/MgZnO$ heterostructure (pointed out by the red spectrum, labeled as ‘End’). As we can observe, the evolution of the signals related to the barriers and the ZnO substrate show again a clear shift of their peaks towards lower energy, in agreement with the *red-shift* observed, for the $MgZnO$ -barrier peak, in the spectra 5.12, from $V_{DC} = 0$ kV to $V_{DC} = 7.5$ kV. During the evaporation of the APT specimen, figure 5.13, also the signal related to the QWs shows a shift towards lower energy, but, as already observed in figure 5.12, the intensity of the QWs peak increases and decreases during the ongoing evaporation from a QW to the next one. This behavior is supposed to be related either to the specific position of the evaporated QW inside the nanoneedle or to the shape of the APT-specimen, on which depend the direction

of the emitted light, that can be more or less efficiently collected by the spectrometer, giving spectra of different intensity. Anyway, the present assumption needs additional experimental proofs. The modifications in the spectral series may be investigated by direct comparison of different spectra, as reported in figure 5.13, but also by defining differential spectra $\Delta S_{i,i+1} = S_i - S_{i+1}$, which is particularly useful in the present case, as shown by the 2D map in figure 5.14(a). The 2D maps in figure 5.14 have reported on

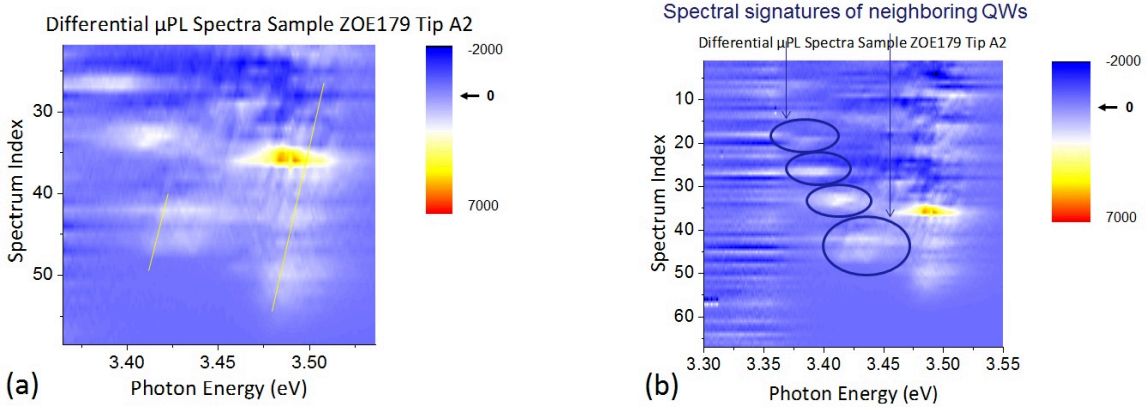


Figure 5.14: Differential spectra represented in a 2D color-map. (a) The *red-shift* of the signals related to the QWs and barriers are highlighted by the two yellow lines. (b) The optical signatures of 1 over 4 QWs are highlighted by the blue circles.

the ordinate-axis the index related to the spectrum $S(i)$ considered and on the abscissa-axis the emission photon energy, associated to each component of the $ZnO/MgZnO$ heterostructure. The two yellow diagonal lines, which appear in the 2D map, fig. 5.14(a), highlight the *red-shift* of:

- the barriers $\Delta E \approx [3.455; 3.51]eV$;
- one QW signal $\Delta E \approx [3.41; 3.43]eV$;

during the acquisition from the spectrum #20 until the spectrum #60 along the ongoing evaporation of the sample. While, in figure 5.14(b), the differential emission signals related to different QWs are circled. Each QW starts to emit at a different energy position, which depends on its thickness and the related excitonic transition. If we

look at the signal of each QW, inside each circle, in figure 5.14(b), a *red-shift* of the QW, during the evaporation process is observed. The possibility to distinguish the signal of neighboring QWs asks a spatial resolution that overlaps the μPL diffraction limit (laser spot size $\approx 1\mu m$), since, as estimated above, each QW is separated by a barrier in the tip A2 with approximately constant thickness $t_{barrier} \approx 45\text{ nm}$. These data are better clarified in the next section, correlating the μPL results with the APT 3D-reconstruction of the sample.

5.3 Interpretation of the correlated results

The notes written down, during the analysis protocol, were used to perform a corrected correlation of the experimental results.

The plots in figure 5.15 completely summarize the results that derive by the correlation of the elaborated data. In figure 5.15(a) are reported two PL spectra which were acquired respectively: at the beginning of the μPL analysis, labeled as ‘S(0)’, since it is acquired without any bias, and then the spectrum ‘S(58)’ which was acquired after the evaporation of the QW#1 or the beginning of the barrier#1, which are the closest to the ZnO substrate. Comparing the spectra S(0) and S(58), the signals of the ZnO substrate, peaked at $E \approx 3.36\text{ eV}$, and the $MgZnO$ barrier, peaked at $E \approx 3.51\text{ eV}$, show both a similar energy *red-shift* of -30 meV and -33 meV , respectively, that is supposed to be related to the effect of the induced tensile uniaxial stress, as it will be proven in the next subsection. Between the ZnO and $MgZnO$ peaks, the spectrum ‘S(0)’ shows also the signal related to the QWs, while in the spectrum ‘S(58)’ the QW signal disappear, since they were all evaporated, in agreement with the correlated information given by the APT-data.

In fig. 5.15(b), the 2D color map is a different representation of the complete serie of collected μPL spectra reported in figure 5.13, where also the signal related to the QWs is clearly distinguishable, as much as the signal of the $MgZnO$ barriers and the ZnO substrate. Thanks to the direct color contrast, to follow the changement of intensity of the different components during the evaporation is easier. The series of μPL spectra clearly shows, from the top to the bottom of the 2D color map, the progressive

bleaching of the spectral components relative to the $Mg_{0.07}Zn_{0.93}O$ barriers and the QWs.

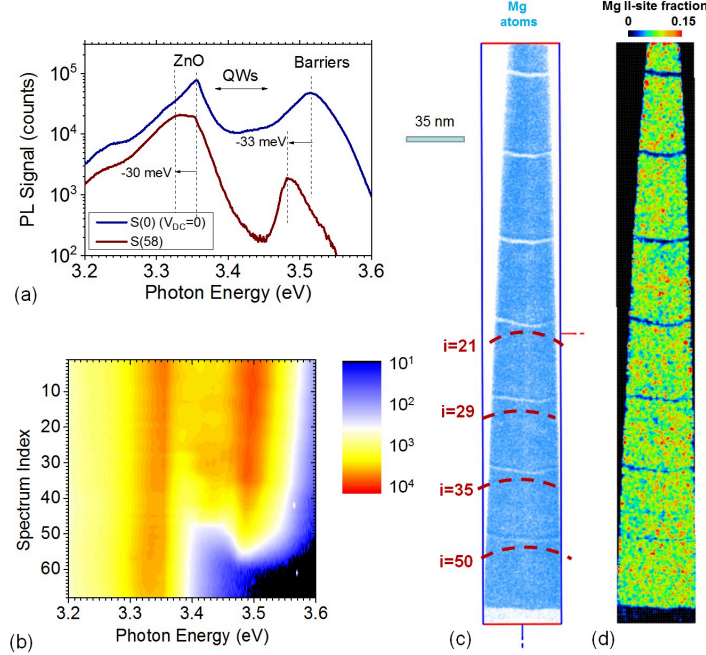


Figure 5.15: (a) μPL spectra collected at the beginning of the experiment S(0) and after the evaporation of the last quantum well S(58). The spectral contributions derive by the ZnO substrate, the QWs and by the $MgZnO$ barriers. (b) Complete serie of collected μPL spectra; (c) 3D-reconstruction of the position of Mg atoms and (d) 2D-distribution of the Mg II-site fraction, calculated over a volume of $(30 \times 30 \times 40) nm^3$. The red dashed lines indicate the approximate position of the specimen surface during the acquisition of the i - th spectrum. The separation between neighboring QWs is around $45 nm$.

We have concluded the previous section 5.2.3.2 affirming that the optical signature of the QWs, which appear in the 2D map, figure 5.14, highlighted by blue circles, shift their emission energies respect to each other, because the recombination energy of each QW depends only by its own thickness, in non-polar systems. Here, comparing the index of the spectrum which appears in the 2D map, fig. 5.14(b), and the position of the specimen surface, corresponding to a set of specific spectrum indeces, reported as a dashed red line in fig. 5.15(c), the relationship between the QWs signal position in

the 2D map, fig. 5.14(b), and their morphology, reconstructed by the APT-data, in fig. 5.15(c) and (d), is showed to be strictly related. In the table 5.4, the thickness of each reconstructed QW is reported. Comparing the 2D map, fig. 5.14(b), and the APT 3D-reconstruction, fig. 5.15(c), we can associate to each circle a QW in a precise position inside the specimen. In particular, the circles in the 2D map highlight the signatures of the QW#1 to#4 and the average emission energy that is possible to associate to each QW is in good agreement with the evaluated QW thickness, reported in the table 5.4. It is important to underline again that the interwell distance is as low as 45 nm. The $\mu PL - APT$ can thus discriminate the emission of two quantum light emitters that are much closer than the diffraction limit of the laser wavelength ($\approx 1 \mu m$), increasing in a considerable way the spatial resolution of the simple μPL system. Furthermore the value of 45 nm distance is dictated only by the specific interwell distance in the analyzed sample, so, decreasing the distance between two emitters inside the specimen, probably, a better spatial resolution can be achieved, until the spectral peaks related the two emitters do not overlap.

5.3.1 Evaluation of the stress using the bandgap deformation potential associated to the ZnO substrate

The $ZnO/MgZnO$ nanoneedle is an heterostructure composed by semiconductive materials, so the straight correlation between the observed *red-shift* and the uniaxial tensile stress, induced by the high bias applied, needs a brief explanation. In Chapter 3, in agreement with what several experimental results demonstrated, we have proved that a dielectric tip, as diamond nanoneedles, under a high electric field ($\approx 10 V/nm$) can act as a conductive material, screening the electric field at its surface. In this way, the electric field, that acts on the surface of the tip, generates a hydrostatic tensile stress on the apex of the specimen, as reported in the equation (5.4).

$$\sigma_{apex} = \frac{1}{2}\epsilon_0 F_s^2 \quad (5.4)$$

This hydrostatic stress at the apex, gradually translates in a uniaxial stress further from the apex [16, 57]. As demonstrated through the analysis on diamond nanoneedles, the intensity of the stress is proportional to the inverse cross section of the tip at the position where the emitter is located, since the mechanical tension is conservative along the axis of the tip. In an evaporating conical tip, with shank angle α , the apex radius R_{apex} linearly increases with the analyzed depth ‘ z ’, as reported in equation (5.5):

$$R(z) = R(0) + z \cdot \tan(\alpha) \quad (5.5)$$

where at $z = 0$ we set as the apex of the tip, at the beginning of the analysis. As confirmed by the charge-state-ratio of the (Zn^{2+}/Zn^+) ions detected by the APT analysis, the electric field, F_S , can be assumed nearly constant, so, in agreement with the relationship eq.(5.4) also the hydrostatic stress at the apex of the tip can be considered as constant. The uniaxial stress at depth \bar{z} generated by the field acting on the tip apex at the coordinate z evolves as in equation 5.6:

$$\sigma(z, \bar{z}) = \sigma(\bar{z}) \left(\frac{R(z)}{R(\bar{z})} \right)^2 \quad (5.6)$$

where the term \bar{z} indicates a position along the axis of the tip that is conventionally fixed. In agreement with the results obtained by diamond nanoneedles and published in the articles [57, 115], then the μPL -APT system can be used in order to perform optical piezo-spectroscopy of optically active specimens with a nanometric tip shape. In particular, once that the light emitter is localized, its photoemission signal can be used in order to measure the stress in real time, if its behavior under stress or strain is known. In this case, through all the components which constitute the $ZnO/MgZnO$ heterostructure, the bulk ZnO is the only one for which the elastic constants and the deformation potentials are known [149]. So, we can try to evaluate the uniaxial stress acting in a precise position of the tip, on the ZnO substrate, and to compare the result obtained with the *red-shift* observed in the corresponding PL spectrum. As we can observe, looking at the spectra in fig. 5.15(a), the signal of the ZnO buffer is a broad peak and in the spectrum ‘S(58)’ doesn’t look well peaked on a precise emission

energy position. The reason of such behavior can be explained considering that the laser spot size is $\approx 1 - 2 \mu m$, so the *PL* signal is collected by the whole tip, along all the experiment. Then, the emitting parts of *ZnO* closest to the tip apex generate the low-energy shoulder signal, while the parts further from the apex remain nearly unperturbed, emitting the characteristic *ZnO* bulk signal. The plot in figure 5.16(b) reports the trend of the applied DC voltage V_{DC} as a function of the analyzed depth, and thanks to the equation (5.7):

$$R(V_{DC}) = \frac{V_{DC}}{(k_f \cdot F_S)} \quad (5.7)$$

where the geometric factor k_f and the electric field F_S are given by the APT 3D reconstruction, the evolution of the apex radius during the evaporation of the tip, can be also plotted as a function of the depth. The radius seems to increase roughly linearly as a function of the analyzed depth. The linear increase of the radius with the analyzed depth was taken into account in order to calculate the uniaxial stress at $\bar{z} = 356 \text{ nm}$, the depth that corresponds to the interface between the *MgZnO* barrier and the *ZnO* buffer and to compare it with the one observed by the *red-shift* of the *ZnO* peak in the spectrum ‘S(58)’.

The stress was:

1. inferred by the PL experiments;
2. evaluated by the reconstruction parameters, related to ZnO wz-crystal structure reported in table 4.3, using the relationship between the PL energy shift of the exciton types involved in the transitions, which are linearly dependent on the uniaxial strain ϵ_{zz} along the z -axis, as reported in ref. [160, 169]

As we can observe in fig. 5.16(b) the values of the uniaxial stress, calculated as in the case (1) and (2) are in fair agreement, but do not perfectly overlap.

The discrepancies can be explained considering that:

1. the shoulder signal of *ZnO* buffer can be generated by a portion of the substrate that lies at larger depth which can explain why the experimental stress results lower at the beginning of the analysis;

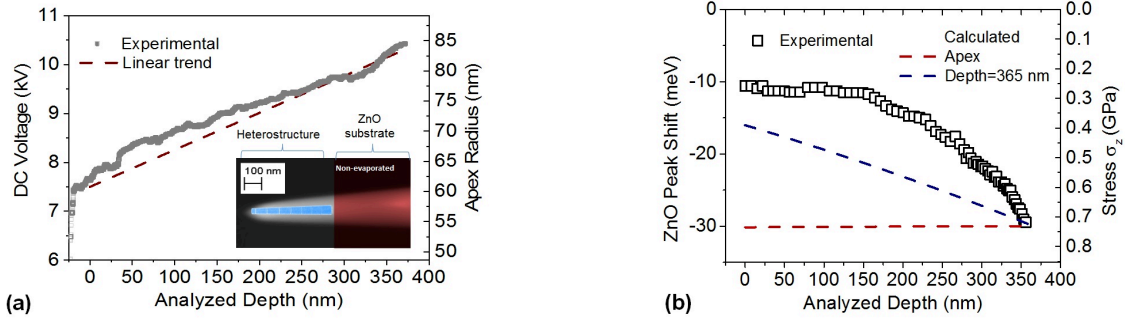


Figure 5.16: Study of the effect of the field-induced stress on the *PL* emission of the *ZnO* substrate. (a) Evolution of the DC voltage applied to the tip during the APT analysis. A linear trend curve (dashed line) is superimposed to the experimental data. In the inset the location of the reconstructed heterostructure and of the *ZnO* substrate are shown. (b) Evolution of the spectral shift of the *ZnO* peak versus the analyzed depth of the specimen. The experimental values are compared to the expected values of the stress at the tip apex and at $z = 365 \text{ nm}$, interface between *ZnO* substrate and the *MgZnO* barrier.

2. as an additional hydrostatic stress contribution to the uniaxial stress, as the the apex surface comes closer to the *ZnO* interface, generating a larger *red-shift* than a pure uniaxial stress. This should explain why the slope of the curve of the PL signal as a function of the depth, gradually increases for $z > 250 \text{ nm}$.

These results proof that through the μPL -APT system is possible to estimate the stress or strain of a specific portion of the tip during the APT analysis, as for conductive as for non-conductive specimens.

Finally, we can observe that the shift of the *ZnO* peak (-30 meV) with that of the *MgZnO* alloy (-33 meV) are comparable. Although these two phasees are not located at the same depth in the APT tip, the PL spectrum ‘S(58)’ is contiguous in the *ZnO* substrate. It can be qualitatively concluded that the deformation potentials in the $\text{Mg}_{0.07}\text{Zn}_{0.93}\text{O}$ alloy does not differ too much by those of bulk *ZnO*, at least in those involved in the observed *red-shift* along the $[1\bar{1}00]$ direction.

Conclusions

In this thesis the coupled “*in-situ*” La-APT/ μ PL technique was used in order to study the optical properties related to two different material systems:

1. diamond needle crystals with nanometric apex radius and different color centers;
2. specimens based on ZnO/(Mg,Zn)O MQWs heterostructures.

In order to get access to the optical information of these two different systems, the different mechanisms which generate the photoemitted signal in the two materials, under high electric field, are taken into account.

In the case of diamond nanoscale needles, the “*in-situ*” La-APT/ μ PL technique was used to study the radiative transitions of the excited color centers, allowing to attain a threefold goal:

- the measurement of stress in a nanoscale tip;
- the demonstration of contactless piezo-spectroscopy in nanoscale systems under uniaxial tensile stress;
- the measurement of the electrostatic field at the surface of a nanometric diamond needle.

The APT is not used as a nano-analysis tool but rather as a position sensor for the laser spot in order to focus it on the diamond needle crystal.

For what concerns the analysis of the ZnO/(Mg,Zn)O heterostructure, the “*in-situ*”

optical spectroscopy (μ PL) within an atom probe (APT) allows resolving spectral signatures of single quantum emitters with a spatial resolution better than the μ PL diffraction limit. Such signatures can then be correlated with their 3D reconstructed map of chemical composition, and the effect of uniaxial stress can be assessed.

The potential of the “*in-situ*” La-APT/ μ PL technique is enhanced by the possibility to use it in order to get access to the optical properties of different emitting systems. For what concerns the diamond needle crystals, the application of a high electrostatic field, at the apex of these tips, induces an energy splitting of the photoluminescence lines of color centers. The trend of the energy splitting of the ZPL of the NV⁰ color center was found to scale with the square of the voltage applied to the needle, which we interpreted as due to the electrostatic stress developed as a consequence of the interaction between the free holes accumulating at the needle apex and the applied field. The diamond nanotips, probed in this way, have also been scanned along the *z-axis* (length of the tip), which corresponds to the $\langle 001 \rangle$ crystal direction, from the apex position until $\sim 25 \mu\text{m}$ toward the base. Furthermore, applying the DC bias of 16 kV, in a region close to the apex of the tips, it was possible to perform polarization-resolved analysis of the NV⁰ peaks. This stress, hydrostatic at the very needle apex, rapidly evolves to a uniaxial tensile stress along the needle shank. Stresses up to 7 GPa could be estimated accordingly to the model in the proximity of the needle apex. This study constitutes the first experimental quantitative, contactless assessment of the stress building up inside a field emitter as a consequence of the application of a high voltage at its apex. The results obtained for diamond should be reproducible for any material or nanoscale system exhibiting a stress-dependent optical signature: color centers in other ionic crystals, quantum dots, quantum wells and near band-edge emissions in ultra-high crystalline quality semiconductor nanowires should exhibit stress-related modifications of their spectral properties. Such possibilities are also interesting in view of nanoscale piezospectroscopic studies exploiting the stress field as a parameter for the investigation of the symmetries of the optically active electron states, which could yield original information in the domain of quantum cryptography and information. In this study the symmetry of the NV⁰ center was confirmed by piezo-spectroscopic polarization-resolved analysis, through μ PL.

These results suggest that field-emission tip specimens with known mechanical and geometrical parameters could be used as optical sensors of intense electrostatic field in scanning probe microscopes. Furthermore, these experiments provided a validation of the model according to which the surface of dielectric needle specimens metallized under high positive fields because free holes accumulate at the apex surface, providing efficient screening of the applied field and preventing from its penetration in the interior of the material. The contactless piezo-spectroscopy was performed also on the color center at 2.65 eV, in order to prove that this color center could be also a better candidate than the NV⁰ for the fabrication of strain mediated coupling systems. By contactless piezo-spectroscopy the strain sensitivity of this color center is compared with that of the NV⁰ center. The energy splitting of the center at 2.65 eV was also found scaling linearly with the uniaxial tensile stress along the <001> direction. At the same value of stress, the energy splitting of the center at 2.65 eV is twice than the one of NV⁰. Polarization-resolved μ PL measurements of the 2.65 eV center, for diamond tips with crystal axis along the <001> crystalline direction, were also performed, under strain field. Despite the complete polarization-resolved PL study, the symmetry of this color center does not correspond to anyone reported in the literature. So, regarding the symmetry of the 2.65 eV center, further studies are needed in order understand its nature. These measurements on the NV⁰ and 2.65 eV center were performed in the UV range of exciting wavelength. Piezo-spectroscopic studies in the IR-range on the 2.65 eV color center could open more interesting perspectives about the application of this color center as stress-field sensor. Finally, preliminary findings about the temporal dynamic of the recombination process assessed through TRPL shown that the decay time of the NV⁰ centers seems to decrease from the apex of the diamond tip towards its base and also as a function of the induced stress. Anyway, further studies are needed.

The analysis performed on the ZnO/(Mg,Zn)O through the *in-situ* μ PL-APT system were used to correlate the APT 3D-reconstruction and the PL emission, to evaluate the Mg II-site fraction “ $x_{Mg} = 0.07$ ” by the position of the peak related to the MgZnO in the PL spectrum and to attribute an average emission energy to each QW, making the coupled μ PL-APT a super-resolution technique with a spatial resolution of ≈ 45 nm, where such distance is related just to the interwell distance of the specimen analyzed.

It is reasonable to think that in further studies this spatial resolution can decrease the scale, if the interwell distance between the two emitters decreases and their signal do not significantly overlaps. The μ PL data related to the ZnO/MgZnO heterostructure were used to measure the stress in real time for a specific depth, provided that, by the correlation with the APT-analysis, the light emitter is localized and its behavior under stress or strain is known. In particular, the attention was focused on the emission from the ZnO, for which the deformation potentials were known from past works in literature [149], in order to use them to infer the stress with the PL spectral shift of the ZnO peak. The uniaxial stress was calculated at the depth of the interface between the ZnO substrate and the MgZnO barrier. Although these two phases are not located at the same depth, the portion of barrier producing the PL signal, at the depth corresponding to their interface, is contiguous to the ZnO substrate, and the stress experienced by it should not be too different. It can be qualitatively concluded that the deformation potentials in $Mg_{0.07}Zn_{0.93}O$ should not differ too much from those of ZnO, at least in those involved in the red shift for uniaxial stress along the length-axial direction of the tip, which corresponds to the $[1\bar{1}00]$ direction.

The study of polarization-dependence near-band-edge PL transition in ZnO strain-free nanowires is known by literature [170] and it is in agreement with the symmetry of the excitonic transitions in wurtzite semiconductor crystals, as reported in ref. [171]. Going further, polarization-resolved μ PL measurements of the ZnO/MgZnO heterostructure, under strain-field could be a new and interesting study in order to discover if the induced stress-field changes the symmetry of the excitonic transitions related to the ZnO QWs and the MgZnO barriers.

Bibliography

- [1] E. Di Russo, *Study of the physical mechanisms leading to compositional biases in atom probe tomography of semiconductors*. Thèse de doctorat, Université de Rouen, 2018.
- [2] D. Bluvstein, Z. Zhang, and A. C. B. Jayich, “Identifying and Mitigating Charge Instabilities in Shallow Diamond Nitrogen-Vacancy Centers,” *Physical Review Letters*, vol. 122, p. 076101, Feb. 2019.
- [3] G. Davies and M. F. Hamer, “Optical studies of the 1.945 eV vibronic band in diamond,” *Proceedings of the Royal Society A: Mathematical, Physical and Engineering Sciences*, vol. 348, no. 1653, pp. 285–298, 1976.
- [4] G. Davies, C. Foy, and K. O’Donnell, “The TR12 vibronic band in diamond,” vol. 14, no. 28, pp. 4153–4165.
- [5] K. Iakoubovskii and G. J. Adriaenssens, “Optical study of some interstitial-related centres in CVD diamond,” vol. 181, no. 1, pp. 59–64.
- [6] K. Iakoubovskii, G. Adriaenssens, N. Dogadkin, and A. Shiryaev, “Optical characterization of some irradiation-induced centers in diamond,” vol. 10, no. 1, pp. 18–26.
- [7] F. J. McClung and R. W. Hellwarth, “Giant Optical Pulsations from Ruby,” *Journal of Applied Physics*, vol. 33, pp. 828–829, Mar. 1962.
- [8] G. Smith, “The early laser years at Hughes Aircraft Company,” *IEEE Journal of Quantum Electronics*, vol. 20, pp. 577–584, June 1984.

- [9] W. E. Lamb, “Theory of an Optical Maser,” *Physical Review*, vol. 134, pp. A1429–A1450, June 1964.
- [10] L. E. Hargrove, R. L. Fork, and M. A. Pollack, “Locking of He-Ne Laser Modes Induced by Synchronous Intracavity Modulation,” *Applied Physics Letters*, vol. 5, pp. 4–5, July 1964.
- [11] L. Porrès, A. Holland, L.-O. Palsson, A. P. Monkman, C. Kemp, and A. Beeby, “Absolute measurements of photoluminescence quantum yields of solutions using an integrating sphere,” *Journal of Fluorescence*, vol. 16, pp. 267–272, Mar. 2006.
- [12] A. R. Henderson, “Fabry-Perot interferometers. G. Hernandez,” *Optics Laser Technology*, vol. 18, pp. 274–274, Oct. 1986.
- [13] C. Kammerer, G. Cassaboïs, C. Voisin, M. Perrin, C. Delalande, P. Roussignol, and J. M. Gèrard, “Interferometric correlation spectroscopy in single quantum dots,” *Applied Physics Letters*, vol. 81, pp. 2737–2739, Sept. 2002.
- [14] R. Bell, “Introductory Fourier Transform Spectroscopy - 1st Edition,” Dec. 2012.
- [15] V. F. Lefebvre W. and S. X., *Atom Probe Tomography: Put Theory Into Practice*. Academic Press, May 2016.
- [16] E. P. Silaeva, L. Arnoldi, M. L. Karahka, B. Deconihout, A. Menand, H. J. Kreuzer, and A. Vella, “Do Dielectric Nanostructures Turn Metallic in High-Electric dc Fields?,” *Nano Letters*, vol. 14, pp. 6066–6072, Nov. 2014.
- [17] E. P. Silaeva, J. Houard, A. Hideur, G. Martel, and A. Vella, “Field evaporation of semiconductors assisted by nonequilibrium phonon excitations,” *Physical Review B*, vol. 92, p. 195307, Nov. 2015.
- [18] L. J. Lauhon, P. Adusumilli, P. Ronsheim, P. L. Flaitz, and D. Lawrence, “Atom-Probe Tomography of Semiconductor Materials and Device Structures,” *MRS Bulletin*, vol. 34, pp. 738–743, Oct. 2009.

- [19] C. Oberdorfer, P. Stender, C. Reinke, and G. Schmitz, “Laser-Assisted Atom Probe Tomography of Oxide Materials,” *Microscopy and Microanalysis*, vol. 13, pp. 342–346, Oct. 2007.
- [20] K. Thompson, R. Alvis, and D. Lawrence, “IBM: P. Ronsheim, P. Flaitz, J. McMurray, C. Molella, C. Parks,” p. 24, 2006.
- [21] E. W. Müller and K. Bahadur, “Field Ionization of Gases at a Metal Surface and the Resolution of the Field Ion Microscope,” *Physical Review*, vol. 102, pp. 624–631, May 1956.
- [22] E. R. McMullen and J. P. Perdew, “Theory of field evaporation of the surface layer in jellium and other metals,” *Physical Review B*, vol. 36, pp. 2598–2606, Aug. 1987.
- [23] E. R. McMullen, J. P. Perdew, and J. H. Rose, “Effects of an intense electric field on metal surface geometry,” *Solid State Communications*, vol. 44, pp. 945–949, Nov. 1982.
- [24] H. J. Kreuzer and K. Nath, “Field evaporation,” *Surface Science*, vol. 183, pp. 591–608, May 1987.
- [25] F. Vurpillot and C. Oberdorfer, “Modeling Atom Probe Tomography: A review,” *Ultramicroscopy*, vol. 159, pp. 202–216, Dec. 2015.
- [26] F. Djurabekova, S. Parviainen, A. Pohjonen, and K. Nordlund, “Atomistic modeling of metal surfaces under electric fields: Direct coupling of electric fields to a molecular dynamics algorithm,” *Physical Review E*, vol. 83, p. 026704, Feb. 2011.
- [27] M. Wada, “On the thermally activated field evaporation of surface atoms,” *Surface Science*, vol. 145, pp. 451–465, Oct. 1984.
- [28] K. Chibane and R. G. Forbes, “The temperature dependence of evaporation field for Gomer-type field-evaporation mechanisms,” *Surface Science*, vol. 122, pp. 191–215, Nov. 1982.

- [29] T. F. Kelly, A. Vella, J. H. Bunton, J. Houard, E. P. Silaeva, J. Bogdanowicz, and W. Vandervorst, “Laser pulsing of field evaporation in atom probe tomography,” *Current Opinion in Solid State and Materials Science*, vol. 18, pp. 81–89, Apr. 2014.
- [30] A. Sommerfeld, “Mathematische Theorie der Diffraction | SpringerLink.”
- [31] A. Vella, “On the interaction of an ultra-fast laser with a nanometric tip by laser assisted atom probe tomography: a review,” *Ultramicroscopy*, vol. 132, pp. 5–18, Sept. 2013.
- [32] G.-H. Ding, C. T. Chan, Z. Q. Zhang, and P. Sheng, “Resonance-enhanced optical annealing of silicon nanowires,” *Physical Review B*, vol. 71, p. 205302, May 2005.
- [33] M. K. Miller, *Atom Probe Tomography: Analysis at the Atomic Level*. Springer Science & Business Media, Dec. 2012. Google-Books-ID: E0_aBwAAQBAJ.
- [34] A. Cerezo, T. J. Godfrey, C. R. M. Grovenor, M. G. Hetherington, R. M. Hoyley, J. P. Jakubovics, J. A. Liddle, G. D. W. Smith, and G. M. Worrall, “Materials analysis with a position-sensitive atom probe,” *Journal of Microscopy*, vol. 154, no. 3, pp. 215–225, 1989.
- [35] G. Schmitz, “Nanoanalysis by Atom Probe Tomography,” in *Nanotechnology*, pp. 213–257, American Cancer Society, 2010.
- [36] F. Vurpillot, B. Gault, B. P. Geiser, and D. J. Larson, “Reconstructing atom probe data: A review,” *Ultramicroscopy*, vol. 132, pp. 19–30, Sept. 2013.
- [37] C. M. C. d. Castilho, “Ion trajectories in atom probe field ion microscopy and gas field ion sources,” *Journal of Physics D: Applied Physics*, vol. 32, pp. 2261–2265, Aug. 1999.
- [38] G. Da Costa, F. Vurpillot, A. Bostel, M. Bouet, and B. Deconihout, “Design of a delay-line position-sensitive detector with improved performance,” *Review of Scientific Instruments*, vol. 76, p. 013304, Dec. 2004.

- [39] Y. C. Chen and D. N. Seidman, “On the atomic resolution of a field ion microscope,” *Surface Science*, vol. 26, pp. 61–84, June 1971.
- [40] B. Gault, M. Muller, A. La Fontaine, M. P. Moody, A. Shariq, A. Cerezo, S. P. Ringer, and G. D. W. Smith, “Influence of surface migration on the spatial resolution of pulsed laser atom probe tomography,” *Journal of Applied Physics*, vol. 108, p. 044904, Aug. 2010.
- [41] M. P. Moody, A. V. Ceguerra, A. J. Breen, X. Y. Cui, B. Gault, L. T. Stephenson, R. K. W. Marceau, R. C. Powles, and S. P. Ringer, “Atomically resolved tomography to directly inform simulations for structure-property relationships,” *Nature Communications*, vol. 5, p. 5501, Nov. 2014.
- [42] A. R. Waugh, E. D. Boyes, and M. J. Southon, “Investigations of field evaporation with a field-desorption microscope,” *Surface Science*, vol. 61, pp. 109–142, Dec. 1976.
- [43] M. K. Miller, “THE EFFECTS OF LOCAL MAGNIFICATION AND TRAJECTORY ABERRATIONS ON ATOM PROBE ANALYSIS,” *Le Journal de Physique Colloques*, vol. 48, pp. C6–565–C6–570, Nov. 1987.
- [44] F. Vurpillot, A. Cerezo, D. Blavette, and D. J. Larson, “Modeling Image Distortions in 3dap,” *Microscopy and Microanalysis*, vol. 10, pp. 384–390, June 2004.
- [45] D. J. Larson, B. P. Geiser, T. J. Prosa, S. S. A. Gerstl, D. A. Reinhard, and T. F. Kelly, “Improvements in planar feature reconstructions in atom probe tomography,” *Journal of Microscopy*, vol. 243, pp. 15–30, July 2011.
- [46] N. Rolland, F. Vurpillot, S. Duguay, and D. Blavette, “Dynamic evolution and fracture of multilayer field emitters in atom probe tomography: a new interpretation,” *The European Physical Journal Applied Physics*, vol. 72, p. 21001, Nov. 2015.

- [47] B. Gault, F. d. Geuser, L. T. Stephenson, M. P. Moody, B. C. Muddle, and S. P. Ringer, “Estimation of the Reconstruction Parameters for Atom Probe Tomography,” *Microscopy and Microanalysis*, vol. 14, pp. 296–305, Aug. 2008.
- [48] T. M. Smeeton, M. J. Kappers, J. S. Barnard, M. E. Vickers, and C. J. Humphreys, “Electron-beam-induced strain within InGaN quantum wells: False indium “cluster” detection in the transmission electron microscope,” *Applied Physics Letters*, vol. 83, pp. 5419–5421, Dec. 2003.
- [49] R. Agrawal, R. A. Bernal, D. Isheim, and H. D. Espinosa, “Characterizing Atomic Composition and Dopant Distribution in Wide Band Gap Semiconductor Nanowires Using Laser-Assisted Atom Probe Tomography,” *The Journal of Physical Chemistry C*, vol. 115, pp. 17688–17694, Sept. 2011.
- [50] M. Karahka and H. J. Kreuzer, “Field evaporation of oxides: A theoretical study,” *Ultramicroscopy*, vol. 132, pp. 54–59, Sept. 2013.
- [51] B. Gault, D. W. Saxey, M. W. Ashton, S. B. Sinnott, A. N. Chiaramonti, M. P. Moody, and D. K. Schreiber, “Behavior of molecules and molecular ions near a field emitter,” *New Journal of Physics*, vol. 18, p. 033031, Mar. 2016.
- [52] F. De Geuser, B. Gault, A. Bostel, and F. Vurpillot, “Correlated field evaporation as seen by atom probe tomography,” *Surface Science*, vol. 601, no. 2, pp. 536 – 543, 2007.
- [53] D. W. Saxey, “Correlated ion analysis and the interpretation of atom probe mass spectra,” *Ultramicroscopy*, vol. 111, pp. 473–479, May 2011.
- [54] D. R. Kingham, “The post-ionization of field evaporated ions: A theoretical explanation of multiple charge states,” *Surface Science*, vol. 116, pp. 273–301, Apr. 1982.
- [55] A. V. d. A. Neto and C. M. C. d. Castilho, “Some remarks on the Haydock-Kingham model for field ionization,” *Journal of Physics B: Atomic, Molecular and Optical Physics*, vol. 24, pp. 2609–2615, June 1991.

- [56] Z. Yang, D. Lichtenwalner, A. Morris, J. Krim, and A. I. Kingon, “Contact degradation in hot/cold operation of direct contact micro-switches,” *Journal of Micromechanics and Microengineering*, vol. 20, p. 105028, Sept. 2010.
- [57] L. Rigutti, L. Venturi, J. Houard, A. Normand, E. P. Silaeva, M. Borz, S. A. Malykhin, A. N. Obraztsov, and A. Vella, “Optical contactless measurement of electric field-induced tensile stress in diamond nanoscale needles,” vol. 17, no. 12, pp. 7401–7409.
- [58] E. Di Russo, N. Cherkashin, M. Korytov, A. E. Nikolaev, A. V. Sakharov, A. F. Tsatsulnikov, B. Bonef, I. Blum, J. Houard, G. Da Costa, D. Blavette, and L. Rigutti, “Compositional accuracy in atom probe tomography analyses performed on III-N light emitting diodes,” *Journal of Applied Physics*, vol. 126, p. 124307, Sept. 2019.
- [59] M. K. Miller, K. F. Russell, K. Thompson, R. Alvis, and D. J. Larson, “Review of Atom Probe FIB-Based Specimen Preparation Methods,” *Microscopy and Microanalysis*, vol. 13, pp. 428–436, Dec. 2007.
- [60] L. Rigutti, A. Vella, F. Vurpillot, A. Gaillard, N. Sevelin-Radiguet, J. Houard, A. Hideur, G. Martel, G. Jacopin, A. D. Luna Bugallo, and B. Deconihout, “Coupling atom probe tomography and photoluminescence spectroscopy: Exploratory results and perspectives,” *Ultramicroscopy*, vol. 132, pp. 75–80, Sept. 2013.
- [61] M. K. Miller, “Sculpting Needle-Shaped Atom Probe Specimens with a Dual Beam FIB,” *Microscopy and Microanalysis*, vol. 11, pp. 808–809, Aug. 2005.
- [62] M. Grundmann, *The physics of semiconductors: an introduction including nanophysics and applications*. Graduate texts in physics, Springer-Verlag, 2nd ed ed., 2010.
- [63] J. R. Chelikowsky and S. G. Louie, “First-principles linear combination of atomic orbitals method for the cohesive and structural properties of solids: Application to diamond,” *Physical Review B*, vol. 29, pp. 3470–3481, Mar. 1984.

- [64] C. D. Clark, P. J. Dean, P. V. Harris, and W. C. Price, "Intrinsic edge absorption in diamond," *Proceedings of the Royal Society of London. Series A. Mathematical and Physical Sciences*, vol. 277, pp. 312–329, Feb. 1964.
- [65] K. Miyoshi, "Structures and mechanical properties of natural and synthetic diamonds," p. 26.
- [66] T. S., T. K., P. Patel, F. G., and T. K., "Diamond, diamond-like carbon (DLC) and diamond-like nanocomposite (DLN) thin films for MEMS applications," in *Microelectromechanical Systems and Devices* (N. Islam, ed.), InTech.
- [67] S. B. Singh, M. Pandey, N. Chand, A. Biswas, D. Bhattacharya, S. Dash, A. K. Tyagi, R. M. Dey, S. K. Kulkarni, and D. S. Patil, "Optical and mechanical properties of diamond like carbon films deposited by microwave ECR plasma CVD," vol. 31, no. 5, pp. 813–818.
- [68] P. Hess, "The mechanical properties of various chemical vapor deposition diamond structures compared to the ideal single crystal," vol. 111, no. 5, p. 051101.
- [69] "The absorption spectra of natural and irradiated diamonds," vol. 234, no. 1198, pp. 363–381.
- [70] J. Walker, "Optical absorption and luminescence in diamond," vol. 42, no. 10, pp. 1605–1659.
- [71] J. J. Sinai and S. Y. Wu, "Lattice dynamics of isolated nitrogen in synthetic diamond," vol. 43, no. 15, pp. 12419–12424.
- [72] R. Ulbricht, S. T. van der Post, J. P. Goss, P. R. Briddon, R. Jones, R. U. A. Khan, and M. Bonn, "Single substitutional nitrogen defects revealed as electron acceptor states in diamond using ultrafast spectroscopy," vol. 84, no. 16.
- [73] S. F. Martin, "Methodology for the construction of quaternary carbon centers," vol. 36, no. 4, pp. 419–460.

- [74] V. Blank, M. Popov, G. Pivovarov, N. Lvova, and S. Terentev, “Mechanical properties of different types of diamond,” vol. 8, no. 8, pp. 1531–1535.
- [75] A. T. Collins, “The characterisation of point defects in diamond by luminescence spectroscopy,” vol. 1, no. 5, pp. 457–469.
- [76] A. S. Stepanov, A. V. Korsakov, O. P. Yuryeva, V. A. Nadolinniy, M. Perraki, K. De Gussem, and P. Vandenabeele, “Brown diamonds from an eclogite xenolith from udachnaya kimberlite, yakutia, russia,” vol. 80, no. 1, pp. 41–48.
- [77] A. M. Zaitsev, *Optical Properties of Diamond: A Data Handbook*. Springer-Verlag.
- [78] J. R. Maze, A. Gali, E. Togan, Y. Chu, A. Trifonov, E. Kaxiras, and M. D. Lukin, “Properties of nitrogen-vacancy centers in diamond: the group theoretic approach,” vol. 13, no. 2, p. 025025.
- [79] A. N. Obraztsov, P. G. Kopylov, A. L. Chuvilin, and N. V. Savenko, “Production of single crystal diamond needles by a combination of CVD growth and thermal oxidation,” vol. 18, no. 10, pp. 1289–1293.
- [80] P. G. Kopylov, A. N. Obraztsov, M. A. Dolganov, and S. S. Abramchuk, “Formation of pyramidal shaped single crystal diamonds in chemical vapor deposition,” vol. 45, no. 5, pp. 553–557.
- [81] A. A. Zolotukhin, M. A. Dolganov, A. M. Alekseev, and A. N. Obraztsov, “Single-crystal diamond microneedles shaped at growth stage,” vol. 42, pp. 15–20.
- [82] A. Zolotukhin, P. G. Kopylov, R. R. Ismagilov, and A. N. Obraztsov, “Thermal oxidation of CVD diamond,” vol. 19, no. 7, pp. 1007–1011.
- [83] M. W. Doherty, N. B. Manson, P. Delaney, F. Jelezko, J. Wrachtrup, and L. C. Hollenberg, “The nitrogen-vacancy colour centre in diamond,” vol. 528, no. 1, pp. 1–45.

- [84] N. B. Manson, J. P. Harrison, and M. J. Sellars, “Nitrogen-vacancy center in diamond: Model of the electronic structure and associated dynamics,” vol. 74, no. 10.
- [85] H. Sternschulte, K. Thonke, R. Sauer, P. C. MÃEnzinger, and P. Michler, “1.681-eV luminescence center in chemical-vapor-deposited homoepitaxial diamond films,” vol. 50, no. 19, pp. 14554–14560.
- [86] A. Gali and J. R. Maze, “*Ab initio* study of the split silicon-vacancy defect in diamond: Electronic structure and related properties,” *Physical Review B*, vol. 88, Dec. 2013.
- [87] L. J. Rogers, K. D. Jahnke, M. W. Doherty, A. Dietrich, L. P. McGuinness, C. MÃEller, T. Teraji, H. Sumiya, J. Isoya, N. B. Manson, and F. Jelezko, “Electronic structure of the negatively charged silicon-vacancy center in diamond,” vol. 89, no. 23.
- [88] S. A. Malykhin, R. R. Ismagilov, F. T. Tuyakova, E. A. Obraztsova, P. V. Fedotov, A. Ermakova, P. Siyushev, K. G. Katamadze, F. Jelezko, Y. P. Rakovich, and A. N. Obraztsov, “Photoluminescent properties of single crystal diamond microneedles,” vol. 75, pp. 49–55.
- [89] F. T. Tuyakova, E. A. Obraztsova, E. V. Korostylev, D. V. Klinov, K. A. Prusakov, A. A. Alekseev, R. R. Ismagilov, and A. N. Obraztsov, “Photo- and cathodo-luminescence of needle-like single crystal diamonds,” vol. 179, pp. 539–544.
- [90] N. Aslam, G. Waldherr, P. Neumann, F. Jelezko, and J. Wrachtrup, “Photo-induced ionization dynamics of the nitrogen vacancy defect in diamond investigated by single-shot charge state detection,” vol. 15, no. 1, p. 013064.
- [91] H. B. Dyer, F. A. Raal, L. Du Preez, and J. H. N. Loubser, “Optical absorption features associated with paramagnetic nitrogen in diamond,” vol. 11, no. 112, pp. 763–774.

- [92] G. Davies, “Dynamic jahn-teller distortions at trigonal optical centres in diamond,” vol. 12, no. 13, pp. 2551–2566.
- [93] Y. Mita, “Change of absorption spectra in type-i *b* diamond with heavy neutron irradiation,” vol. 53, no. 17, pp. 11360–11364.
- [94] H.-Q. Zhao, M. Fujiwara, and S. Takeuchi, “Effect of substrates on the temperature dependence of fluorescence spectra of nitrogen vacancy centers in diamond nanocrystals,” vol. 51, p. 090110.
- [95] N. Manson and J. Harrison, “Photo-ionization of the nitrogen-vacancy center in diamond,” *Diamond and Related Materials*, vol. 14, pp. 1705–1710, Oct. 2005.
- [96] K. Wang, J. W. Steeds, Z. Li, and Y. Tian, “Photoluminescence studies of both the neutral and negatively charged nitrogen-vacancy center in diamond,” vol. 22, no. 1, pp. 108–112.
- [97] J. R. Weber, W. F. Koehl, J. B. Varley, A. Janotti, B. B. Buckley, C. G. Van de Walle, and D. D. Awschalom, “Quantum computing with defects,” vol. 107, no. 19, pp. 8513–8518.
- [98] N. Manson and C. Wei, “Transient hole burning in n-v centre in diamond,” *Journal of Luminescence*, vol. 58, pp. 158–160, Jan. 1994.
- [99] J. Storteboom, P. Dolan, S. Castelletto, X. Li, and M. Gu, “Lifetime investigation of single nitrogen vacancy centres in nanodiamonds,” *Optics Express*, vol. 23, no. 9, p. 11327, 2015.
- [100] F. A. Inam, M. D. W. Grogan, M. Rollings, T. Gaebel, J. M. Say, C. Bradac, T. A. Birks, W. J. Wadsworth, S. Castelletto, J. R. Rabeau, and M. J. Steel, “The jahn-teller effect and vibronic coupling at deep levels in diamond,” *Reports on Progress in Physics*, vol. 44, pp. 787–830, July 1981.
- [101] A. Gali, “Theory of the neutral nitrogen-vacancy center in diamond and its application to the realization of a qubit,” *Physical Review B*, vol. 79, June 2009.

- [102] F. A. Inam, M. D. W. Grogan, M. Rollings, T. Gaebel, J. M. Say, C. Bradac, T. A. Birks, W. J. Wadsworth, S. Castelletto, J. R. Rabeau, and M. J. Steel, “Emission and nonradiative decay of nanodiamond NV centers in a low refractive index environment,” *ACS Nano*, vol. 7, no. 5, pp. 3833–3843, 2013.
- [103] A. S. Orekhov, F. T. Tuyakova, E. A. Obraztsova, A. B. Loginov, A. L. Chuvilin, and A. N. Obraztsov, “Structural peculiarities of single crystal diamond needles of nanometer thickness,” *Nanotechnology*, vol. 27, p. 455707, Oct. 2016.
- [104] A. T. Collins, “The fermi level in diamond,” *Journal of Physics: Condensed Matter*, vol. 14, no. 14, p. 3743, 2002.
- [105] K. Iakoubovskii, G. J. Adriaenssens, and M. Nesladek, “Photochromism of vacancy-related centres in diamond,” *Journal of Physics: Condensed Matter*, vol. 12, pp. 189–199, Dec. 1999.
- [106] Y. Dumeige, F. Treussart, R. Alleaume, T. Gacoin, J.-F. Roch, and P. Grangier, “Photo-induced creation of nitrogen-related color centers in diamond nanocrystals under femtosecond illumination,” *Journal of Luminescence*, vol. 109, pp. 61–67, Aug. 2004.
- [107] K. Iakoubovskii and A. Stesmans, “Chemical vapour deposition diamond studied by optical and electron spin resonance techniques,” vol. 14, no. 17, pp. R467–R499.
- [108] T. T. Tsong, “Field penetration and band bending near semiconductor surfaces in high electric fields,” vol. 81, no. 1, pp. 28–42.
- [109] M. K. Miller, A. Cerezo, M. G. Hetherington, and G. D. W. S. FRS, *Atom Probe Field Ion Microscopy*. Monographs on the Physics and Chemistry of Materials, Oxford University Press.
- [110] S. A. Malykhin, J. Houard, R. R. Ismagilov, A. S. Orekhov, A. Vella, and A. N. Obraztsov, “Luminescent characteristics of needle-like single crystal diamonds,” vol. 255, no. 1, p. 1700189.

- [111] P. Tamarat, T. Gaebel, J. R. Rabeau, M. Khan, A. D. Greentree, H. Wilson, L. C. L. Hollenberg, S. Prawer, P. Hemmer, F. Jelezko, and J. Wrachtrup, “Stark shift control of single optical centers in diamond,” vol. 97, no. 8, p. 083002.
- [112] M. Ruhl, C. Ott, S. Gotzinger, M. Krieger, and H. B. Weber, “Controlled generation of intrinsic near-infrared color centers in 4h-SiC via proton irradiation and annealing,” *Applied Physics Letters*, vol. 113, p. 122102, Sept. 2018.
- [113] G. Wolfowicz, C. P. Anderson, A. L. Yeats, S. J. Whiteley, J. Niklas, O. G. Poluektov, F. J. Heremans, and D. D. Awschalom, “Optical charge state control of spin defects in 4h-SiC,” *Nature Communications*, vol. 8, Nov. 2017.
- [114] M. Radulaski, M. Widmann, M. Niethammer, J. L. Zhang, S.-Y. Lee, T. Rendler, K. G. Lagoudakis, N. T. Son, E. Janzèn, T. Ohshima, J. Wrachtrup, and J. Vuckovic, “Scalable Quantum Photonics with Single Color Centers in Silicon Carbide,” *Nano Letters*, vol. 17, pp. 1782–1786, Mar. 2017.
- [115] L. Venturi, L. Rigutti, J. Houard, I. Blum, S. Malykhin, A. Obraztsov, and A. Vella, “Strain sensitivity and symmetry of 2.65eV color center in diamond nanoscale needles,” vol. 114, no. 14, p. 143104.
- [116] G. Davies, “The effect of nitrogen impurity on the annealing of radiation damage in diamond,” vol. 5, no. 17, pp. 2534–2542.
- [117] K. Mohammed, G. Davies, and A. T. Collins, “Uniaxial stress splitting of photoluminescence transitions at optical centres in cubic crystals: theory and application to diamond,” vol. 15, no. 12, pp. 2779–2788.
- [118] M. Albrecht, H. P. Strunk, R. Hull, and J. M. Bonar, “Dislocation glide in {110} planes in semiconductors with diamond or zinc-blende structure,” vol. 62, no. 18, pp. 2206–2208.
- [119] L. Pizzagalli, “Stability and mobility of screw dislocations in 4h, 2h and 3c silicon carbide,” vol. 78, pp. 236–244.

- [120] D. G. Brandon and M. Wald, “The direct observation of lattice defects by field ion microscopy,” vol. 6, no. 68, pp. 1035–1044.
- [121] J. E. Field and C. S. J. Pickles, “Strength, fracture and friction properties of diamond,” vol. 5, no. 6, pp. 625–634.
- [122] J. Teissier, A. Barfuss, P. Appel, E. Neu, and P. Maletinsky, “Strain coupling of a nitrogen-vacancy center spin to a diamond mechanical oscillator,” vol. 113, no. 2, p. 020503.
- [123] E. R. MacQuarrie, M. Otten, S. K. Gray, and G. D. Fuchs, “Cooling a mechanical resonator with nitrogen-vacancy centres using a room temperature excited state spin-strain interaction,” vol. 8, p. 14358.
- [124] K. W. Lee, D. Lee, P. Ovartchaiyapong, J. Minguzzi, J. R. Maze, and A. C. Bleszynski Jayich, “Strain coupling of a mechanical resonator to a single quantum emitter in diamond,” vol. 6, no. 3, p. 034005.
- [125] P. Ovartchaiyapong, K. W. Lee, B. A. Myers, and A. C. B. Jayich, “Dynamic strain-mediated coupling of a single diamond spin to a mechanical resonator,” vol. 5, p. 4429.
- [126] H. Hanzawa, Y. Nisida, and T. Kato, “Measurement of decay time for the NV centre in ib diamond with a picosecond laser pulse,” vol. 6, no. 11, pp. 1595–1598.
- [127] K. Iakoubovskii and G. J. Adriaenssens, “Luminescence excitation spectra in diamond,” vol. 61, no. 15, pp. 10174–10182.
- [128] J. Walker, “An optical study of the TR12 and 3h defects in irradiated diamond,” vol. 10, no. 16, pp. 3031–3037.
- [129] A. Mainwood, A. T. Collins, and P. Woad, “Isotope dependence of the frequency of localized vibrational modes in diamond,” in *Defects in Semiconductors 17*, vol. 143 of *Materials Science Forum*, pp. 29–34, Trans Tech Publications, 10 1993.

- [130] B. Naydenov, R. Kolesov, A. Batalov, J. Meijer, S. Pezzagna, D. Rogalla, F. Jelezko, and J. Wrachtrup, “Engineering single photon emitters by ion implantation in diamond,” vol. 95, no. 18, p. 181109.
- [131] P. Ji, R. Balili, J. Beaumariage, S. Mukherjee, D. Snoke, and M. V. G. Dutt, “Multiple-photon excitation of nitrogen vacancy centers in diamond,” vol. 97, no. 13, p. 134112.
- [132] S. L. Jacques, “Optical properties of biological tissues: a review,” vol. 58, no. 11, pp. R37–61.
- [133] A. Dubietis, G. TamoÅjauskas, R. Å uminas, V. Jukna, and A. Couairon, “Ultra-fast supercontinuum generation in bulk condensed media (invited review),”
- [134] A. Janotti and C. G. Van de Walle, “Fundamentals of zinc oxide as a semiconductor,” *Reports on Progress in Physics*, vol. 72, p. 126501, Dec. 2009.
- [135] M. Tamargo, *II-VI Semiconductor Materials and their Applications*. Routledge, 2018.
- [136] T. L. Chu and S. S. Chu, “Thin film II-VI photovoltaics,” *Solid-State Electronics*, vol. 38, no. 3, pp. 533–549, 1995.
- [137] M.-W. Ahn, K.-S. Park, J.-H. Heo, J.-G. Park, D.-W. Kim, K. J. Choi, J.-H. Lee, and S.-H. Hong, “Gas sensing properties of defect-controlled ZnO-nanowire gas sensor,” *Applied Physics Letters*, vol. 93, p. 263103, Dec. 2008.
- [138] L. Rigutti, L. Mancini, D. Hernandez-Maldonado, W. Lefebvre, E. Giraud, R. Butte, J.-F. Carlin, N. Grandjean, D. Blavette, and F. Vurpillot, “Statistical correction of atom probe tomography data of semiconductor alloys combined with optical spectroscopy: The case of $al_{0.25}ga_{0.75}n$,” *Journal of Applied Physics*, vol. 119, no. 11, p. 105704, 2016.
- [139] M. Karaliunas, V. Sukauskas, E. Kuokstis, S.-Y. Ting, J.-J. Huang, and C.-C. Yang, “Band tail filling effect in MBE-grown ternary MgZnO epitaxial layers with high Mg content,” *Physica Status Solidi (c)*, p. 105704, Oct. 2013.

- [140] T. Makino, Y. Segawa, M. Kawasaki, and H. Koinuma, "Optical properties of excitons in ZnO-based quantum well heterostructures," *Semiconductor Science and Technology*, vol. 20, no. 4, pp. S78–S91, 2005.
- [141] H. Morkoc and U. Ozgur, *Zinc oxide: fundamentals, materials and device technology*. Wiley-VCH, 2009.
- [142] A. Dal Corso, M. Posternak, R. Resta, and A. Baldereschi, "*Ab initio* study of piezoelectricity and spontaneous polarization in ZnO," *Physical Review B*, vol. 50, pp. 10715–10721, Oct. 1994.
- [143] D. Reynolds, D. Look, and B. Jogai, "Optically pumped ultraviolet lasing from ZnO," *Solid State Communications*, vol. 99, no. 12, pp. 873–875, 1996.
- [144] S. S. Hullavarad, N. V. Hullavarad, D. E. Pugel, S. Dhar, I. Takeuchi, T. Venkatesan, and R. D. Vispute, "Homo- and hetero-epitaxial growth of hexagonal and cubic $\text{Mg}_x\text{Zn}_{1-x}\text{O}$ alloy thin films by pulsed laser deposition technique," *Journal of Physics D: Applied Physics*, vol. 40, pp. 4887–4895, Aug. 2007.
- [145] A. Ohtomo, M. Kawasaki, T. Koida, K. Masubuchi, H. Koinuma, Y. Sakurai, Y. Yoshida, T. Yasuda, and Y. Segawa, " $\text{mg}_x\text{zn}_{1-x}\text{o}$ as a II-VI widegap semiconductor alloy," *Applied Physics Letters*, vol. 72, no. 19, pp. 2466–2468, 1998.
- [146] A. Redondo-Cubero, A. Hierro, J.-M. Chauveau, K. Lorenz, G. Tabares, N. Franco, E. Alves, and E. Munoz, "Single phase a-plane MgZnO epilayers for UV optoelectronics: substitutional behaviour of mg at large contents," *Cryst. Eng. Comm*, vol. 14, pp. 1637–1640, Feb. 2012.
- [147] S. W. H. Eijt, J. de Roode, H. Schut, B. J. Kooi, and J. T. M. De Hosson, "Formation and stability of rocksalt ZnO nanocrystals in MgO," *Applied Physics Letters*, vol. 91, p. 201906, Nov. 2007.
- [148] B. Laumer, F. Schuster, M. Stutzmann, A. Bergmaier, G. Dollinger, and M. Eickhoff, "Accurate determination of optical bandgap and lattice parameters of $\text{zn}_{1-x}\text{mg}_x\text{o}$ epitaxial films ($0 < x < 0.3$) grown by plasma-assisted molecular beam

epitaxy on a-plane sapphire,” *Journal of Applied Physics*, vol. 113, p. 233512, June 2013.

- [149] W. J. Fan, J. B. Xia, P. A. Agus, S. T. Tan, S. F. Yu, and X. W. Sun, “Band parameters and electronic structures of wurtzite ZnO and ZnO/MgZnO quantum wells,” *Journal of Applied Physics*, vol. 99, pp. 13–72, Jan. 2006.
- [150] J.-M. Chauveau, J. Vives, J. Zuniga-Perez, M. Laugt, M. Teisseire, C. Deparis, C. Morhain, and B. Vinter, “Residual strain in nonpolar a-plane Zn_{1-x}Mg_xO (0,” *Applied Physics Letters*, vol. 93, p. 231911, Dec. 2008.
- [151] H. Matsui, N. Hasuike, H. Harima, and H. Tabata, “Growth evolution of surface nanowires and large anisotropy of conductivity on MgZnO/ZnO quantum wells based on M-nonpolar (10-10) ZnO,” *Journal of Applied Physics*, vol. 104, p. 094309, Nov. 2008.
- [152] Y. Hu, H. Zeng, J. Du, Z. Hu, and S. Zhang, “The structural, electrical and optical properties of Mg-doped ZnO with different interstitial Mg concentration,” *Materials Chemistry and Physics*, vol. 182, pp. 15–21, Oct. 2016.
- [153] W.-R. Liu, W.-L. Huang, Y.-C. Wu, L.-H. Lai, C.-H. Hsu, W.-F. Hsieh, T.-H. Chiang, H. W. Wan, M. Hong, and J. Kwo, “Correction to Exciton Localization of High-Quality ZnO/Mg_xZn_{1-x}O Multiple Quantum Wells on Si (111) with a Y₂O₃ Buffer Layer,” *ACS Applied Nano Materials*, vol. 1, pp. 5958–5958, Oct. 2018.
- [154] M. Al-Suleiman, A. El-Shaer, A. Bakin, H.-H. Wehmann, and A. Waag, “Optical investigations and exciton localization in high quality Zn_{1-x}Mg_xO-ZnO single quantum wells,” *Applied Physics Letters*, vol. 91, p. 081911, Aug. 2007.
- [155] Z. L. Liu, Z. X. Mei, R. Wang, J. M. Zhao, H. L. Liang, Y. Guo, A. Y. Kuznetsov, and X. L. Du, “Alloy-fluctuation-induced exciton localization in high-mg-content (0.27 ≤ x ≤ 0.55) wurtzite $mg_xzn_{1-x}o$ epilayers,” *Journal of Physics D: Applied Physics*, vol. 43, no. 28, p. 285402, 1995.

- [156] W.-R. Liu, W.-L. Huang, Y.-C. Wu, L.-H. Lai, C.-H. Hsu, W.-F. Hsieh, T.-H. Chiang, H. W. Wan, M. Hong, and J. Kao, “Exciton Localization of High-Quality ZnO/MgxZn1-xO Multiple Quantum Wells on Si (111) with a Y2o3 Buffer Layer,” *ACS Applied Nano Materials*, vol. 1, pp. 3829–3836, Aug. 2018.
- [157] T. B. Bateman, “Elastic Moduli of Single-Crystal Zinc Oxide,” *Journal of Applied Physics*, vol. 33, pp. 3309–3312, Nov. 1962.
- [158] R. Ahuja, L. Fast, O. Eriksson, J. M. Wills, and B. Johansson, “Elastic and high pressure properties of ZnO,” *Journal of Applied Physics*, vol. 83, pp. 8065–8067, May 1998.
- [159] X. Wang, Y. Gu, X. Sun, H. Wang, and Y. Zhang, “Third-order elastic constants of ZnO and size effect in ZnO nanowires,” *Journal of Applied Physics*, vol. 115, p. 213516, June 2014.
- [160] J. E. Rowe, M. Cardona, and F. H. Pollak, “Valence band symmetry and deformation potentials of ZnO,” *Solid State Communications*, vol. 6, pp. 239–242, Apr. 1968.
- [161] G. L. Bir, G. E. Pikus, P. Shelnitz, and D. Louvish, *Symmetry and strain-induced effects in semiconductors*. Wiley ; Israel Program for Scientific Translations ; Distributed by Wiley, 1976.
- [162] T. B. Bahder, “Eight-band $\mathbf{k} \cdot \mathbf{p}$ model of strained zinc-blende crystals,” *Physical Review B*, vol. 41, pp. 11992–12001, June 1990.
- [163] S.-H. Wei and A. Zunger, “Predicted band-gap pressure coefficients of all diamond and zinc-blende semiconductors: Chemical trends,” *Physical Review B*, vol. 60, pp. 5404–5411, Aug. 1999.
- [164] L. Beaur, T. Bretagnon, B. Gil, A. Kavokin, T. Guillet, C. Brimont, D. Tainoff, M. Teisseire, and J.-M. Chauveau, “Exciton radiative properties in nonpolar homoepitaxial ZnO/(Zn,Mg)O quantum wells,” *Physical Review B*, vol. 84, p. 165312, Oct. 2011.

- [165] H. Matsui and H. Tabata, “In-plane anisotropy of polarized photoluminescence in M-plane (10 $\bar{1}$ 0) ZnO and MgZnO/ZnO multiple quantum wells,” *Applied Physics Letters*, vol. 94, p. 161907, Apr. 2009.
- [166] E. Di Russo, L. Mancini, F. Moyon, S. Moldovan, J. Houard, F. H. Julien, M. Tchernycheva, J. M. Chauveau, M. Hugues, G. Da Costa, I. Blum, W. Lefebvre, D. Blavette, and L. Rigutti, “Three-dimensional atomic-scale investigation of $zno/mg_xzn_{1-x}o$ m -plane heterostructures,” *Applied Physics Letters*, vol. 111, p. 032108, July 2017.
- [167] E. Di Russo, F. Moyon, N. Gogneau, L. Largeau, E. Giraud, J.-F. Carlin, N. Grandjean, J. M. Chauveau, M. Hugues, I. Blum, W. Lefebvre, F. Vurpillot, D. Blavette, and L. Rigutti, “Composition metrology of ternary semiconductor alloys analyzed by atom probe tomography,” *Reports on Progress in Physics*, vol. 122, pp. 16704–16714, July 2018.
- [168] N. Amirifar, R. Larde, E. Talbot, P. Pareige, L. Rigutti, L. Mancini, J. Houard, C. Castro, V. Sallet, E. Zehani, S. Hassani, C. Sartel, A. Ziani, and X. Portier, “Quantitative analysis of doped/undoped ZnO nanomaterials using laser assisted atom probe tomography: Influence of the analysis parameters,” *Journal of Applied Physics*, vol. 118, p. 215703, Dec. 2015.
- [169] L. Rigutti, G. Jacopin, L. Largeau, E. Galopin, A. De Luna Bugallo, F. H. Julien, J.-C. Harmand, F. Glas, and M. Tchernycheva, “Correlation of optical and structural properties of GaN/AlN core-shell nanowires,” *Physical Review B*, vol. 83, p. 155320, Apr. 2011.
- [170] G. Jacopin, L. Rigutti, A. D. L. Bugallo, F. H. Julien, C. Baratto, E. Comini, M. Ferroni, and M. Tchernycheva, “High degree of polarization of the near-band-edge photoluminescence in ZnO nanowires,” *Nanoscale Research Letters*, vol. 6, p. 501, Aug. 2011.
- [171] L. Rigutti, M. Tchernycheva, A. De Luna Bugallo, G. Jacopin, F. H. Julien, F. Furtmayr, M. Stutzmann, M. Eickhoff, R. Songmuang, and F. Fortuna,

“Photoluminescence polarization properties of single GaN nanowires containing $\text{Al}_x\text{Ga}_{1-x}\text{N}/\text{GaN}$ quantum discs,” *Physical Review B*, vol. 81, p. 045411, Jan. 2017.

Appendix

A - Correlated data acquired through the μ PL-APT system

Data collected in real time, during the evaporation of the tip A2. Thanks to these data, it was possible to correlate the evolution of the spectral peaks related to the ZnO MQWs and the MgZnO barriers, during the evaporation of the layers of the ZnO/MgZnO hetrostructure.

Origin file	$\Delta t_{acquisition}$ (s)	# atoms beginning	# atoms end	V_{DC} (kV)	# evaporated QWs	Comments
# 1	20	0	0	beginning acquisition
# 2	60	0	0	...
# 3	120	0	0	...
# 4	20	0	0	...
# 5	120	0.5	0	...
# 6	60	1	0	...
# 7	60	1.5	0	...
# 8	60	2	0	...
# 9	60	2.5	0	...
# 10	60	3	0	...
# 11	150	3.5	0	...
# 12	150	4	0	...
# 13	150	4.5	0	...
# 14	150	5	0	...
# 15	150	5.5	0	...

Origin file	$\Delta t_{acquisition}$ (s)	# atoms beginning	# atoms end	V_{DC} (kV)	# evaporated QWs	Comments
# 16	150	65 K	71 K	6	0	...
# 17	150	75 K	92 K	6.5	0	...
# 18	150	104 K	143 K	7	0	...
# 19	150	189 K		7.5	0	...
# 20	300	404 K	547 K	<i>soft</i>	1	inside 1 st QW
# 21	300	558 K	696 K	<i>soft</i>	1	inside 1 st barrier
# 22	300	706 K	839 K	<i>soft</i>	1	inside 1 st barrier
# 23	300	856 K	990 K	<i>soft</i>	1	inside 1 st barrier
# 24	300	1000 K	1138 K	<i>soft</i>	1	inside 1 st barrier
# 25	300	1148 K	1287 K	<i>soft</i>	1	inside 1 st barrier
# 26	300	1304 K	1440 K	<i>soft</i>	1	inside 1 st barrier
# 27	300	1478 K	1621 K	<i>soft</i>	1+2	inside 2 nd QW
# 28	300	1626 K	1763 K	<i>soft</i>	2	out of the 2 nd QW
# 29	300	1767 K	1945 K	<i>soft</i>	2	2 nd barrier
# 30	300	1952 K	2173 K	<i>soft</i>	2	2 nd barrier
# 31	300	2195 K	2413 K	<i>soft</i>	2	2 nd barrier
# 32	300	2428 K	2543 K	<i>soft</i>	2	2 nd barrier
# 33	300	2676 K	2912 K	<i>soft</i>	2+3	end 2 nd barrier +inside 3 rd QW
# 34	300	2928 K	3156 K	<i>soft</i>	3	evaporation 3 rd QW
# 35	300	3175 K	3411 K	<i>soft</i>	3	3 rd barrier
# 36	300	3423 K	3652 K	<i>soft</i>	3	3 rd barrier
# 37	300	3661 K	3891 K	<i>soft</i>	3	3 rd barrier
# 38	300	3900 K	4145 K	<i>soft</i>	3	3 rd barrier
# 39	300	4154 K	4371 K	<i>soft</i>	3+4	end 3 rd barrier +inside 4 th QW
# 40	300	4377 K	4622 K	<i>soft</i>	4	evaporation 4 th QW
# 41	300	4629 K	4862 K	<i>soft</i>	4	evaporation 4 th QW
# 42	300	4869 K	5097 K	<i>soft</i>	4	4 th barrier
# 43	300	5102 K	5325 K	<i>soft</i>	4	4 th barrier
# 44	300	5350 K	5567 K	<i>soft</i>	4	4 th barrier
# 45	300	5590 K	5827 K	<i>soft</i>	4	4 th barrier
# 46	300	5855 K	6070 K	<i>soft</i>	4	4 th barrier
# 47	300	6095 K	6334 K	<i>soft</i>	4+5	end 4 th barrier +inside 5 th QW
# 48	300	6362 K	6587 K	<i>soft</i>	5	inside 5 th QW+barrier
# 49	300	6618 K	6844 K	<i>soft</i>	5	inside 5 th barrier
# 50	300	6905 K	7134 K	<i>soft</i>	5	inside 5 th barrier
# 51	300	7151 K	7384 K	<i>soft</i>	5	inside 5 th barrier
# 52	300	7414 K	7640 K	<i>soft</i>	5	inside 5 th barrier
# 53	300	7662 K	7878 K	<i>soft</i>	5	inside 5 th barrier
# 54	300	7892 K	8125 K	<i>soft</i>	5+6	end 5 th barrier +inside 6 th QW

# 55	300	8158 K	8398 K	<i>soft</i>	6	evaporation 6 th QW
# 56	300	8421 K	8651 K	<i>soft</i>	6	out of 6 th QW
# 57	300	8664 K	8882 K	<i>soft</i>	6	inside 6 th barrier
# 58	150	8890 K	9007 K	<i>soft</i>	6	inside 6 th barrier
# 59	150	9017 K	9128 K	<i>soft</i>	6	inside 6 th barrier
# 60	150	9139 K	9251 K	<i>soft</i>	6	inside 5 th barrier
# 61	150	9262 K	9381 K	<i>soft</i>	6	inside 6 th barrier
# 62	150	9391 K		<i>soft</i>	6	inside 6 th barrier
# 63	150	9568 K	9678 K	<i>soft</i>	6	inside 6 th barrier
# 64	150	9693 K	9814 K	<i>soft</i>	6	inside 6 th barrier
# 65	150	9830 K	9941 K	<i>soft</i>	6+7	end 6 th barrier +inside 7 th QW
# 66	150	9955 K	10075 K	<i>soft</i>	7	evaporation 7 th QW
# 67	150	10097 K	10220 K	<i>soft</i>	7	evaporation 7 th QW
# 68	150	10241 K	10353 K	<i>soft</i>	7	evaporation 7 th QW
# 69	150	10375 K	10484 K	<i>soft</i>	7	end 7 th QW +begin 7 th barrier
# 70	150	10503 K	10613 K	<i>soft</i>	7	inside 7 th barrier
# 71	150	10628 K	10736 K	<i>soft</i>	7	inside 7 th barrier
# 72	150	10755 K	10872 K	<i>soft</i>	7	inside 7 th barrier
# 73	150	10891 K	10999 K	<i>soft</i>	7	inside 7 th barrier
# 74	150	11046 K	11154 K	<i>soft</i>	7+8	end 7 th barrier +begin 8 th QW
# 75	150	11173 K	11275 K	<i>soft</i>	8	evaporation 8 th QW
# 76	150	11289 K	11387 K	<i>soft</i>	8	inside 8 th barrier
# 77	150	11397 K	11504 K	<i>soft</i>	8	inside 8 th barrier
# 78	150	11511 K	11619 K	<i>soft</i>	8	inside 8 th barrier
# 79	150	11625 K	11731 K	<i>soft</i>	8	inside 8 th barrier
# 80	150	11735 K	11854 K	<i>soft</i>	8	inside 8 th barrier
# 81	150	11875 K	11985 K	<i>soft</i>	8	inside 8 th barrier
# 82	150	11991 K	12103 K	<i>soft</i>	8	inside 8 th barrier
# 83	150	12118 K	12235 K	<i>soft</i>	8	inside 8 th barrier
# 84	150	12237 K	12354 K	<i>soft</i>	8	inside 8 th barrier
# 85	150	12361 K	12476 K	<i>soft</i>	8	beginning substrate
# 86	150	12477 K	12585 K	<i>soft</i>	8	inside substrate
# 87	150	12592 K	12710 K	<i>soft</i>	8	inside substrate

B - Experimental Results related to the tip A3

The tip A3 was obtained by the same sample, named ‘ZOE179’. The characteristics of the ZnO/MgZnO MQWs heterostructure, related to the tip A3, so, are expected to be in good agreement with the ones of the tip A2.

Below, the experimental results obtained on the tip A3, by the μ PL and APT analysis are reported.

Elaboration of the APT data

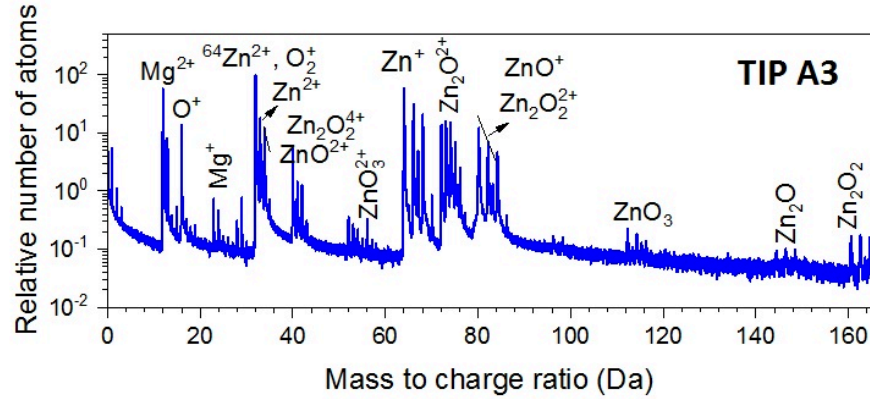


Figure 17: The mass spectrum related to the tip A3. The elaboration of the APT-data was realized by Pradip Dalapati.

	TIP A3
<i>Projection point</i> (m+1)	1.5
<i>F · k_f</i> (V/nm)	15
<i>Curvature factor</i>	0.8
<i>Detection efficiency</i>	0.4

Table 6: Tip A3 parameters given by the APT 3D-reconstruction: *projection point*, *F · k_f* factor, *curvature factor*, *detection efficiency*.

The reconstruction of the 3D volume of the tip A3, in figure 20(a) reports a certain

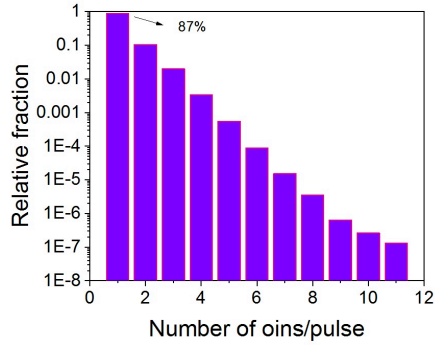


Figure 18: Distribution of multiple-ion events associated to the mass spectrum presented in fig 17. 87% of the total events is associated to single events, while the remaining 13% is associated to multi-ions detection.

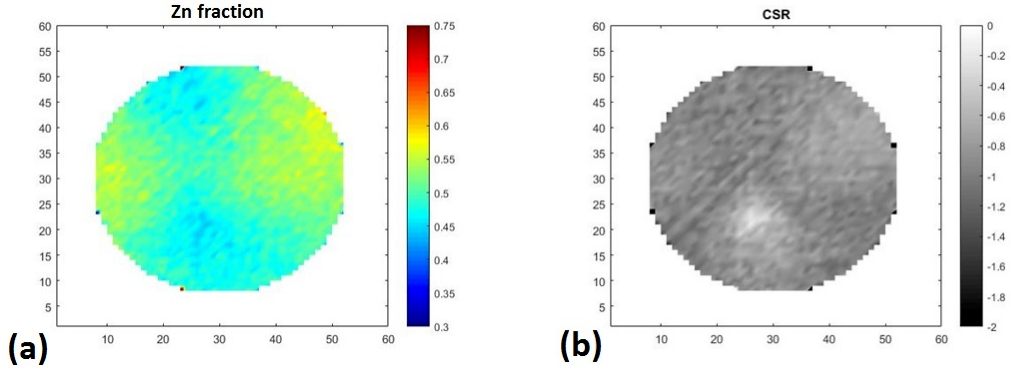


Figure 19: Hitmaps of: (a) the Zn atomic fractions visualized through detector statistics and (b) the Zn^{2+}/Zn^{+} charge state ratio (CSR).

percentage of the Mg^{2+} detected ions in blue and another percentage of the Zn^{1+or2+} detected ions in red.

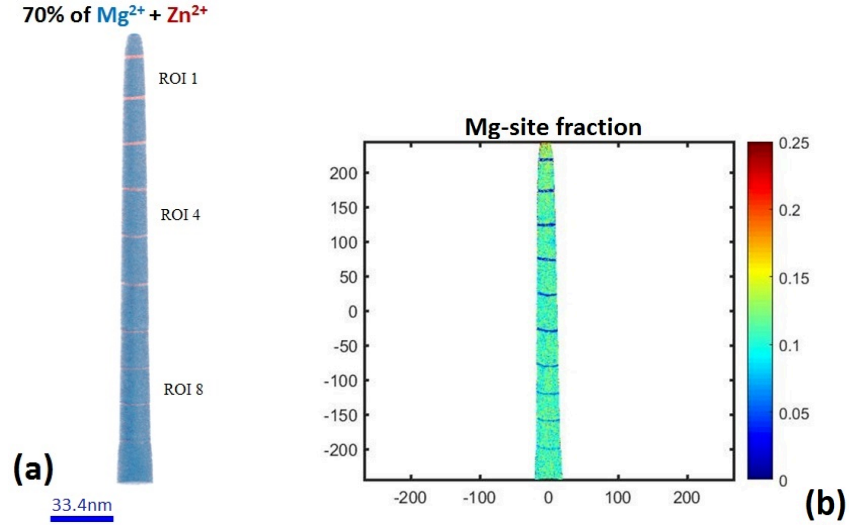


Figure 20: (a) 3D volume reconstruction of the tip A3 with both the Mg^{2+} and Zn^{1+or2+} ions, on the left side, and 3D virtual reconstruction just with the Mg^{2+} and Zn^{1+} ions, on the right side. (b) 2D-distribution of the Mg II-site fraction, calculated over a volume of $(30 \times 30 \times 40) \text{ nm}^3$.

By the Mg -profile along the a -axis, as done for the tip A2, was estimated the value of the Mg II-site fraction for the tip A3, which is in agreement with the values related to the tip A2. The values deduced for each $MgZnO$ barrier of the tip A3 are reported in the table 7. In order to study the alloy fluctuation inside the $MgZnO$ barriers, the Mg -profile along the a -axis was investigated. The profiles, in fig. 5.10, revealed that the Mg -content is almost constant within the barriers and the average value estimated for each $MgZnO$ barrier is reported in the table 7. The QWs thickness was evaluated with the same method adopted for the tip A2 and the results, which correspond to the ones related to the tip A2, are reported in table 8.

Barrier	Mg-site fraction
#1	0.087 ± 0.008
#2	0.085 ± 0.008
#3	0.087 ± 0.008
#4	0.087 ± 0.008
#5	0.089 ± 0.008
#6	0.091 ± 0.009
#7	0.088 ± 0.008

Table 7: The *Mg* II-site fraction.

QW	FWHM (nm)
#1	1.48 ± 0.13
#2	1.8 ± 0.2
#3	1.97 ± 0.16
#4	2.00 ± 0.14
#5	2.8 ± 0.3
#6	2.07 ± 0.13
#7	2.94 ± 0.15

Table 8: QWs size of the tip A3

Elaboration of the μ PL data

The PL spectra reported in figure 21(a) show the optical signature related to the components which constitute the tip A3, during the ongoing evaporation process. The exciting laser impings on the tip A3 at: $\lambda = 260 \text{ nm}$, $P = 500 \mu\text{W} \pm 10\%$ and $T=25 \text{ K}$. Each spectrum (S_i) was collected at the same integration time ($\Delta t_{\text{acquisition}} = 120 \text{ s}$) and at the end of the acquisition of one PL spectrum a new one was acquired. These spectra, figure 21(a), show the trend of all the components present in the *ZnO/MgZnO* heterostructure from the beginning of the evaporation process (pointed out by the green spectrum, labeled as ‘Begin’) until the end of the evaporation of the last barrier of the *ZnO/MgZnO* heterostructure (pointed out by the red spectrum, labeled as ‘End’). As we can observe, the evolution of the signals related to the barriers and the *ZnO* substrate shows again a clear shift of their peaks towards lower energy, in agreement with the *red-shift* observed, for the tip A2. During the evaporation of the APT specimen, as better highlighted by the 2D map in figure 21(b), also the signal related to the QWs shows a shift towards lower energy, in agreement with the results obtained on the tip A2.

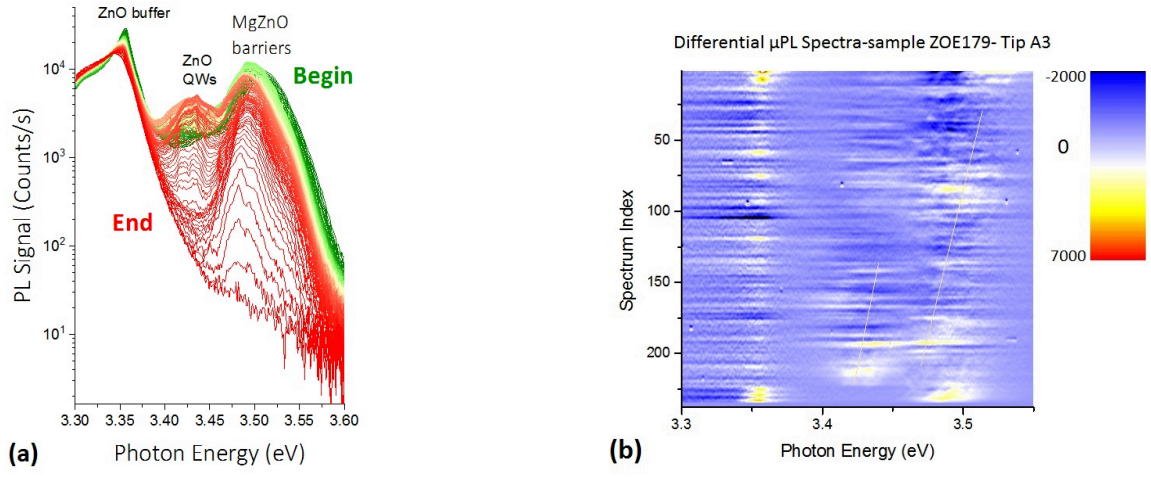


Figure 21: (a) Series of spectra, detected during the μPL -APT analysis of the tip A3, where the spectral components progressively disappear due to the evaporation of the tip. (b) Differential spectra of the tip A3 represented in a 2D color-map: the *red-shift* of the signals related to the QWs and barriers are highlighted by the two yellow lines.

Acknowledgements

This thesis is the result of an important experience in my life. As any important experience, it was not carried out alone, but with a good company. For this reason, I would like to express, in these last pages, my gratitude to the people who lived with me these three years and gave me the motivation to arrive until the end, enjoying everyday.

My advisors: Angela Vella and Lorenzo Rigutti helped me to improve my scientific skills, they were available to dialogue and to compare our point of views, always in a good atmosphere. They helped me in order to highlight my natural aptitudes and so, in this sense, they didn't only represent my teachers for these three years, but they also suggested me a possible direction to follow after this thesis.

My family: my mother Graziella, my father Claudio, my brother Federico and my relatives, also if further, they were constantly present in order to sustain each other. They were a continuous proof of faith and they showed me how it is possible to listen carefully and to understand someone although the distance.

My friends, in order to cite some of them: Mohamed, Souhaila, Federica, Mario, Kamal, Elodie, Chantal, Kevi, Marie-Laure, Olha, Liz, Camille, Serena, Ludovica, Chiara, Davide, Amalia, Sahar, Diana, Roger, Danut, all the people of the laboratory and of course all the people with who it was really easy to share some time and be part of the same team. To all these friends I am sincerely thankful, because they recharged my energy, they sustained me and they helped me to find the positive attitude in order to appreciate everyday.